CLIMATOLOGY

Snowball Earth climate dynamics and Cryogenian geology-geobiology

Paul F. Hoffman,[1,2]* Dorian S. Abbot,[3] Yosef Ashkenazy,[4] Douglas I. Benn,[5] Jochen J. Brocks,[6] Phoebe A. Cohen,[7] Grant M. Cox,[8,9] Jessica R. Creveling,[10] Yannick Donnadieu,[11,12] Douglas H. Erwin,[13,14] Ian J. Fairchild,[15] David Ferreira,[16] Jason C. Goodman,[17] Galen P. Halverson,[18] Malte F. Jansen,[3] Guillaume Le Hir,[19] Gordon D. Love,[20] Francis A. Macdonald,[1] Adam C. Maloof,[21] Camille A. Partin,[22] Gilles Ramstein,[11] Brian E. J. Rose,[23] Catherine V. Rose,[24†] Peter M. Sadler,[20] Eli Tziperman,[1] Aiko Voigt,[25,26] Stephen G. Warren[27]

Geological evidence indicates that grounded ice sheets reached sea level at all latitudes during two long-lived Cryogenian (58 and ≥5 My) glaciations. Combined uranium-lead and rhenium-osmium dating suggests that the older (Sturtian) glacial onset and both terminations were globally synchronous. Geochemical data imply that CO_2 was 10^2 PAL (present atmospheric level) at the younger termination, consistent with a global ice cover. Sturtian glaciation followed breakup of a tropical supercontinent, and its onset coincided with the equatorial emplacement of a large igneous province. Modeling shows that the small thermal inertia of a globally frozen surface reverses the annual mean tropical atmospheric circulation, producing an equatorial desert and net snow and frost accumulation elsewhere. Oceanic ice thickens, forming a sea glacier that flows gravitationally toward the equator, sustained by the hydrologic cycle and by basal freezing and melting. Tropical ice sheets flow faster as CO_2 rises but lose mass and become sensitive to orbital changes. Equatorial dust accumulation engenders supraglacial oligotrophic meltwater ecosystems, favorable for cyanobacteria and certain eukaryotes. Meltwater flushing through cracks enables organic burial and submarine deposition of airborne volcanic ash. The subglacial ocean is turbulent and well mixed, in response to geothermal heating and heat loss through the ice cover, increasing with latitude. Terminal carbonate deposits, unique to Cryogenian glaciations, are products of intense weathering and ocean stratification. Whole-ocean warming and collapsing peripheral bulges allow marine coastal flooding to continue long after ice-sheet disappearance. The evolutionary legacy of Snowball Earth is perceptible in fossils and living organisms.

INTRODUCTION

For 50 years, climate models of increasing complexity have hinted that Earth is potentially vulnerable to global glaciation through ice-albedo feedback (Fig. 1) (*1*–*23*). Independent geological evidence points to consecutive "Snowball Earth" (*24*) episodes in the Neoproterozoic era (*24*–*34*) and at least one such episode in the early Paleoproterozoic era (Fig. 2B) (*35*–*40*). Strangely, virtually no ice sheets are known to have existed during the intervening 1.5 billion years (Gy) of the Proterozoic glacial gap (Fig. 2B). The oldest Snowball Earth (*35*–*40*) was broadly coeval with the Great Oxidation Event (Fig. 2B), the first rise of molecular oxygen (*41*–*45*), whereas the younger tandem (Fig. 2A) was associated with the emergence of multicellularity in animals (Fig. 3) (*46*–*49*).

The Cryogenian period (*50*) encompasses the paired Neoproterozoic Snowball Earths and the brief nonglacial interlude (Fig. 2A). The term "cryochron" (*27*) was proposed for the panglacial epochs, on the assumption that their onsets and terminations were sharply defined in time, which now appears to be the case (Table 1). The older cryochron has come to be known as "Sturtian" and the younger one has come to be known as "Marinoan," after Sturt Gorge and Marino Rocks near Adelaide, South Australia, where they were recognized and mapped over 100 years ago (*51*). [As originally defined (*52*), these regional terms did not refer exclusively to the glacial epochs, but the original terminology has been superseded by the formal periods of the International Time Scale (Fig. 2A) (*50*, *53*). We find it convenient to

[1]Department of Earth and Planetary Sciences, Harvard University, Cambridge, MA 02138, USA. [2]School of Earth and Ocean Sciences, University of Victoria, Victoria, British Columbia V8P 5C2, Canada. [3]Department of Geophysical Sciences, University of Chicago, Chicago, IL 60637, USA. [4]Department of Solar Energy and Environmental Physics, Ben-Gurion University of the Negev, Midreshet Ben-Gurion, 84990, Israel. [5]School of Geography and Sustainable Development, University of St Andrews, St Andrews, Fife KY16 8YA, UK. [6]Research School of Earth Sciences, Australian National University, Canberra, Australian Capital Territory 2601, Australia. [7]Geosciences, Williams College, Williamstown, MA 01267, USA. [8]Centre for Tectonics, Resources and Exploration (TRaX), Department of Earth Sciences, University of Adelaide, Adelaide, South Australia 5005, Australia. [9]Department of Applied Geology, Curtin University, Bentley, Western Australia 6845, Australia. [10]College of Earth, Ocean, and Atmospheric Sciences, Oregon State University, Corvallis, OR 97331–5503, USA. [11]Laboratoire des Sciences du Climat et de l'Environnement (LSCE), Institut Pierre Simon Laplace (IPSL), CEA-CNRS-UVSQ, Université Paris-Saclay, 91191 Gif-sur-Yvette, France. [12]Aix-Marseille Université, CNRS, L'Institut de recherche pour le développement (IRD), Centre Européen de Recherche et D'enseignement de Géosciences de L'environnement (CEREGE), 13545 Aix-en-Provence, France. [13]Department of Paleobiology, Smithsonian Institution, P.O. Box 37012, MRC 121, Washington, DC 20013–7012, USA. [14]Santa Fe Institute, 1399 Hyde Park Road, Santa Fe, NM 87501, USA. [15]School of Geography, Earth and Environmental Sciences, University of Birmingham, Edgbaston, Birmingham B15 2TT, UK. [16]Department of Meteorology, University of Reading, Reading, RG6 6BB, UK. [17]Department of Environmental Science, Wheaton College, Norton, MA 02766, USA. [18]Department of Earth and Planetary Sciences, McGill University, Montréal, Québec H3A 0E8, Canada. [19]Institut de Physique du Globe de Paris, 1, rue Jussieu, 75005 Paris, France. [20]Department of Earth Sciences, University of California, Riverside, Riverside, CA 92521, USA. [21]Department of Geosciences, Princeton University, Princeton, NJ 08544, USA. [22]Department of Geological Sciences, University of Saskatchewan, Saskatoon, Saskatchewan S7N 5E2, Canada. [23]Department of Atmospheric and Environmental Sciences, University at Albany, Albany, NY 12222, USA. [24]Department of Geology, Trinity College Dublin, Dublin 2, Ireland. [25]Institute of Meteorology and Climate Research, Department of Troposphere Research, Karlsruhe Institute of Technology, Karlsruhe, Baden-Württemberg, Germany. [26]Lamont-Doherty Earth Observatory, Columbia University, P.O. Box 1000, Palisades, NY 10964–1000, USA. [27]Department of Atmospheric Sciences, University of Washington, Seattle, WA 98195–1640, USA.
*Corresponding author. Email: paulfhoffman@gmail.com
†Present address: School of Earth and Environmental Sciences, University of St Andrews, Irvine Building, St Andrews, Fyfe KY16 9AL, UK.

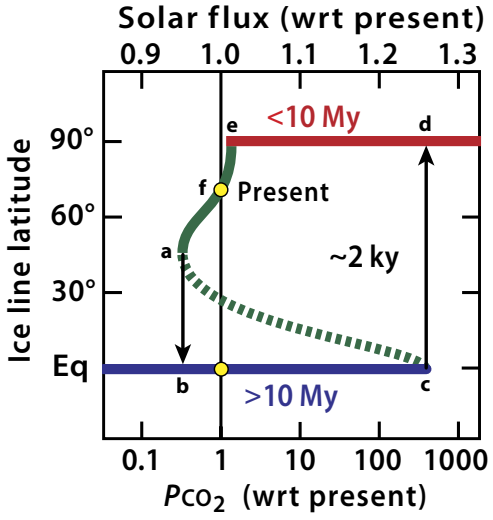

Fig. 1. Generic bifurcation diagram illustrating the Snowball Earth hysteresis. Ice-line latitude as a function of solar or CO_2 radiative forcing in a one-dimensional (1D) (meridional) energy-balance model of the Budyko-Sellers type (*3*, *4*), showing three stable branches (red, green, and blue solid lines) and the unstable regime (dashed line). Yellow dots are stable climates possible with present-day forcing. Black arrows indicate nonequilibrium transitions. In response to lower forcing, ice line migrates equatorward to the ice-albedo instability threshold (a), whereupon the ice line advances uncontrollably to the equator (Eq) (b). With reduced sinks for carbon, normal volcanic outgassing drives atmospheric CO_2 higher over millions to tens of millions of years (*73*) until it reaches the deglaciation threshold (c). Once the tropical ocean begins to open, ice-albedo feedback drives the ice line rapidly poleward (in ~2 ky) (*327*) to (d), where high CO_2 combined with low surface albedo creates a torrid greenhouse climate. Intense silicate weathering and carbon burial lower atmospheric CO_2 (in 10^7 years) (*164*) to (e), the threshold for the reestablishment of a polar ice cap. The hysteresis loop predicts that Snowball glaciations were long-lived (b and c), began synchronously at low latitudes (a and b), and ended synchronously at all latitudes under extreme CO_2 radiative forcing (c and d). The ocean is predicted to undergo severe acidification and deacidification in response to the CO_2 hysteresis. Qualitatively similar hysteresis is found in 3D general circulation models (GCMs). P_{CO_2}, partial pressure of CO_2; wrt, with respect to.

follow the current informal international usage, wherein "Sturtian" and "Marinoan" identify the cryochron and its immediate aftermath, including the respective postglacial cap-carbonate sequences.] The nonglacial interlude separating the cryochrons was 9 to 19 million years (My) in duration (Fig. 2A).

The worldwide distribution of late Precambrian glacial deposits (Fig. 4) became evident in the 1930s (*25*, *54*, *55*), but only recently has their synchroneity been demonstrated radiometrically (*32*, *56*–*65*). Previously, geologists were divided whether the distribution of glacial deposits represents extraordinary climates (*29*, *66*) or diachronous products of continental drift (*67*, *68*).

The recognition that a panglacial state might be self-terminating (*69*), due to feedback in the geochemical carbon cycle, meant that its occurrence in the geological past could not be ruled out on grounds of irreversibility. "If a global glaciation were to occur, the rate of silicate weathering should fall very nearly to zero (due to the cessation of normal processes of precipitation, erosion, and runoff), and carbon dioxide should accumulate in the atmosphere at whatever rate it is released from volcanoes. Even the present rate of release would yield 1 bar of carbon dioxide in only 20 million years. The resultant large greenhouse effect should melt the ice cover in a geologically short period of time" [(*69*), p. 9781]. Because Snowball Earth surface temperatures are below the freezing point of water everywhere, due to high planetary albedo, there is no rain to scrub CO_2 (insoluble in snow) from the atmosphere.

Deposition of CO_2 ice at the poles in winter is a potential sink that might render a Snowball Earth irreversible (*70*). CO_2 ice, having a density of 1.5 g cm^{-3}, might sink gravitationally into the polar water ice, melting as it penetrates warmer ice at depth (*70*). On the other hand, CO_2 ice clouds warm the poles in winter by scattering outgoing radiation (*71*, *72*), yet dissipate in summer, allowing sunshine to reach the surface and sublimate CO_2 ice particles in the firn (*70*). As atmospheric CO_2 accumulates, the stability range for deposition of CO_2 ice initially grows because of higher saturation (*70*). However, an ice-covered planet with Earth-like obliquity and distance (1 astronomical unit) from a Sun-like star, with or without CO_2 ice clouds, remains far below the threshold for CO_2 ice deposition at any CO_2 level relevant to a Cryogenian

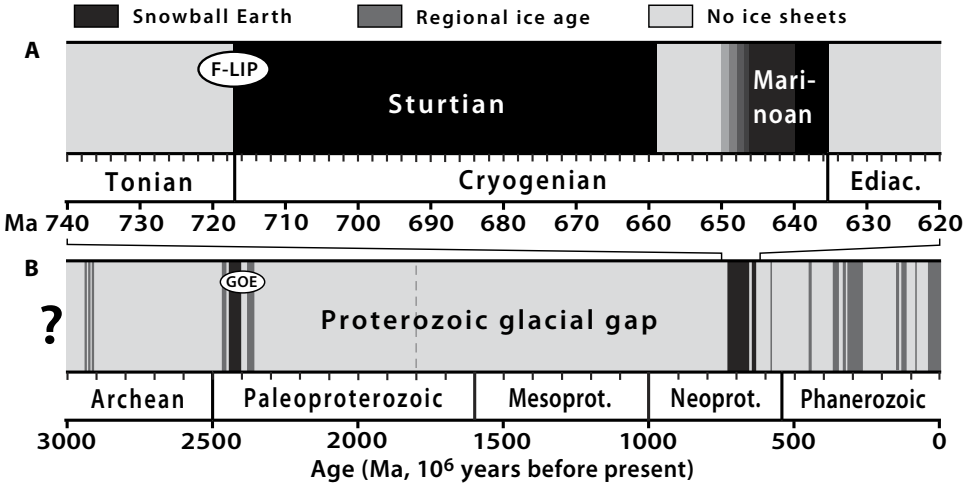

Fig. 2. Glacial epochs on Earth since 3.0 Ga. (**A**) Black bands indicate durations of the Sturtian and Marinoan cryochrons (Table 1). The graded start to the Marinoan cryochron denotes chronometric uncertainty, not gradual onset. Ellipse F-LIP shows the possible age span of the Franklin large igneous province (LIP) (*32*, *127*). (**B**) Snowball Earth chrons (black), regional-scale ice ages (medium gray), and nonglacial intervals (light gray) since 3.0 Ga. Ellipse GOE is centered on the Great Oxidation Event, as recorded by the disappearance of mass-independent S isotope fractionations ≥0.3 per mil (‰) in sedimentary sulfide and sulfate minerals (*484*). The dashed gray line indicates questionable glaciation.

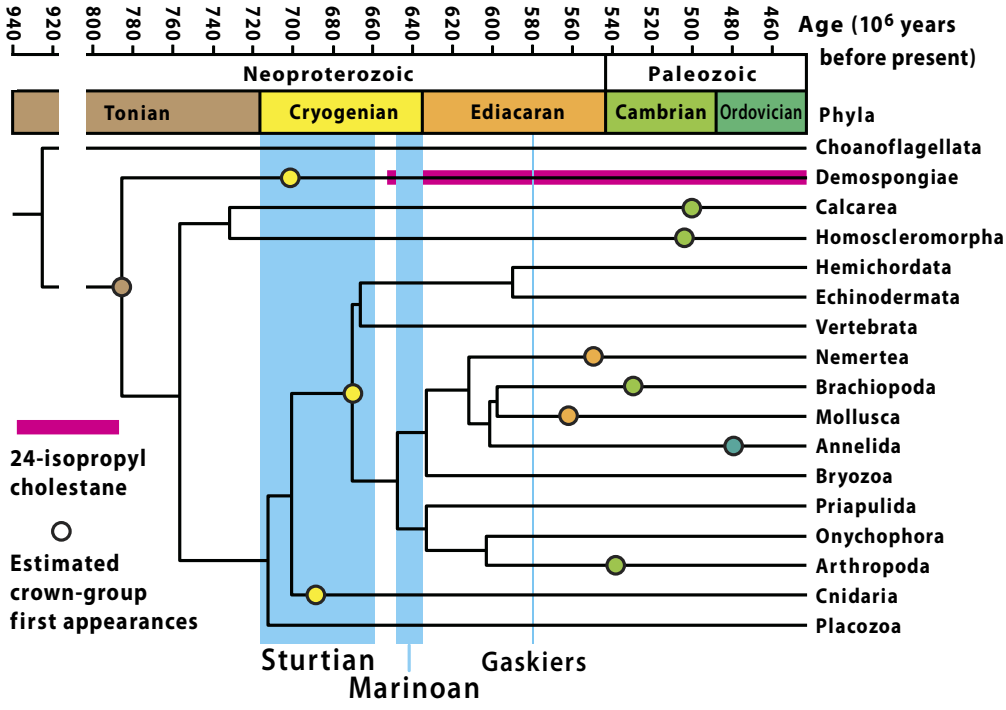

Fig. 3. Early metazoan phylogeny, the geologic time scale, and Neoproterozoic glacial epochs. Simplified topology of the metazoan radiation (*315*), based on a phylogeny and concatenated, invertebrate-calibrated, molecular clock estimates (*47*) and glacial chronology (Table 1). Sterane biomarkers in the South Oman Salt Basin are interpreted to be products of demosponges, appearing no later than the clement interlude between the Sturtian and Marinoan glaciations (*46*, *48*).

Snowball Earth [see figure 2b and c in the study by Turbet *et al.* (*70*)]. The risk of irreversibility due to CO_2-ice deposition is not so easily dismissed for a Siderian (2.4 Ga) Snowball Earth (Fig. 2B), when the Sun was about 10% dimmer than in the Cryogenian.

Seafloor weathering represents another sink for atmospheric CO_2 on Snowball Earth (*73*–*75*). Cold bottom-water temperature slows the rate of seafloor weathering (*76*), but this is nullified by the long duration and low pelagic sediment flux of the Snowball ocean. Weathering rate increases when the pH of cold seawater falls below 7.0 in response to CO_2 rise (*76*). Current estimates of the CO_2 level required for Cryogenian Snowball termination range from 0.01 to 0.1 volume mixing ratio, dependent on the tropical ice albedo and other factors (*77*–*82*). Seafloor weathering, a sink for CO_2 and a source of alkalinity, is a potential factor in the longevity of the Sturtian cryochron (Fig. 2A).

Self-termination occurs under circumstances that are falsifiable geologically. Snowball cryochrons should be long-lived, reflecting the enormous amount of CO_2 that must accumulate to counteract the high planetary albedo. Their onsets should be synchronous at low latitudes, and their terminations should be synchronous everywhere (Fig. 1). Terminations should be accompanied by extraordinarily high atmospheric CO_2 levels, equivalent to 10^4 to 10^5 parts per million (ppm) by volume in the present atmosphere, giving rise to torrid greenhouse aftermaths as the surface darkens due to ice retreat (Fig. 1). These predictions are increasingly supported by combined U-Pb and Re-Os geochronology (*32*, *56*–*65*, *83*) and by geochemical data (*60*, *84*–*91*), none of which existed when Cryogenian Snowball states were hypothesized (*24*, *27*).

Less clear is how the Cryogenian sedimentary and geobiological records should be interpreted within the context of Snowball Earth. The Cryogenian sedimentary record is widespread and accessible (Fig. 4), fostering detailed studies in many areas (*92*–*102*). In contrast, the Cryogenian fossil record has low total and within-assemblage diversity (*103*). Molecular fossils (*46*) and macrofossils (*104*–*107*) are rare, and molecular "clock" estimates for early metazoan divergences (Fig. 3) are imprecisely calibrated (*108*). Moreover, recycling of preglacial organic matter into glacial deposits is inevitable, because glaciers would have readily entrained organic-rich sediments on the continental shelves they traversed (*109*). Although both the sedimentary and fossil records have been cited as casting doubt on the Snowball Earth hypothesis (*107*, *110*–*114*), the reality is that, until recently, the concept itself was not fleshed out in sufficient detail to make reliable predictions regarding those records.

This unpromising situation is now changing. Research on Snowball Earth climate dynamics has taken hold at leading institutions on four continents. Its motivation is not only to assist geology and geobiology but also to pursue potential applications for study of exoplanets, to gain insights from intermodel comparison, and to stimulate fresh perspectives on the Anthropocene. The goal of this paper is more modest. We survey progress in modeling the Snowball Earth atmosphere, cryosphere, hydrosphere, and lithosphere, specifically as it pertains to Cryogenian geology and geobiology. Such a review is timely because the recent development of a radiometric chronology for Cryogenian glaciation (*63*) has breathed new life into Neoproterozoic research. We build on an insightful pair of 6-year-old reviews of the same topic (*115*, *116*) and offer ours in the same ecumenical spirit.

We begin by reviewing Cryogenian geochronology and paleogeography, followed by Snowball atmospheric dynamics and the hydrologic cycle, Snowball ice-sheet extent and variability, low-latitude sea ice-margin stability, sea-glacier dynamics, supraglacial cryoconite ecosystems, subglacial ocean dynamics, and "cap-carbonate" sequences unique to Cryogenian glacial terminations. We conclude with a summary of modeling results and their geological implications. Although we

Table 1. U-Pb and Re-Os geochronological constraints on Cryogenian glacial onsets and terminations. CA, chemical abrasion; ID-TIMS, isotope-dilution and thermal-ionization mass spectrometry; SIMS, secondary-ion mass spectrometry.

Paleocontinent	Age (Ma)	Method*	Reference
Marinoan deglaciation/cap carbonate: 636.0 to 634.7 Ma			
Laurentia	>632.3 ± 5.9	Re-Os	(*63*)
South China	635.2 ± 0.5	U-Pb ID-TIMS	(*57*)
Southern Australia	636.41 ± 0.45	U-Pb CA-ID-TIMS	(*59*)
Swakop	635.21 ± 0.59/0.61/0.92	U-Pb CA-ID-TIMS	(*56*, *83*)
Marinoan glacial onset: 649.9 to 639.0 Ma			
Congo	>639.29 ± 0.26/0.31/0.75	U-Pb CA-ID-TIMS	(*83*)
Southern Australia	<645.1 ± 4.8	Re-Os	(*137*)
South China	<654.2 ± 2.7	U-Pb SIMS	(*134*)
South China	<654.5 ± 3.8	U-Pb SIMS	(*58*)
Sturtian deglaciation/cap carbonate: 659.3 to 658.5 Ma			
Southern Australia	>657.2 ± 2.4	Re-Os	(*137*)
Tuva-Mongolia	659.0 ± 4.5	Re-Os	(*63*)
Southern Australia	<659.7 ± 5.3	U-Pb SIMS	(*366*)
Laurentia	662.4 ± 3.9	Re-Os	(*60*)
South China	>662.7 ± 6.2	U-Pb SIMS	(*65*)
Sturtian glacial onset: 717.5 to 716.3 Ma			
Oman	>713.7 ± 0.5	U-Pb ID-TIMS	(*365*)
South China	<714.6 ± 5.2	U-Pb SIMS	(*64*)
South China	<715.9 ± 2.8	U-Pb SIMS	(*62*)
South China	<716.1 ± 3.4	U-Pb SIMS	(*62*)
Laurentia	>716.5 ± 0.2	U-Pb CA-ID-TIMS	(*32*)
Laurentia	<717.4 ± 0.1	U-Pb CA-ID-TIMs	(*32*)
Laurentia	<719.47 ± 0.29	U-Pb CA-ID-TIMS	(*61*)

* Re-Os isochron ages from sedimentary organic matter. Errors are quoted at the 2σ level of uncertainty. Where multiple uncertainties are given, they represent analytical/analytical + tracer solution/analytical + tracer solution + decay-constant uncertainties.

refer to them tangentially, we do not discuss the isotopic proxy records surrounding Cryogenian glaciation. To do so would easily double the length of the paper (and the list of authors).

We offer a few words for geologists who are more accustomed to the "inverse" approach. When we speak declaratively in describing the results of a climate model, there is no implication that nature necessarily behaved similarly. A model result is simply the equilibrium response of the model to a set of prescribed conditions. It is a job for geology to determine whether the record is consistent with model predictions. Like geology itself, models are a source of astonishment, wonder, and inspiration. Like geological observations, they are incomplete and subject to improvement. To help make the distinction clear, we will endeavor to use the present tense in describing model results and the past tense for inference based on geological data.

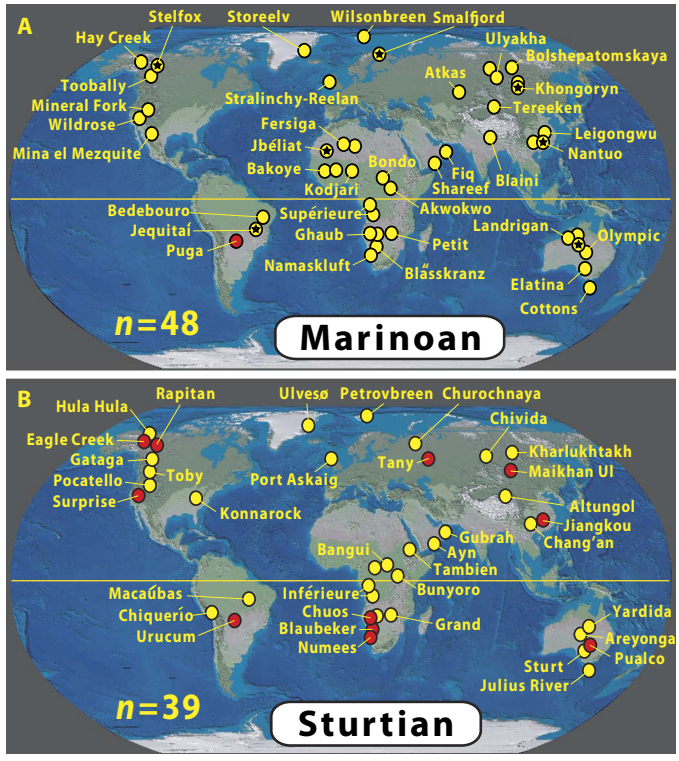

Fig. 4. Present distribution of Cryogenian glacial-periglacial deposits. (**A**) Marinoan (ca. 645 to 635 Ma) and (**B**) Sturtian (717 to 659 Ma) deposits (*28*, *33*). Yellow dots indicate regional-scale deposits of glacial and/or periglacial origin. Red dots indicate glacial-periglacial deposits with associated sedimentary Fe oxide formation (*160*, *400*). Black stars in yellow dots indicate occurrence of authigenic and/or seafloor barite ($BaSO_4$) in the postglacial cap dolostone (*131*). Areas lacking glacial deposits, for example, northeastern North America and central Europe, simply lack Cryogenian sedimentary records.

To a geologist, it may seem that climate models are overly concerned with the Snowball state and with glacial states close to the Snowball bifurcation. Why not the more geologically interesting onsets and terminations (Fig. 1)? The reason for this is that current climate models used in deep-time investigations are meaningful only as equilibrium responses to prescribed forcings. The equilibration time is typically hundreds to thousands of model years. Snowball onsets and terminations are highly nonequilibrium situations on these time scales. These nonequilibrium states can be modeled but are computationally demanding.

Because of inconsistent usage in the current glacial sedimentology literature, we need to clarify that we use the terms "dynamic" and "stability" in reference to ice flow and ice extent, respectively. A "dynamic" glacier is one that flows, and an "unstable" one waxes and wanes. Finally, we do not use the words "hypothesis" and "theory" to distinguish degrees of confidence or certainty regarding Snowball Earth. Theory refers to the mechanism behind the phenomenon. The hypothesis is the postulate (*24*) that the phenomenon actually occurred in the geologic past.

CRYOGENIAN CHRONOLOGY AND PALEOGEOGRAPHY

Geochronology

Before 2004 (*56*), no Cryogenian glacial deposit had been directly dated radiometrically. The Snowball Earth hypothesis (*24*) was then 12 years old, and the prospect of testing it geochronologically appeared remote.

Today, the onset of the Sturtian cryochron and the terminations of both cryochrons are tightly constrained at a million-year resolution by U-Pb and Re-Os geochronology on multiple paleocontinents (Table 1). This is a remarkable achievement and, more than any other factor, encourages the hypothesis to be taken seriously by geologists.

The time scale for Cryogenian glaciation (Table 1) is based on U-Pb geochronology of the mineral zircon ($ZrSiO_4$), separated from volcanic rocks including far-traveled ash layers (tuffs), and on Re-Os isochron ages for the deposition of organic-rich sediments. The former is the most precise and most accurate dating method in deep-time applications because of the refractory nature of zircon, its low nonradiogenic Pb content, and an internal "concordance" test between two independent decay schemes ($^{238}U \rightarrow {}^{206}Pb$ and $^{235}U \rightarrow {}^{207}Pb$) having different decay constants. The long history, current methodologies, and error-propagation procedures of U-Pb geochronology have recently been reviewed (*117*–*121*). An important recent development was chemical abrasion of zircon grains (*122*), which improves concordance through selective removal of damaged grain fractions that are susceptible to radiogenic Pb loss. Chemical abrasion coupled with ID-TIMS (CA-ID-TIMS) is the most accurate dating method. Early Pb loss is an insidious problem, resulting in ages that are too young but still concordant. Zircon grains having high U contents are most susceptible to early Pb loss and are routinely avoided. Basaltic rocks typically lack zircon but may contain the mineral baddeleyite (ZrO_2), which can also be dated by U-Pb but with technical issues that are less well resolved than for zircon.

Re-Os geochronology is a more recent development, pioneered less than 30 years ago (*123*) and successfully applied to a Paleozoic black shale in 2002 (*124*, *125*). Early attempts to date Neoproterozoic shales had mixed success, but after an improved extraction technique was introduced (*126*), intended to screen out nonhydrogenous (that is, detrital) Re and Os, isochron ages for Neoproterozoic organic-rich shales and limestones became generally compatible with existing U-Pb dating [(*63*) and Table 1]. As with all isochron methods, sampling and sample selection are critical.

The onset of the Sturtian cryochron at low (21° ± 3°N) paleolatitude is tightly constrained between 717.5 and 716.3 Ma by U-Pb (CA-ID-TIMS) zircon ages (*32*) from volcanic rocks in central Yukon (Canada). Zircon ages from South China and Arctic Alaska are consistent with these constraints (Table 1). The Sturtian onset is indistinguishable in time from the most reliable U-Pb baddeleyite ages of 716.33 ± 0.54 Ma (*32*) and 716 ± 1 Ma (*127*) from mafic sills and dikes in different parts of the Franklin LIP of northern Laurentia. Franklin dikes, sills, and lavas extend across northern Canada from Alaska to Greenland (*127*) and Siberia (*128*), implying that the original volcanic plateau may have covered an area of $>3 \times 10^6$ km^2, making it among the largest terrestrial LIPs of all time (*129*).

The termination of the Sturtian cryochron is globally marked by an organic-rich limestone (hereafter "cap limestone") that sharply but conformably overlies glacial or periglacial deposits (*130*, *131*). Re-Os isochron ages from cap limestones in Australia, Laurentia (Northwest Territories, Canada), and Mongolia, and a U-Pb (SIMS) zircon date from a volcanic ash layer within terminal glaciomarine deposits in South Australia, tightly constrain the date of the Sturtian termination between 659.3 and 658.5 Ma (Table 1). Accordingly, the duration of the Sturtian cryochron was between 57.0 and 59.0 My, nearly as long as the entire Cenozoic era.

Some authors infer that the Sturtian cryochron encompassed multiple discrete glaciations (*132*–*135*). There is sedimentological evidence for multiple advances and retreats of Sturtian ice-sheet margins and ice grounding lines (*92*, *95*, *136*). However, the cap limestone is unique to the final ice retreat, and wherever it has been dated, its age is ~659 Ma (Table 1). Nowhere have multiple cap carbonates been found within either cryochron, implying that the terminal deglaciations were unique events.

The onset of the Marinoan cryochron is only loosely constrained between 649.9 and 639.0 Ma by a pre-Marinoan Re-Os isochron age of 645.1 ± 4.8 Ma (*137*) for organic-rich shale (Tindelpina Member, lower Tapley Hill Formation) in South Australia and a syn-Marinoan U-Pb (CA-ID-TIMS) zircon age of 639.3 ± 0.3 Ma (*83*) from a volcanic tuff within glaciomarine diamictite (Ghaub Formation) in northern Namibia. Additional constraints on the Marinoan onset come from U-Pb (SIMS) zircon dates from tuffs within pre-Marinoan strata (Datangpo Formation) in South China (Table 1).

The nonglacial interlude between the Sturtian termination and the Marinoan onset had a total duration between 8.6 and 20.3 Ma (Table 1). The low or high ends of this range agree with an astrochronological estimate of 6 to 8 My for the same interlude in East Svalbard, assuming that 0.5-m-scale rhythms of dolomitic siltstone in shale were forced by orbital precession (*138*) or obliquity, respectively. However, whether the rhythms are truly periodic remains to be seen. Comparable in duration to the shorter Phanerozoic epochs (for example, Oligocene, Middle Jurassic, and Middle Devonian), the nonglacial interlude can be globally correlated. In East Greenland (*139*), East Svalbard (*138*), and South China (*140*–*142*), 0.2 to 0.3 km (uncompacted) of fine-grained terrigenous strata appear. In western Mongolia (*143*) and northern Namibia (*144*), one finds 0.6 km of limestone and dolostone. In Idaho (*133*) and Oman (*145*), there are 0.7 to 0.8 km of fine- and coarse-grained terrigenous deposits. Northwest Canada (Mackenzie Mountains) (*146*–*149*) and South Australia (*150*–*153*) have 1.3 and 3.0 km, respectively, of mixed terrigenous and carbonate strata. Accommodation created during the Sturtian glaciation and high rates of weathering and erosion in the Sturtian aftermath account for the high sedimentation rates (<0.1 km My^{-1}). The absence of large ice sheets is inferred from peritidal cycles in platform carbonates that lack karstic disconformities and other evidence of forced regressions [(*144*, *152*); but see the study by Day *et al.* (*149*)].

The termination of the Marinoan cryochron is globally marked by a laterally continuous unit of pale, pinkish-to-beige–colored, peloidal dolostone with wave-generated sedimentary structures (*97*, *130*, *154*). This so-called "cap dolostone" sharply overlies the last glacial and periglacial deposits without evident hiatus. It was deposited during glacioeustatic flooding resulting from global deglaciation (*154*–*156*). The date of Marinoan deglaciation is tightly constrained between 636.0 and 634.7 Ma by U-Pb (CA-ID-TIMS) zircon ages from volcanic ash layers within the youngest glacial deposits in Namibia and Australia and at the top of the cap dolostone in South China (Table 1). Because of the uncertainty in the date of its onset, the duration of the Marinoan cryochron is loosely constrained between 3.0 and 15.2 My. A thermal subsidence model of the carbonate passive margin (upper Otavi Group) in northern Namibia (*157*) implies ~6 My for the Marinoan cryochron together with its postglacial depositional sequence (Maieberg Formation), in which the cap dolostone forms the base.

The most striking aspect of the new Cryogenian chronology is the grossly unequal duration of the cryochrons (Fig. 2A). The Sturtian lasted 4 to 19 times longer than the Marinoan. This could be the result of a small difference in equatorial surface albedo, because surface warming has a logarithmic dependence on CO_2 concentration. Because CO_2

is assumed to have accumulated linearly or at a decreasing rate over time during a cryochron (*73*), subject to sequestering as CO_2 ice or consumption by seafloor weathering, as mentioned earlier, even a small increase in the radiative threshold for melting could require a long time to achieve because of the high CO_2 concentration required to trigger deglaciation (Fig. 1).

Another surprising aspect of the new chronology is the brevity of the nonglacial interlude between the cryochrons. When the Marinoan began, a Snowball Earth had terminated less than 20 My earlier. When the Sturtian began, no low-latitude glaciation had occurred for 1.7 Gy (Fig. 2B). Might this contrast in circumstance relate to the inequality of the cryochrons? Might it rationalize the geochemical distinctions between them (*130*, *131*, *158*)? Nearly all synglacial Cryogenian iron formations (Fig. 4) are Sturtian in age (*159*, *160*), whereas all known occurrences of barite ($BaSO_4$) in cap dolostones are Marinoan (*91*, *155*, *161*–*163*). Nearly all the isotopic evidence for anomalous atmospheric CO_2 comes from the shorter Marinoan cryochron (*86*) or its aftermath (*84*, *85*, *87*–*91*, *162*, *163*). This reflects the absence in the Sturtian of glaciolacustrine calcite and postglacial barite and the incomplete development of Sturtian cap-carbonate sequences, discussed later. There is no reason to assume that Sturtian deglaciation required less CO_2 than the Marinoan. The 10- to 20-My nonglacial interlude is of the same duration as the estimated time scale for the post-Snowball drawdown of atmospheric CO_2 (*164*).

The difference in cryochron duration should relate to the low-latitude albedo or to sinks for CO_2 that could retard its rise in the atmosphere. In many areas, geological observations imply that Sturtian glacial deposits accumulated during the active rifting of Rodinia (Fig. 5), whereas Marinoan ones accumulated during the drift stage of post-rift subsidence. If true, active rift flanks may have increased Sturtian paleotopography, resulting in more complete coverage of the continents by ice sheets (*165*, *166*), most importantly by glacial flow into the equatorial zone of sublimation. This would have raised the planetary albedo. Increasing the ice coverage would also reduce the atmospheric dust load, allowing long-wavelength radiation to escape more readily (*77*, *115*). A lower dust flux would additionally raise albedo in the sublimation zones of glaciers (*78*, *79*, *167*, *168*). More ice and less dust means that more CO_2 must accumulate to deglaciate (*116*).

If rift-related paleotopography was greater during the Sturtian cryochron, then erosion and sedimentation rates should have been greater as well. This prediction is not supported by data on their respective sediment accumulation rates (Fig. 6) (*169*). Sturtian sections have median and average thicknesses that are two and four times greater, respectively, than those of Marinoan sections. However, the average accumulation rate is actually lower for Sturtian than for Marinoan sections because of the disproportionate averaging times (Fig. 6) (*169*). The apparent contradiction could stem from a subtlety. Whereas it is the extent of ice that governs Snowball albedo and hence the CO_2 threshold for deglaciation, it is the flux of ice (at equilibrium lines) that appears to govern rates of erosion and sedimentation by active glaciers (*170*). More rugged Sturtian landscapes with more ice and less dust could be consistent with sedimentation rate data (Fig. 6) if Sturtian ice sheets were, on average, less dynamic. For example, modeling indicates that ice sheets are largest on Snowball Earth when CO_2 is low and the ice flux is weak (*100*). For this to occur, low surface temperatures and thus a feeble hydrologic cycle would need to be maintained (*81*) during much of the Sturtian cryochron. This scenario is unlikely: The most-rapid warming should occur at the start of a cryochron because of its logarithmic dependence on CO_2 and because of the pH dependence at low temperatures of CO_2 consumption by seafloor weathering (*76*).

Sinks for CO_2 on Snowball Earth include subglacial weathering of continental crust (*171*), including LIPs, low-temperature alteration of young oceanic crust on the flanks of seafloor spreading ridges (*75*, *76*, *172*, *173*), and organic burial (see the "Meltwater flushing, the carbon cycle, and atmospheric oxygen" section). Geochronologic and paleomagnetic data demonstrate that the windward margin of Rodinia in the deep tropics was resurfaced by flood basalt of the Franklin LIP (Fig. 5) just before the Sturtian glaciation (*32*). Nonradiogenic Sr, Os, and Nd isotope compositions in sediments show that LIP and/or seafloor weathering had been dominant for the preceding 15 My (*60*, *174*). It has been suggested that the removal of volcanic plateaus by Sturtian glacial erosion rendered continents less reactive, thereby accounting for the shorter duration of the Marinoan glaciation (*174*). A potential problem for this idea is that debris from the ca. 825-Ma Wooltana (LIP) volcanics in South Australia is prominent in both the Sturtian and

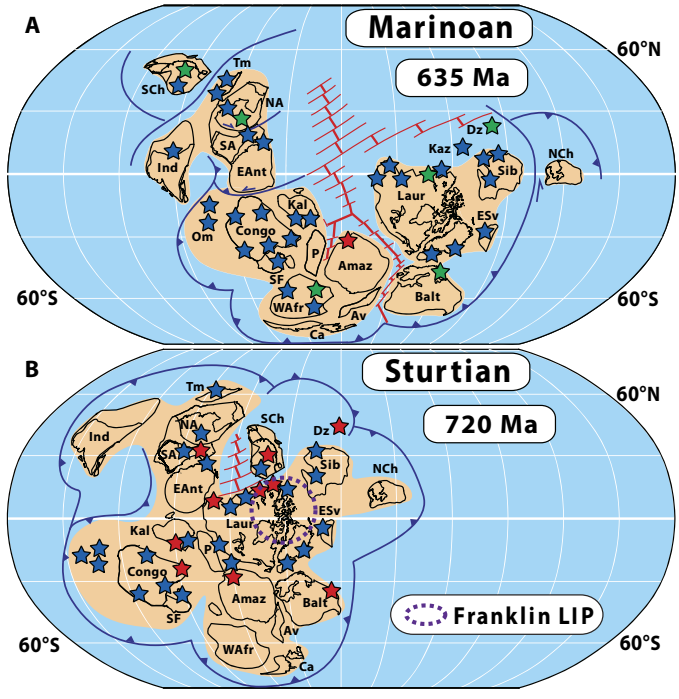

Fig. 5. Cryogenian paleogeography and the breakup of Rodinia. Global paleogeographic reconstructions in Mollweide projection for (**A**) Marinoan termination at 635 Ma and (**B**) Sturtian onset at 720 Ma (*34*). Red lines are oceanic spreading ridge-transform systems, and dark blue lines with barbs are inferred subduction zones. Stars are glacial-periglacial formations (Fig. 4), red stars are formations with synglacial iron formation, and green stars indicate occurrences of authigenic and/or seafloor barite in Marinoan postglacial cap dolostone (Fig. 4). Cryogenian glaciation was coeval with the breakup of supercontinent Rodinia. Paleocontinent Laurentia (Laur) is fixed in latitude and declination at 720 Ma by paleomagnetic data (n = 87 sites) from the Franklin LIP (purple dashed line) in Arctic Canada (*32*, *33*, *127*). Paleocontinents South Australia (SA) and South China (SCh) are similarly fixed at 635 Ma by paleomagnetic data from the Nuccaleena Formation cap dolostone (*33*) and the Nantuo Formation glacial diamictite (*368*), respectively. Other paleocontinents are Amazonia (Amaz), Avalonia (Av), Baltica (Balt), Cadomia (Ca), Congo, Dzabkhan (Dz) in Mongolia, East Antarctica (EAnt), East Svalbard (ESv), India (Ind), Kalahari (Kal), Kazakhstan (Kaz), North Australia (NA), North China (NCh), Oman (Om), Rio de la Plata (P), São Francisco (SF), Siberia (Sib), Tarim (Tm), and West Africa (WAfr). The paleolocation of Oman is uncertain; alternatively, it could restore west of India. The Sturtian location of South China opposite Laurentia is controversial; it might have been closer to its Marinoan position (*368*).

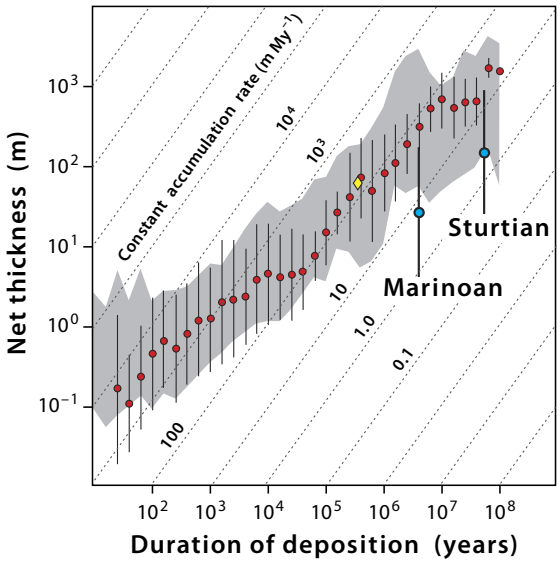

Fig. 6. Sediment accumulation rates during Cryogenian and younger glacial epochs (*169*). Comparison of stratigraphic thickness of Marinoan and Sturtian cryochrons (blue dots and whiskers: mean ± 1σ for 492 records) with Phanerozoic shallow glaciomarine accumulation (red dots: 6733 records) and nonglacigenic terrigenous shelf accumulation (gray: ±1σ band for 32,892 records), plotted by duration of deposition. The yellow diamond represents the 580-Ma Gaskiers glaciation (*247*). Comparison of comparable durations is mandated because accumulation rate (dashed contours in meters per million years) decreases as averaging time increases, due to stratigraphic incompleteness (*240*). Data are from Partin and Sadler (*169*) and Sadler and Jerolmack (*242*). Cryogenian glacial deposits accumulated 3 to 10 times more slowly than younger glacial deposits of comparable duration (*169*).

Marinoan glacial deposits in that region, although isotopic tracers globally become more radiogenic after the Sturtian glaciation, consistent with progressive LIP removal (*174*).

Paleogeography

Cryogenian glacial deposits (*28*, *175*) are reliably documented in >90 formations on 22 paleocontinents and microcontinents worldwide (Fig. 4). Areas where they are absent, such as northeastern North America, simply lack Cryogenian strata and should not be considered to have been ice-free. Certain Sturtian and Marinoan deposits were formed by glaciers that were grounded below sea level at low paleomagnetic latitudes (*28*, *31*, *33*, *34*). Glacial deposits of both cryochrons are bounded regionally by thick, shallow-water, nonskeletal, carbonate sequences (*24*, *25*, *34*, *143*, *144*, *176*). In both warm and cool global climates, nonskeletal carbonate production occurs preferentially in the warmest parts of the surface ocean (*177*, *178*), reflecting the temperature and inverse pressure dependence of carbonate saturation state. Moreover, broad carbonate platforms lack mountains from which glaciers could descend. This was the logic that justified the Snowball Earth hypothesis before proof of synchroneity was available. If the warmest surface areas were glaciated, then colder areas must also have been frozen.

Cryogenian glacial deposits can now be retrolocated on paleogeographic maps (Fig. 5), constructed by means of paleomagnetically constrained interpolation between an inferred configuration of the Rodinia supercontinent at 780 Ma and that of the Gondwana megacontinent at 520 Ma (*34*, *179*, *180*). The main uncertainty is Rodinia: Adopt a different configuration for Rodinia (*181*) and the specifics of Cryogenian paleogeography will be quite different, even if the generalities remain. Notable among the generalities are the absence of polar continents and the large low-latitude land area (Fig. 5).

In the absence of vascular plants, continental surface albedos were presumably higher than present-day albedos in the tropical and midlatitude wet zones, but transpiration and hence evaporative cooling were less. Silicate weathering and silicate-weathering feedback, the ultimate climate thermostat (*69*), may have been weaker in the absence of rooted plants (*22*), which increase soil acidity by CO_2 pumping and organic acid production. Rooted plants also stabilize hillslopes, which lengthens soil residence time in the weathering zone, but retards the entry of fresh rock into that zone. Higher atmospheric CO_2, adjusted to the 6 to 7% dimmer Cryogenian Sun (*69*), would have lowered soil-water pH, offsetting the absence of rooted plants to some degree. Lower seawater pH would have enhanced seafloor weathering at low temperatures (*172*, *173*), but the enlarged ocean-atmosphere C reservoir would have weakened the silicate-weathering feedback because of the climate's logarithmic dependence on CO_2.

The tropical bias in Cryogenian continentality is postulated to have lowered global surface temperatures by raising the planetary albedo (*24*). Experiments with a coupled atmosphere-ocean GCM, ECHAM5/MPI-OM, support this supposition, yielding a global mean surface temperature with Cryogenian paleogeography ~3°C lower than present, because of both higher albedo and suppressed water-vapor greenhouse (*18*). However, the problem is not a simple one—Tropical continents also suppress evaporative cooling (*182*), and an absence of high-latitude continents reduces summer snow cover, leading to warmer high-latitude oceans and less sea ice (*183*). Experiments with an atmospheric GCM, CAM3.1, coupled to a mixed-layer ocean model and a land model, CLM (community land model), yield a warmer-than-present climate with Cryogenian paleogeography because of decreased tropical cloud cover over land and intensification of the Walker circulation, leading to more (rather than less) water-vapor greenhouse (*184*). However, on the time scale of the geochemical cycle of carbon, more continental area in the deep wet tropics should yield a globally colder climate because of enhanced silicate weathering (*185*).

The change in paleogeography over the Cryogenian period (Fig. 5) reflects the breakup of the Rodinia supercontinent at this time. The breakup presumably reduced CO_2 greenhouse warming in two ways. First, moistening of previously arid lands in the supercontinental interior adjusted CO_2 to a lower level because of increased weathering efficiency (*186*), defined as the silicate weathering rate globally at any given CO_2 level. A less marked cooling followed the breakup of Pangea (*187*), perhaps because an equatorial ocean (Tethys) already existed within the Pangea supercontinent and because of the low albedo of tropical forests, nonexistent during the Cryogenian period. Second, the total length of all continental margins rose, resulting in higher rates of global sediment accumulation and consequently organic burial (*188*, *189*). The apparent absence of polar continents in Cryogenian paleogeography (Fig. 5) weakened the protection against uncontrolled cooling normally afforded by silicate-weathering feedback. If global weathering rate declines because of the glaciation of polar continents, then atmospheric CO_2 stabilizes or even rises. When polar continents are absent, this protective feedback vanishes (*190*). The ice-albedo feedback is then driven by oceanic ice (that is, sea ice plus shelf ice) alone, and the Snowball bifurcation (Fig. 1, point a) can be reached with little prior development of grounded ice sheets (*18*). This may explain why regional-scale ice ages (Fig. 2) have not been observed in Cryogenian time.

The Rodinia breakup was also associated with the emplacement of basaltic LIPs at ~825 Ma (Guibei-Willouran LIP), ~800 Ma (Suxiong-Xiaofeng LIP), ~775 Ma (Gunbarrel-Kinding LIP), ~755 Ma (Mundine Well LIP), and ~717 Ma (Franklin LIP). The last one was emplaced squarely across the paleoequator (*34*, *35*, *127*, *191*). Weathering of basaltic rock consumes CO_2 more rapidly than weathering average upper continental crust [(*192*, *193*); but see the study by Jacobson *et al.* (*194*)], and basalt weathers most rapidly at high temperatures (*195*). Basaltic rocks including pre-Sturtian LIPs are strongly enriched in phosphorus relative to average upper crust, possibly leading to enhanced organic productivity and burial (*193*, *196*), depending on the controls of apatite dissolution kinetics (that is, grain size and soil-water pH). Elevated rates of fractional organic burial are indicated by enriched C isotopes ($\delta^{13}C \geq$ 5‰ Vienna Pee Dee belemnite) in marine carbonate deposited from ~825 to 717 Ma [(*174*, *197*); but see the study by Shields and Mills (*198*)]. Enhanced weathering of young basaltic rocks is supported by relatively nonradiogenic Sr, Os, and Nd isotopic compositions observed in pre-Sturtian carbonate, organic matter, and shale, respectively (*60*, *174*, *197*). Enhanced CO_2 consumption and global cooling due to the breakup of the Rodinia supercontinent and the emplacement of a temporal cluster of LIPs (*174*, *186*, *196*, *199*) purportedly moved the climate system closer to the Snowball bifurcation (Fig. 1).

The synchroneity of Franklin LIP emplacement with the onset of low-latitude glaciation (*32*) raises the possibility that volcanism was the proximal trigger for the Sturtian cryochron (*200*). Historical flood-basalt fissure eruptions generated thermal plumes that injected sulfate aerosol precursor gases (SO_2 and H_2S) into the stratosphere intermittently for months (*201*), and more voluminous LIP eruptions likely extended this time scale to years (*202*). Many Franklin LIP sills and dykes are highly enriched in S, 10^2 to 10^5 ppm (*203*), because of contamination by sulfate evaporites they intrude within the pre-Sturtian Neoproterozoic Shaler Supergroup (*204*). Sulfur chemistry, aerosol microphysics, and radiative energy-balance modeling (*200*) reveal the importance of the ambient climate and the paleolatitude of eruption. A cold pre-Sturtian climate, related to the Rodinia breakup, was vulnerable to stratospheric aerosol forcing because the tropopause was lower in elevation and the ocean mixed layer was closer to the freezing point (*200*). Sulfate aerosol increases the planetary albedo, and the resultant cooling effect is maximized if injection occurs at low latitudes, where insolation is strongest (*200*). Accordingly, the Franklin LIP had unique climatic consequences because S-rich lavas were erupted at high rates at the paleoequator in an already-cold climate. Concurrent CO_2 emissions were small, relative to an ambient atmospheric reservoir of ≤3000 ppm (*200*), and were compensated by enhanced weathering on the time scale of LIP emplacement.

ATMOSPHERE DYNAMICS AND THE HYDROLOGIC CYCLE

A variety of geological features—erratic blocks (*205*), striated pavements (Fig. 7A) (*98*, *206*–*208*), moraines (*98*, *206*), faceted and striated clasts (*209*), preferred clast orientation (*92*, *102*), periglacial loessite (*210*), U-shaped paleovalleys (*95*, *211*–*213*), glacitectonic deformation (*102*, *214*), and glacial seismites (*215*)—demonstrate that Cryogenian glaciers and ice sheets were dynamic. Erosion and transport may have been achieved locally by marine ice, by means of the "sea-ice escalator" (*109*, *216*–*218*). However, provenance indicators and depositional facies relations imply that the dominant agents of erosion and transport were grounded ice masses and their floating extensions (*92*, *93*, *95*–*100*, *219*, *220*).

Whether dynamic ice sheets are compatible with a frozen ocean was among the first issues that arose when the Snowball concept was applied to Cryogenian glacial deposits (*217*, *221*). The issue boils down to the following. Can the Snowball atmosphere drive a hydrologic cycle capable of building ice sheets thick enough to reach the pressure-melting point at the base of the ice sheet and thereby accommodate flow by basal sliding? The ice need not slide everywhere: Large ice sheets that accumulate slowly may largely drain through narrow ice streams (*222*, *223*). The time frame for ice-sheet buildup is generous (Fig. 2A), with the Marinoan cryochron providing a somewhat tighter bound (3.0 to 15.2 My) than its ponderous predecessor. The geological evidence for dynamic ice is equally compelling in both cryochrons.

Atmosphere dynamics

The Snowball atmosphere has been simulated in six different GCMs under identically prescribed, 100% ice-covered conditions (Figs. 8 and 9; see figure captions for model identities) (*80*, *81*). To isolate differences in atmospheric behavior among the models, surface albedo was set to 0.6 everywhere, eliminating differences between ablative and snow-covered ice. The prescribed albedo is appropriate for cold, ablative, meteoric ice that is free of dust and snow (*224*, *225*). Topography and aerosols were set to zero, as were all greenhouse gases other than CO_2 and H_2O. The solar constant was set to 94% (present-day value; 1285 W m^{-2}), obliquity was set to 23.5°, and eccentricity was set to zero. The models were run at CO_2 equal to 0.1 and 100 mbar to simulate conditions soon after a Snowball onset and just before its termination, respectively.

Because the solid surface has little thermal inertia, surface temperatures closely track the instantaneous insolation forcing (*81*, *116*, *226*–*229*). Diurnal and seasonal cycles are amplified. At solstice (Fig. 8B), temperatures are uniformly warm (relatively speaking) in the summer hemisphere, whereas the winter hemisphere becomes extremely cold. The seasonal temperature change is large at all latitudes, consistent with geological evidence such as periglacial sand-wedge structures at low paleomagnetic latitudes (*230*–*233*), obviating the need for high orbital obliquity (*231*, *233*). Temperature inversions develop in the winter hemisphere (*81*, *116*, *226*, *228*), decoupling the surface from winds and from the greenhouse effect (*81*), which is set by the radiative balance at the top of the atmosphere (*234*).

The Snowball atmosphere (*80*–*82*, *116*, *226*–*229*) is cold, due to high planetary albedo, and therefore holds little moisture. Latent heat contributes little to convection. The solstitial height of the equatorial tropopause is only 6 to 8 km above sea level (*81*), ~10 km less than in the present (geologically cold) climate. Outside the tropics, circulation is weak and dominated by subsidence in winter (Fig. 9, A to D). The Hadley circulation, although shallower than in the modern tropics, is actually significantly stronger (Fig. 9, A to D) (*80*–*82*, *228*, *229*, *235*). Vertical transport of moisture is much smaller than in the modern tropics, because the air is dry. Consequently, the ascending branch must be stronger to move enough heat to balance radiative cooling aloft (*82*).

The zone of ascending air is closely tied to the zone of maximum insolation because of the low thermal inertia of the solid surface. When the ascending branch moves off the equator during the seasonal cycle, the equator falls under the descending branch of the Hadley cell (Fig. 9, A and B). Because the ascending branch spends more time away from the equator than above it, the annual mean Hadley circulation (Fig. 9, C and D) is characterized by equatorial downwelling and subtropical upwelling (*81*, *116*). This "reverse" Hadley circulation is unlike any (low-obliquity) climate with tropical surface water (*236*, *237*) and is more like the present climate of Mars (*238*) but with a denser atmosphere.

One of the GCMs, FOAM, is an outlier, yielding tropical surface temperatures 7 to 11 K colder than the other models (Fig. 8, A and B),

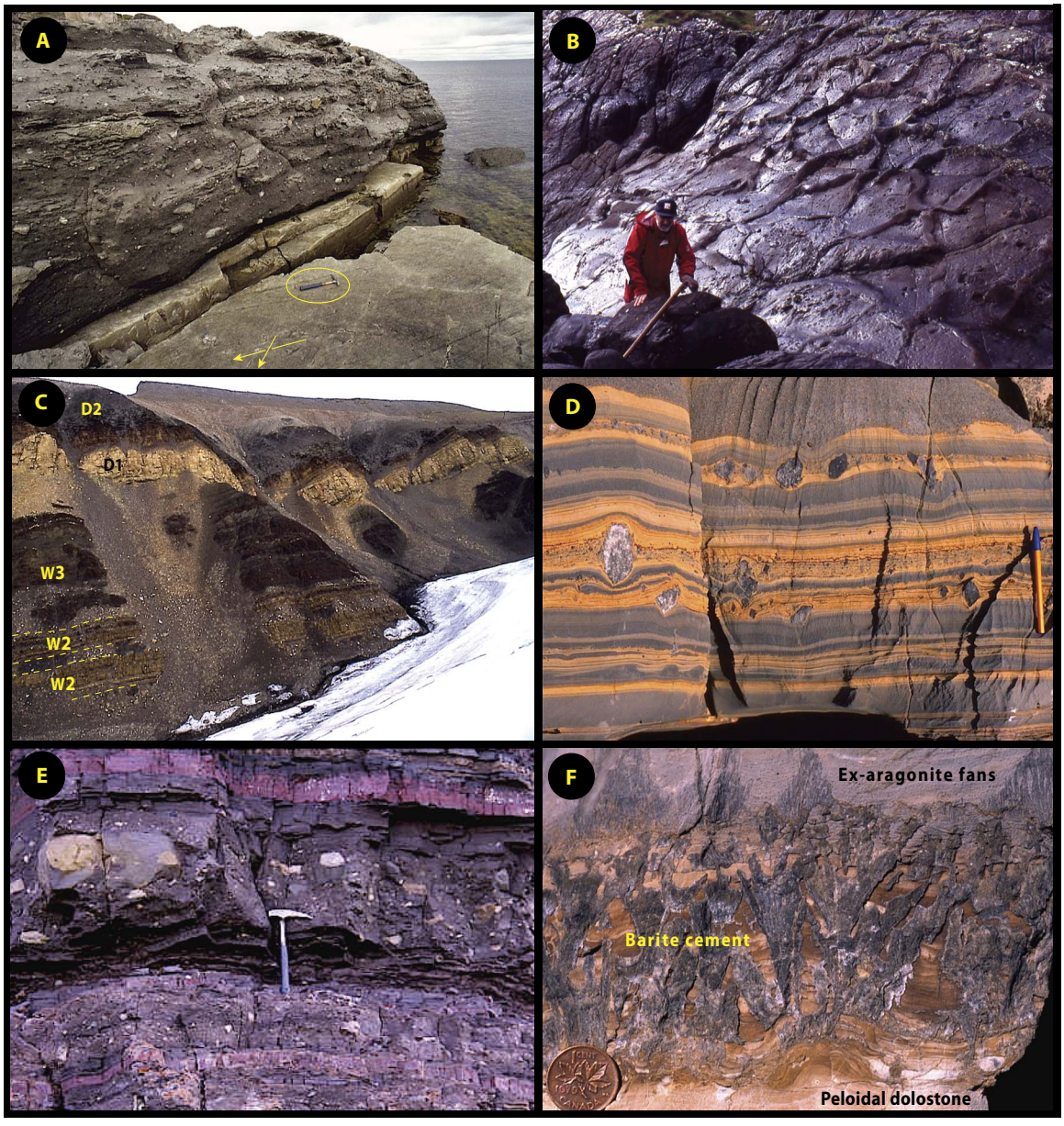

Fig. 7. Images of the Cryogenian sedimentary record. (**A**) Marinoan moraine (Smalfjord Formation) resting on a quartzite bedrock pavement bearing two sets of glacial striations (arrows) in a shallow-marine paleoenvironment at Bigganjar'ga, Varanger Peninsula, Finnmark, North Norway (*93*, *98*, *206*). View looking eastward; 33-cm-long hammer (circled) for scale. (**B**) Polygonal sand wedges indicating subaerial exposure on the upper surface of a Sturtian glacial tillite (Port Askaig Formation), formed when glacial ice advanced across and later retreated from the paleosouthern, subtropical marine shelf of Laurentia, Garvellach Islands, Firth of Lorn, west of Scotland (*92*, *485*). A. M. (Tony) Spencer is seen in the lower left. (**C**) Marinoan glacial and glaciolacustrine sequence (Wilsonbreen Formation) at Ditlovtoppen, Ny Friesland, Svalbard. Glaciolacustrine carbonates (W2) yield mass-dependent and mass-independent sulfate-oxygen isotopic evidence for evaporation of liquid water and extreme atmospheric CO_2 concentration, respectively, indicating ice-free conditions shortly before the Marinoan glacial termination (*86*, *88*, *100*). Glacial readvance is recorded by diamictite (W3), followed by syndeglacial cap dolostone (D1) and organic-rich shale (D2) associated with the postglacial marine inundation (Dracoisen Formation) (*486*–*488*). (**D**) Stratified marine periglacial carbonate diamictite from the Marinoan ice grounding-zone wedge (Ghaub Formation) on the foreslope of the Otavi Group carbonate platform (Congo craton), northern Namibia (*96*, *97*). The pen is 15 cm long. Parallel-laminated lutite (orange) with ice-rafted debris accumulated slowly as fallout from meltwater suspension plumes, whereas graded arenite beds (gray) lacking ice-rafted debris were deposited rapidly from turbidity currents. Carbonate detritus was generated by glacial flow across a carbonate platform developed during the Cryogenian nonglacial interlude (Fig. 2A). (**E**) Beds of hematite-jasper (Fe_2O_3 + SiO_2) iron formation ("jaspilite") within stratified, ice-proximal, glaciomarine diamictite of the Sayunei Formation (Rapitan Group), Iron Creek, Mackenzie Mountains, Yukon, Canada. Stratigraphic context, Fe isotopes, and cerium anomaly data imply that the iron formation accumulated in a silled and likely ice-covered basin where ferruginous deep water mixed into oxygenated meltwater sourced at an advancing ice grounding line (*160*, *220*, *350*, *400*, *412*). Sedimentary iron formation is widely distributed in Sturtian but not Marinoan glaciomarine sequences (Figs. 4 and 5). (**F**) Seafloor barite ($BaSO_4$) precipitated at a regionally extensive horizon at the top of the Marinoan syndeglacial cap dolostone (Ravensthroat Formation), Shale Lake, Mackenzie Mountains, Northwest Territories, Canada. The coin is 2 cm in diamater. Seafloor and authigenic barite is widespread in Marinoan but not Sturtian cap carbonates (Figs. 4 and 5). Triple O isotope and multiple S isotopes from Ravensthroat barite constrain atmospheric CO_2, the size of the seawater sulfate reservoir, the elimination of the atmospheric $\Delta^{17}O$ anomaly, and the time scale for cap dolostone sedimentation (*91*).

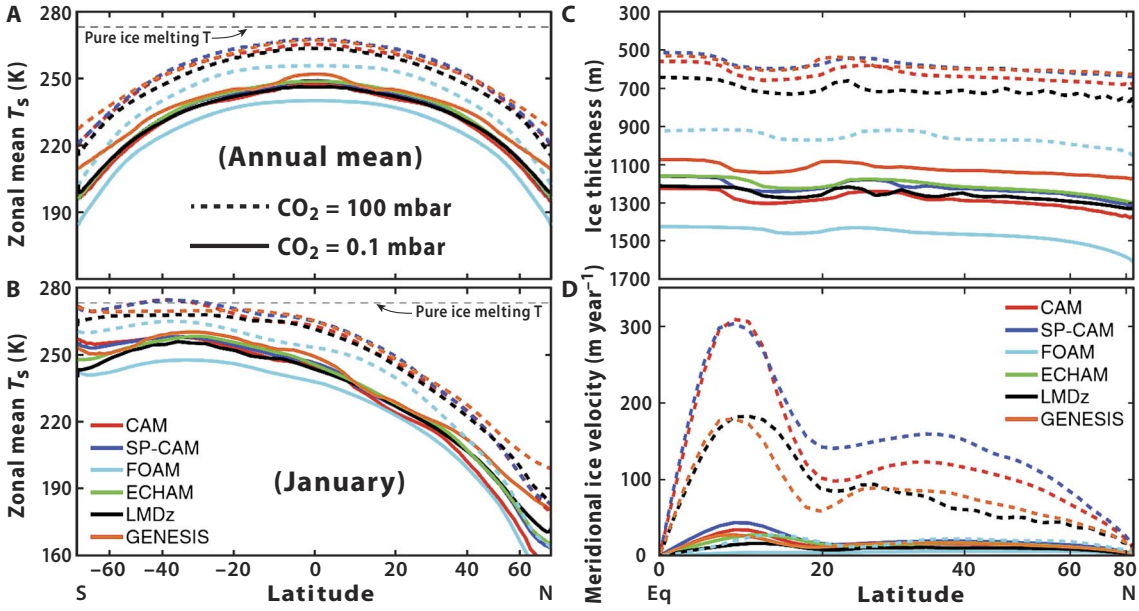

Fig. 8. Snowball Earth intermodel comparison (*81*). Colors assigned each GCM as indicated in (B). Solid lines, CO_2 = 0.1 mbar; dashed lines, CO_2 = 100 mbar. To isolate differences in atmospheric behavior among models, surface albedo was set to 0.6 everywhere, eliminating differences between ablative and snow-covered ice. Topography and the radiative effect of aerosols were set to zero, as were all greenhouse gases other than CO_2 and H_2O. The solar constant was set to 94% (present-day value; 1285 W m^{-2}), obliquity was set to 23.5°, and eccentricity was set to zero. (**A**) Annual and zonal mean surface temperature. (**B**) January zonal mean surface temperature. (**C**) Sea-glacier thickness in meters (increasing downward to simulate depth below the ice surface). (**D**) Meridional (equatorward) ice velocity in meters per year. Models used are as follows: CAM (Community Atmosphere Model) (*489*), SP-CAM (Super-Parameterized Community Atmosphere Model) (*490*, *491*), FOAM (Fast Ocean Atmosphere Model) (*492*), ECHAM (European Centre Hamburg Model) (*493*), LMDz (Laboratoire Météorologie Dynamique Zoom) (*256*), and GENESIS (Global Environmental and Ecological Simulation of Interactive Systems) (*494*, *495*). FOAM produces surface temperatures substantially lower than those of other models and ice was accordingly thicker and slower. This is because FOAM is essentially a cloud-free model under Snowball conditions, accounting for its anomalous resistance to deglaciation at a geologically feasible CO_2 level (*80*, *82*, *228*).

equivalent to changing CO_2 by a factor of 10 to 100 (*80*–*82*). FOAM remains far below the deglaciation point at any geologically feasible CO_2 level, even with prescribed albedos of 0.5 and 0.75 (broadband average) for ablative and snow-covered ice surfaces, respectively (*227*). The reason is that FOAM underpredicts absorption of outgoing long-wavelength radiation by cloud condensate, for example, ice particles (*80*–*82*, *116*). This was originally considered to be unimportant because the dry Snowball atmosphere was assumed to lack optically thick clouds (*227*, *228*). However, a cloud-resolving model (System for Atmospheric Modeling, version 6.10.4) produces ≥10 W m^{-2} of cloud radiative forcing under a wide range of microphysical parameters (*82*), consistent with the non-FOAM GCM results (Figs. 8 and 9) using the same uniform 0.6 surface albedo. This implies that Snowball deglaciation is not problematic from a modeling perspective, given the geological constraints on cryochron duration (Table 1) and CO_2 concentration (*85*–*91*).

Snowball hydrologic cycle

The Snowball atmosphere is dry because it is cold, not because sources of water vapor are absent. The saturation water-vapor pressure is exponentially dependent on temperature (Clausius-Clapeyron relation) but is not much lower over ice than over supercooled water of equal temperature. The latent heats of evaporation and sublimation (direct conversion of ice to water vapor) differ by only 13.2%. Sublimation of ice is therefore a viable source of water vapor. Because of the "reversed" Hadley circulation, the main source of water vapor on Snowball Earth is equatorial sea ice, and the zones of highest net accumulation are the inner subtropics (Fig. 9, E and F). Narrow secondary bands of net sublimation occur at ~25° latitude, possibly related to export of moist air by mid-latitude eddies (*235*). Beyond that latitude, a low rate of net accumulation occurs everywhere, and the polar deserts of the modern climate are absent (*81*).

At low CO_2 (0.1 mbar), ice-equivalent accumulation rates outside the tropics in the (non-FOAM) GCMs (Fig. 9E) are on the order of 1.0 mm year^{-1} (~1.0 km My^{-1}), whereas rates in the inner subtropics reach a few centimeters per year or a few kilometers every 100 ky. These rates increase around fivefold when CO_2 is raised to 100 mbar (Fig. 9F). The rates pertain to sea level (sea ice) and cannot be directly extrapolated to the elevated surfaces of grounded ice sheets. Early studies of ice-sheet development in atmospheric GCMs with Cryogenian paleogeography suggested that tropical ice sheets would thicken and achieve a dynamic steady state within a few 100 ky after the tropical ocean froze over (*165*, *239*). This implies that glacial erosion and sedimentation occur continuously during most of the time span of a Snowball cryochron. However, this conclusion was tentative because the simulated air circulation and precipitation patterns in the early studies (*165*, *239*) were not iteratively coupled to ice-sheet topographic development. New modeling with improved coupling will be described in the "Ice-sheet stability and extent under precession-like forcing and variable CO_2" section.

Because erosion and sedimentation rates appear to scale with the ice flux at the equilibrium line in active glaciers (*170*), we expect these rates to increase over the course of a Snowball cryochron (Figs. 8 and 9). However, the average rates over entire cryochrons are expected to be smaller than for regional-scale glaciations because of the relatively weak hydrological cycle (*81*). With the development of a Cryogenian radiometric

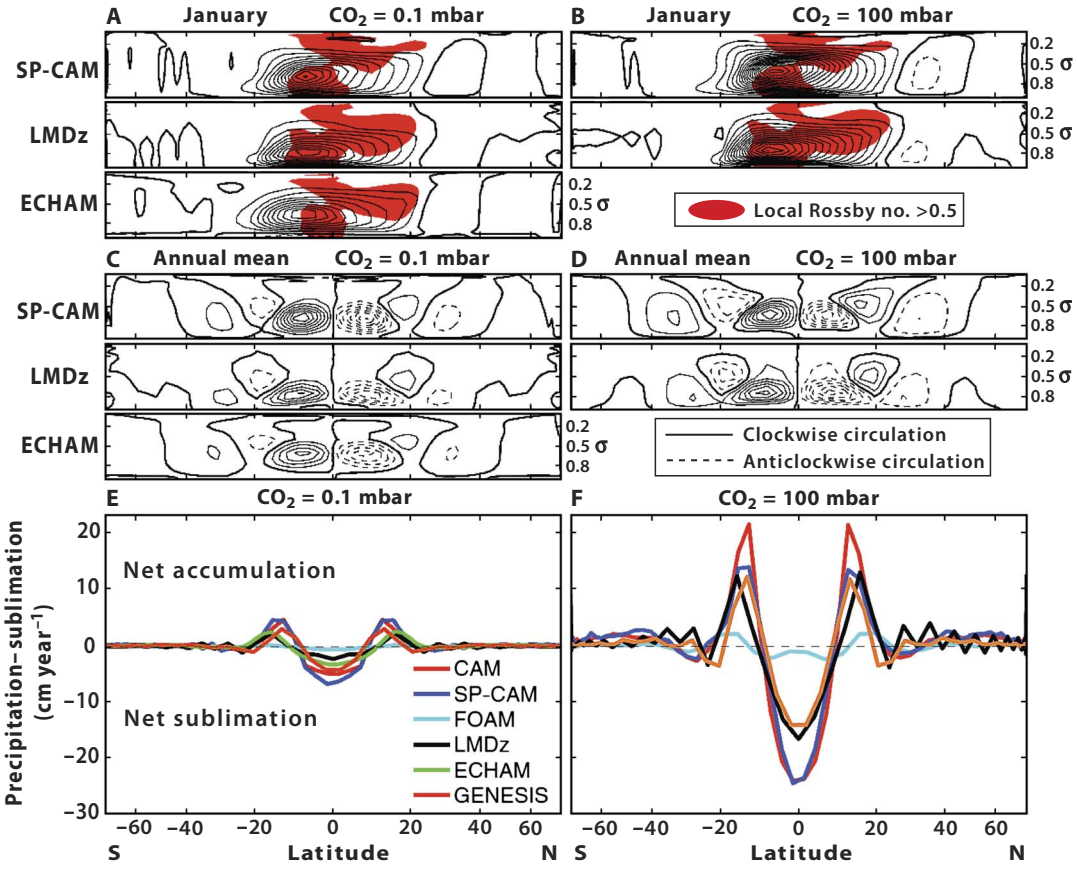

Fig. 9. More Snowball Earth intermodel comparisons (*81*). See Fig. 8 caption for the prescribed conditions. January mean mass Eulerian stream function for models SP-CAM, LMDz, and ECHAM at (**A**) CO_2 = 0.1 mbar and (**B**) CO_2 = 100 mbar. σ is air pressure as a fraction of the surface air pressure. Clockwise atmospheric circulation is depicted by thin solid lines, counterclockwise circulation is depicted by thin dashed lines, and the zero stream function is depicted by thick solid lines. Contour interval is 50×10^9 kg s^{-1}. Maximum mass stream functions in January increase by a factor of ~1.5 between 0.1 and 100 mbar of CO_2. ECHAM is unstable at CO_2 = 100 mbar. Note the ascending flow in January between 10°S and 30°S and the descending flow between 10°S and 20°N. Red shade indicates regions where the local Rossby number is greater than 0.5, meaning that inertial forces dominate over Coriolis forces. (**C** and **D**) Same as (A) and (B) but depict the annual mean mass Eulerian stream function. Contour interval is 20×10^9 kg s^{-1}. Note that air descends in the inner tropics in the annual mean and ascends in the subtropics. This governs the surface hydrologic balance (E and F). Annual and zonal mean precipitation minus sublimation with (**E**) CO_2 = 0.1 mbar and (**F**) CO_2 = 100 mbar. Note the net sublimation in the inner tropics and the net accumulation in the near subtropics, opposite to the present climate. The hydrologic cycle amplifies by nearly a factor of 10 between 0.1 and 100 mbar of CO_2 but is muted in FOAM due to cold surface temperatures (Fig. 8, A and B). LMDz exhibits grid-scale noise in (F).

chronology (Table 1), average sediment accumulation rates over entire cryochrons can now be calculated because the synglacial strata are generally well defined stratigraphically (*175*). Average accumulation rates for all sediments decline as averaging times increase (Fig. 6) because of stratigraphic incompleteness (*240*–*242*). Therefore, Cryogenian accumulation rates should only be compared with younger glacial regimes of comparable duration (Fig. 6) (*169*). The East Antarctic Ice Sheet, for example, has been in continuous existence for 14 My (*243*, *244*), which is close to the maximum duration of the Marinoan cryochron. Late Paleozoic glaciation of polar Gondwana caused the global mean sea level to fluctuate by ≥40 m on orbital time scales from late Viséan through end-Kungurian time (*245*), an interval of ~65 My that exceeds the Sturtian cryochron in duration. Smaller sea-level fluctuations are inferred at times within this interval (*246*), but it is unclear whether they imply less ice or smaller orbital-scale fluctuations.

The observed contrast between Cryogenian and younger glacial accumulation rates (Fig. 6) is striking (*169*). On average, Cryogenian accumulation rates were 3 to 10 times slower than for younger glaciations of comparable duration. This is remarkable given that the Phanerozoic data with long averaging times come exclusively from polar glaciations, Paleozoic Gondwana and Cenozoic Antarctica, whereas the Cryogenian data come from low to mid-paleolatitudes (*169*). Representing a database of 242 Sturtian and 326 Marinoan measured sections—incomplete, poorly exposed, and zero-thickness sections excluded—the anomalous Cryogenian accumulation rates are most readily explained by the attenuated hydrologic cycle of the "hard" Snowball Earth (*169*). In contrast, the sediment accumulation rate averaged over the short-lived (<350 ky), mid-latitude, 580-Ma Gaskiers glaciation (*247*) is indistinguishable from that of Cenozoic glaciations (Fig. 6). The Cryogenian data (*169*) also allow for the possibility (to be discussed in the next section) that low-latitude ice sheets on Snowball Earth may have receded well before the cryochron-ending deglaciation of the ocean (*100*).

CONTINENTAL ICE SHEETS, DRY VALLEYS, AND SAND SEAS

Depositional cycles and ice-sheet stability

Cryogenian glacial and glacial marine deposits commonly display vertical alternations of distal and more proximal deposits that are interpreted

to reflect repetitive advances and retreats of ice margins or grounding lines. The scale of these apparent cycles is broadly comparable to that of orbital cycles in Cenozoic periglacial sequences, but their frequency in the Cryogenian is unknown. During the Sturtian cryochron on the southern subtropical margin of Laurentia (Fig. 5B), for example, grounded ice flowing from the continental interior advanced across a former carbonate-rich, shallow-water marine shelf. The ice left stacked tabular bodies of ice-proximal (rain-out) and ice-contact (melt-out) diamictites, the Port Askaig Formation, with deformed zones attributable to overriding ice (*92*). No fewer than 13 of the diamictite bodies have their upper surfaces ornamented by polygonal sand wedges (Fig. 7C). The sand wedges indicate subaerial exposure in a periglacial environment, evincing withdrawal of the ice that deposited the diamictite on which the sand wedges developed (*92*). In the absence of a detailed chronology, we cannot say whether the migrations of the ice margin were externally forced (for example, orbital) or an expression of ice-sheet dynamics. Polythermal ice sheets in cold climates may undergo repeated surge-retreat cycles due to internal dynamics without external forcing (*248*, *249*).

Likewise, during the Marinoan cryochron, grounded ice flowed off the subtropical northeastern (present southwestern) margin of the Congo craton (Fig. 5A), leaving a compound ice grounding-zone wedge, the Ghaub Formation, on the steep foreslope of a wide carbonate shelf (*96*, *97*). The wedge formed where inland ice flowed across a grounding line into a floating ice shelf. The wedge is composed of interfingered massive and stratified carbonate diamictites, with a terminal ferruginous drape (Bethanis Member) crowded with ice-rafted debris. The massive diamictites include melt-out and rain-out deposits, locally channelized by well-sorted deposits or deformed by overriding ice (*96*). The stratified diamictites (Fig. 7D) accumulated subaqueously in a marine setting and are products of three simultaneous depositional processes: fall-out from fine-grained suspension plumes, mass flows (turbidites and debrites), and ice-rafted dropstones. Ice rafting could have been accomplished by icebergs or by a continuous ice shelf, except for the terminal drape, in which nested dropstones are more consistent with iceberg rafting (*250*). Well-sorted, carbonate sand and gravel form channels within massive diamictites and fans in stratified diamictites. The channels and fans contain dropstones and attest to subglacial meltwater flow and discharge at the grounding line, respectively. The cycles are typically asymmetric, recording progressive grounding-line advances punctuated by abrupt retreats. The grounding-zone wedge rests on an apparent ice-cut surface, implying an older ice maximum (*222*). The wedge pinches out upslope and tapers downslope but continues for hundreds of kilometers along strike. The grounding-line migrations were apparently limited to the width of the wedge, consistent with the steep inclination of the subglacial surface and the absence of reverse bed slopes in the foreslope area (*97*, *251*).

Cyclical instability of ice-sheet margins and grounding lines, as described above, was long assumed to be incompatible with the weak hydrologic cycle of a Snowball Earth (*95*, *113*, *218*, *252*–*255*). A new GCM investigation of ice-sheet mass balance on Snowball Earth implies a strong sensitivity to orbital forcing at intermediate CO_2 levels (*100*).

Ice-sheet stability and extent under precession-like forcing and variable CO_2

To investigate the ice-sheet response to orbital forcing and CO_2 variation on Snowball Earth, experiments have been conducted with a 3D atmospheric model coupled to an ice-sheet model in Marinoan paleogeography (*31*) with prescribed mountain ranges (*100*). The oceanic component of the climate model is turned off because the ocean is prescriptively ice-covered. The atmospheric model (LMDz) (*256*) and ice-sheet model [Grenoble Ice Shelf and Land Ice (GRISLI)] (*257*) are the same ones prescribed in an earlier study (*165*) with 0.33 mbar of CO_2, 94% of present solar luminosity, and the present orbital configuration and day length. In response, the model oceans are frozen, and ice sheets that had been "seeded" on the mountains extend over all tropical and most mid-latitude continents within 0.2 My, leaving bare only some coastal strips (*165*). The new experiments (*100*) seek to compare equilibrium ice-sheet volumes at different CO_2 levels, as well as the response of the ice sheets to orbital-like forcing at each level. To expedite ice-sheet initialization, ablation is eliminated for the first 500 ky, prescribed with present orbital parameters and low CO_2 (0.1 mbar). The models are incrementally coupled every 10 ky. Ablation is introduced at 500 ky, after which the ice sheets wane toward equilibrium volumes at prescribed CO_2 levels of 0.1, 20, 50, and 100 mbar. The coupling interval for this phase is 100 ky. At 0.1 mbar, the model converges on an ice volume close to that found in an earlier study (*165*) within 600 ky after ablation is introduced. The presence of mountains causes ice to overrun the low-latitude zone of net ablation. At each progressively higher CO_2 level, the equilibrium ice volume diminishes (Fig. 10). At 100 mbar, it is <20% of the equilibrium ice volume at 0.1 mbar and is largely controlled by topography (*100*).

To investigate the sensitivity of ice sheets on Snowball Earth to orbital forcing, integrations at each CO_2 level have been performed in which warm and cold summer orbits are switched reciprocally in each hemisphere every 10 ky (*100*). Precession-like forcing is chosen to investigate ice-sheet response in the tropics, where obliquity forcing is found to be weakest, as expected. Switching between orbital extremes, while not realistic, is computationally efficient and demonstrates that the ice-sheet response can outpace sinusoidal precession of the ecliptic. The atmosphere and ice-sheet models are coupled every 10 ky, which may dampen the ice-sheet response slightly compared with more frequent coupling, because of the delayed ice-elevation feedback. The observed response is strongly CO_2-dependent. At the lowest level (0.1 mbar), the ice sheets are unresponsive to orbital switching on a precessional time scale. At intermediate levels, the ice response is strong, and tropical ice-sheet margins migrate as far as 5° (550 km) latitude at 20 mbar (Fig. 11D). Ice volume increases in the cold-summer hemisphere, as expected for precessional forcing, but the response is spatially complex with simultaneous positive and negative mass balance in different areas of each hemisphere (Fig. 11C). At 100 mbar, the response weakens again because the amount of remaining ice is small (Fig. 10D). The sensitivity of ice-sheet margins to precession-like forcing at intermediate CO_2 supports a possible orbital origin for depositional cycles in Cryogenian glacial-periglacial sequences (*100*). It is also consistent with a U-Pb zircon age of 640.3 ± 0.4 Ma, 4 to 6 My older than the Marinoan termination, from a tuff at a stratigraphically intermediate level within the ice grounding-zone wedge on the Congo foreslope (*83*). The magnitude of the flooding events associated with both Cryogenian glacial terminations implies the existence of more ice than modeled at 100 mbar of CO_2 (Fig. 10D). Additional modeling is needed to see whether deglaciation can be triggered at lower CO_2 and a larger ice-sheet volume, possibly by lowering the equatorial oceanic ice albedo, as discussed in the "Cryoconite holes and ponds" section.

Ice-free terrestrial environments

Geological evidence supports the existence of ice-free land areas on Snowball Earth with surface temperatures near the melting point,

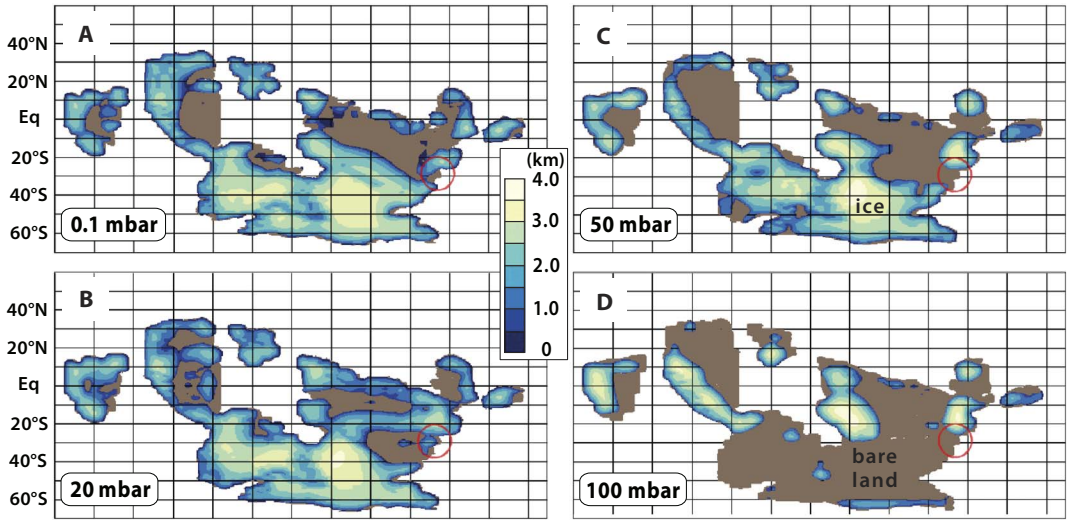

Fig. 10. Ice-sheet recession on Snowball Earth with rising CO_2 (*100*). Results from experiments with the atmospheric component of GCM LMDz, coupled to ice-sheet model GRISLI, in Cryogenian paleogeography with prescribed orography under Snowball conditions with present-day orbit and CO_2 = 0.1 mbar (**A**), 20 mbar (**B**), 50 mbar (**C**), and 100 mbar (**D**). Scale bar is ice-sheet thickness (in kilometers), and brown areas are ice-free. Red circles indicate the study location in Svalbard. Large base-level rise associated with Marinoan deglaciation may imply that more ice was available for melting than in (D), consistent with terminal deglaciation at less than 100 mbar of CO_2.

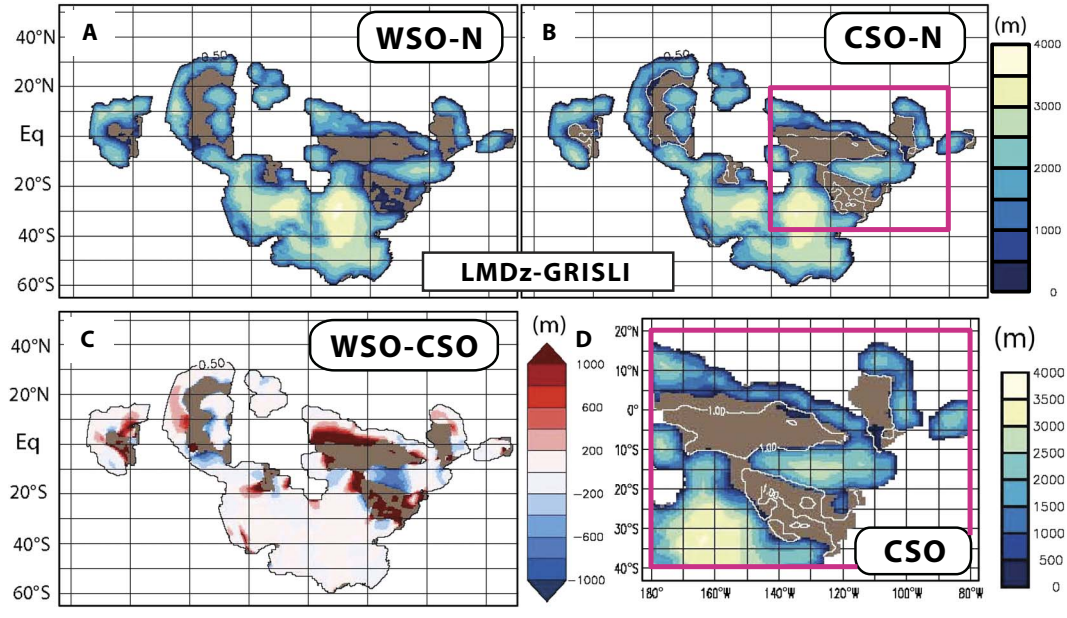

Fig. 11. Sensitivity of ice sheets on Snowball Earth to precession-like forcing (*100*). Same coupled atmosphere–ice-sheet model as in Fig. 10, with CO_2 = 20 mbar. Model equilibrated to northern-hemisphere (**A**) warm (WSO-N) and (**B**) cold (CSO-N) summer orbits. Orbits were switched every 10 ky. Scale bars are ice thickness (in meters), and brown areas are ice-free. (**C**) Difference in local ice-sheet mass balance, with red and blue indicating positive and negative mass balance, respectively, in the WSO-N relative to CSO-N. Note the hemispheric asymmetry as expected for precession, but areas of positive and negative mass balance coexist in both hemispheres at low latitudes, expressing the sensitive response of the hydrologic cycle. Positive mass balance in the war-summer hemisphere is related to prescribed change in eccentricity. (**D**) Expanded sector (magenta box) under CSO-N with white lines indicating ice margins under WSO-N for comparison. Ice margins migrate <5° (550 km) on the precessional time scale.

as predicted by the LMDz-GRISLI climate model (*100*) when CO_2 is high (Fig. 10D). During the Marinoan cryochron in South Australia (Fig. 5A), a low-latitude periglacial block field was invaded by a sand sea, apparently under the influence of katabatic (paleo-north-northwesterly) winds (*258*). The block field and basal sandstone beds host deep (≤3 m) sand wedges, indicating subaerial exposure in a periglacial environment with strong seasonality (*230*–*232*). Ductile deformation of beds associated with sand wedges and the presence of surface meltwater channels indicate that the annual mean surface temperature should have been ≥268 K (*232*) at the known paleomagnetic latitude of 7° to 14° (*33*). The sand sea apparently formed toward the end of the Marinoan cryochron, whereas a coeval ice sheet

and associated katabatic winds are inferred to account for south-southeastward–directed dune migration (*258*), in the zone of easterly trade winds.

An analogous situation is inferred from totally different evidence in the Marinoan of East Svalbard (Fig. 5A). Periglacial lacustrine limestone (*100*–*102*), associated with dolostone and sandwiched between massive glacigenic diamictites (Fig. 7C), contains trace sulfate bearing the largest mass-independent oxygen isotope anomaly ($\Delta^{17}O \geq -1.6‰$) in the terrestrial record (*86*). The magnitude of the anomaly can be accounted for by high atmospheric CO_2 level combined with low rates of photosynthesis-respiration (*86*, *88*, *163*). Moreover, there is a strong mass-dependent isotopic enrichment of oxygen in the host carbonate, $\delta^{18}O \leq +15‰$ (*86*), most likely the result of evaporation. Sublimation of a permanently ice-covered lake should drive sub-ice water isotopically lighter, not heavier, because of ice-water equilibrium fractionation ($\delta^{18}O = 1.003$) (*259*) and quantitative sublimation of ice. Accordingly, either the Marinoan lake was not permanently ice-covered or the meltwater that fed it underwent strong evaporation as it flowed into the lake basin from adjacent glaciers. In contrast, modern hypersaline lake waters in the Antarctic McMurdo Dry Valleys (MDV) are isotopically light, close to the compositions of the bordering glaciers (*260*). This suggests that the opposed isotopic effects of evaporation and sublimation are nearly balanced in the MDV, whereas the late Marinoan cryochron in East Svalbard was more strongly evaporative.

Dry valleys, warmed by katabatic winds from adjacent ice sheets, were likely refugia for cold- and desiccation-tolerant microbial photo-trophs and heterotrophs on Snowball Earth (*261*, *262*). In 1971, cyanobacteria were found inhabiting rocky crevices at 2000 m elevation in the Transantarctic Mountains, <360 km from the South Pole (*263*). In the MDV, 1000 km to the north and 1.8 km lower in elevation, cyanobacteria inhabit rocky soils (*264*), lake ice (*265*), and ice-covered hypersaline lakes (*266*, *267*) in areas that rarely touch the melting point (*268*). Diatoms and ciliates constitute a small eukaryotic component of plankton in MDV brine lakes (*269*), and benthic diatom mats form stromatolites in MDV meltwater streams (*270*). Similar ecosystems are found in the High Arctic (*271*, *272*). However, diatoms do not appear in the fossil record until the Mesozoic era.

Any dust or volcanic ash that accumulates on a glacier will be advected to the ablation zone and may accumulate as "cryoconite" (dark ice-dust) on the surface of sublimative ice (Fig. 12). Clumps of cryoconite absorb solar radiation and sink to an equilibrium depth of ~0.5 m (*273*–*275*), forming "cryoconite holes" (Fig. 13B). Strongly pigmented organic matter produced extracellularly by indigenous cyanobacteria constitutes ~10 weight % (wt %) of typical cryoconite (*276*). This organic matter contributes to the dark color of cryoconite (*276*) and to its cohesion if desiccated (*277*). Although cryoconite holes on modern polar glaciers (Fig. 14A) contain meltwater only in summer (*278*, *279*), they support ecosystems that include not only cyanobacteria (*280*, *281*) but also eukaryotic green algae, fungi, ciliates, and certain metazoans, typically nematodes, rotifers, and tardigrades (*282*, *283*). We will return to the subject of cryoconite and its role in the dynamics and ecology of oceanic ice on Snowball Earth.

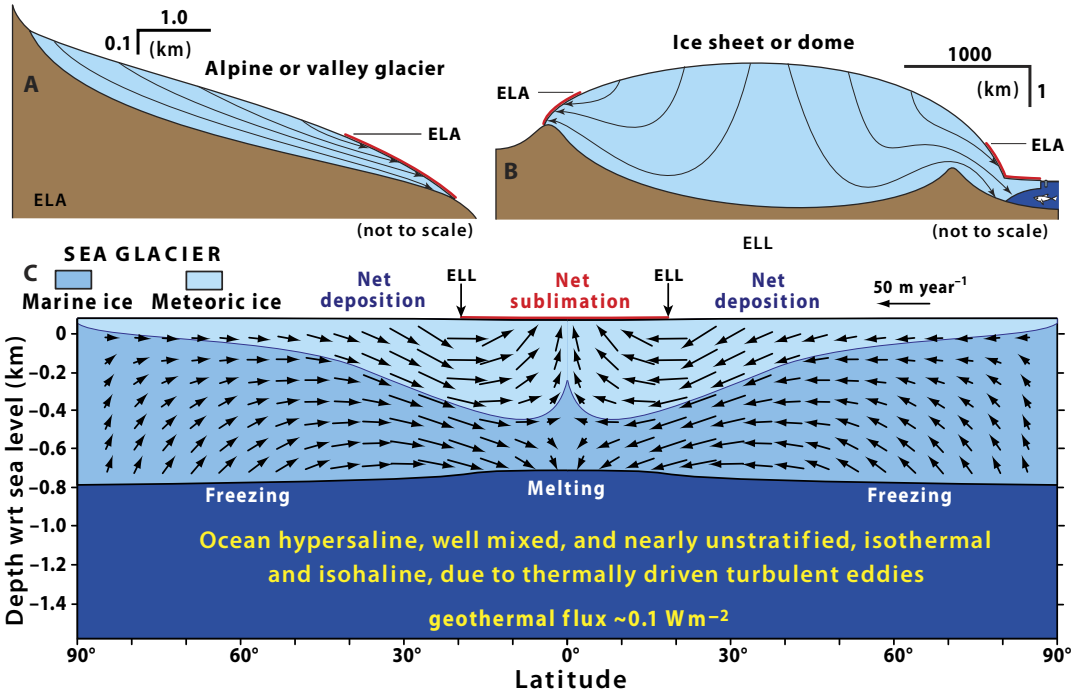

Fig. 12. Cryoconite distribution on glacial ice. (**A**) Alpine glacier and (**B**) ice sheet with terrestrial and marine ice margins. Arrows are ice flow lines. Ablation zones with transient cryoconite holes are indicated in red. ELA, equilibrium line altitude. (**C**) Sea glacier on a Snowball aquaplanet with sublimation zone (in red) where cryoconite collects. Steady-state dynamics in a 2D ice-flow model forced by the ocean-atmosphere GCM FOAM, run under relatively warm Snowball conditions (*167*, *216*). Sublimation of meteoric ice (compressed snow) and melting of marine ice (frozen seawater) at low latitudes are balanced by accumulation and freeze-on, respectively, outside the inner tropics. Flow velocities are highest (compare with Fig. 8D) in the outer tropics, and ice thickness at the equator is <80 m thinner than at the poles (compare with Fig. 16). Overall ice thickness is determined by the geothermal heat flux, global mean surface temperature, and thermal diffusivity of ice. Salinity and, therefore, freezing temperature of seawater depend on global ice volume. ELL, equilibrium line latitude. If volcanoes and continents were included, cryoconite would accumulate in the trans-equatorial sublimation zone (red line).

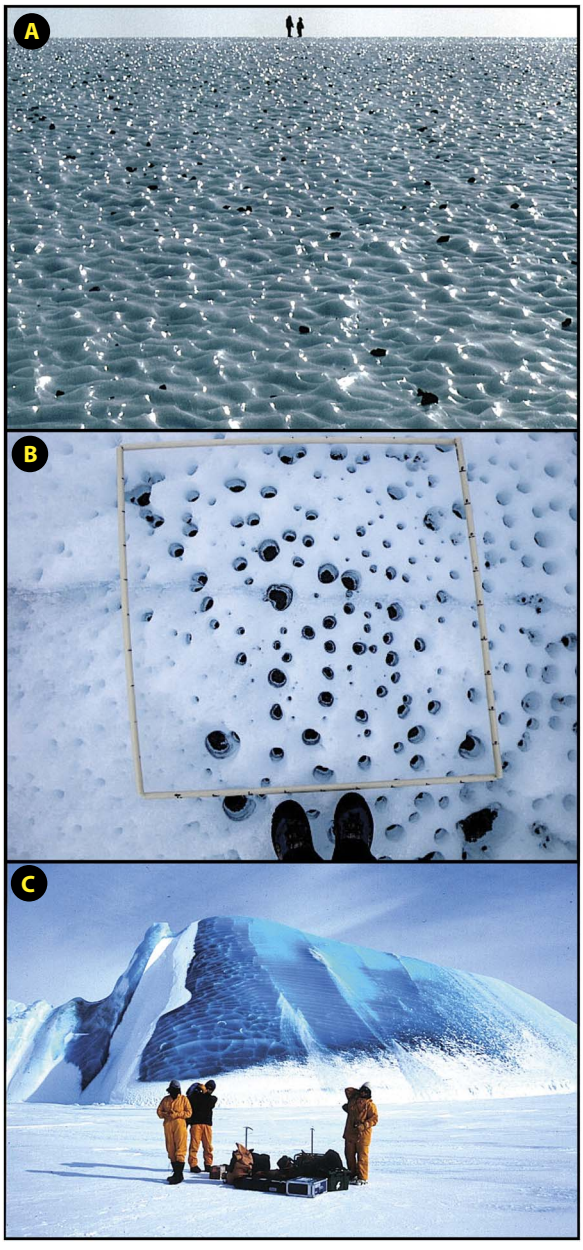

Fig. 13. Modern Antarctic analogs for Cryogenian sublimating ice surfaces. (**A**) Cold sublimating ice surface near Mount Howe nunatak in the Transantarctic Mountains, Antarctica, at 87°22′S latitude and 2350 m above sea level. Surface dust is removed by winds, leaving a lag of stones eroded from the nunatak. Broadband albedo, $\alpha = 0.63$ (*224*). (**B**) Warm sublimating ice surface with cryoconite holes on Canada Glacier, a piedmont glacier in the lower Taylor Valley, MDV area, Antarctica, at 77°37′S latitude and 145 m above sea level. Warmer surface temperatures due to katabatic winds allow dust (cryoconite) to accumulate on the surface, forming dark clumps suffused with organic matter that sink to an equilibrium depth, creating holes containing meltwater in summer capped by clear bubble-free ice (see Fig. 14A). Mucilaginous and heavily pigmented organic matter is secreted extracellularly by cold-tolerant cyanobacteria inhabiting the holes, which also support eukaryotic phototrophs and heterotrophs, including metazoans. (**C**) Capsized iceberg exposing marine ice, formed by freezing seawater at a depth exceeding ~400 m, where the ice does not incorporate bubbles because of increased solubility of air in water. Nor does the ice contain brine inclusions, and light is scattered mainly by a lattice of cracks. Consequently, spectral albedo is low, $\alpha = 0.27$ (*224*). This is the type of ice that may have been exposed in the sublimation zone of Cryogenian sea glaciers (Figs. 15D and 18B).

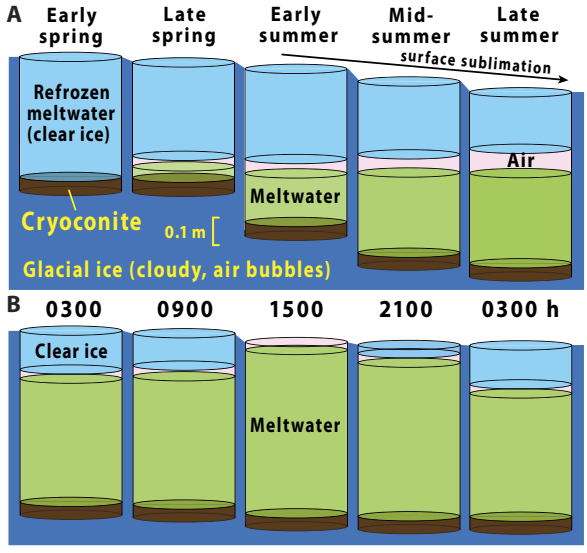

Fig. 14. Meltwater cycles in polar and low-latitude cryoconite holes. (**A**) Summer seasonal cycle of a cryoconite hole in the sublimation zone on Canada Glacier (Fig. 13B), Taylor Valley, Antarctica (*279*). In early summer, cryoconite melts to an equilibrium depth, after which it maintains constant depth relative to the sublimating surface. Air is evolved in the hole from melting of glacial ice containing bubbles of air and from photosynthetic O_2 production. Meltwater refreezes in winter and is covered by an ice cap in summer. Cryoconite is suffused with filamentous cyanobacteria and extracellular mucilaginous polysaccharides, and the holes are also inhabited by green algae, fungi, protists, and certain bilaterian animals—nematodes, rotifers, and tardigrades (*282*). (**B**) Postulated diurnal cycle (0000 hour) of a cryoconite hole on the low-latitude sublimation zone of a sea glacier on Snowball Earth. Relatively high CO_2 allows the nocturnal ice cap to melt away in midafternoon. Cryoconite holes and ponds provide supraglacial habitats for Cryogenian cyanobacteria and eukaryotic algae and heterotrophs once the surface becomes sufficiently warm to retain dust exposed by sublimation (*293*–*296*).

OCEANIC ICE AND THE EVOLUTION OF CRYOGENIAN MARINE LIFE

Snowball Earth is essentially an oceanographic phenomenon. Its onset is defined when the tropical ocean freezes over, and its termination is defined when the equatorial ice shelf finally divides and collapses. Small areas of open ocean are unsustainable because the sea ice becomes hundreds of meters thick within a few thousand years, due to the albedo-driven cold surface temperatures. Consequently, the ice spreads gravitationally and fills in any area that is not physically restricted (*116*, *167*, *168*, *216*, *224*). The term "sea glacier" (*216*, *224*) describes this floating ice mass (Figs. 8, C and D, and 12C), which flows toward the equatorial zone of net ablation from higher latitudes of net accumulation (Fig. 9, E and F). Likewise, it is difficult to maintain areas of oceanic ice sufficiently thin for sub-ice phototrophy, <20 m of clear ice, particularly in the coldest early part of a cryochron (*224*, *225*, *284*–*288*). The most favorable conditions for thin oceanic ice exist in hydrothermal areas (*289*) and marine embayments into low-albedo ice-free land areas (*290*–*292*).

Thin oceanic ice (or open water) is not a prerequisite for phototrophy if meltwater existed on the ice surface. Impressed by the existence of extensive supraglacial cryoconite ponds and associated microbial mats on the McMurdo (78°S) and Ward Hunt (83°N) ice shelves, Vincent and colleagues (*293*–*295*) postulated that similar ecosystems on Snowball Earth "would have provided refugia for the survival,

growth and evolution of a variety of organisms, including multicellular eukaryotes." The proposal was reinforced when modeling (*100*) indicated that ice-free land areas on Snowball Earth widen from the paleoequator as CO_2 rises (Fig. 10). Moreover, those source areas of terrigenous dust are situated in the same zone where surface winds associated with the Hadley cells are strongest (Fig. 9, A to D). The Snowball troposphere was dusty, and dust trapped anywhere on the sea glacier or on ice sheets feeding the sea glacier would be carried by glacial flow to the sublimative surface of meteoric ice in the equatorial zone (Fig. 12C). In Cryogenian paleogeography, the sea glacier sublimation zone is ~6×10^7 km^2 or about 12% of global surface area (*296*). Whereas cryoconite holes and ponds in the polar regions freeze solid in winter (Fig. 14A), those in the equatorial zone of Snowball Earth may have always contained meltwater (Fig. 14B), except during the earliest stages of a cryochron when sublimative surfaces may have been too cold for dust retention (Fig. 13A).

We begin the assessment of supraglacial refugia hypothesis by Vincent and co-workers (*293*–*295*) by briefly reviewing what is known from molecular and body fossil evidence about pre-Sturtian and pre-Marinoan marine life, with emphasis on purported crown groups, which, by definition, are lineages that survived the cryochron(s), and all subsequent vicissitudes. We then review attempts to find geologically acceptable climate-model states in which the tropical or equatorial ocean remains ice-free. Next, we sketch sea-glacier dynamics and its response to surface warming, based on 2D and 3D models. Finally, we consider the timing and extent of cryoconite accumulation and its potential climatic, geochemical, and evolutionary consequences.

Pre-Sturtian and Cryogenian fossil record

Cellular fossils and molecular phylogenetics indicate that cyanobacteria, including those with cellular differentiation, evolved more than 10^9 years before the Cryogenian (*297*–*300*). Low ratios of eukaryotic-to-bacterial biomarkers from indigenous bitumens and oils imply that bacteria were the dominant primary producers in pre-Sturtian oceans (*49*, *301*). As for eukaryotic primary producers, red algae and possibly green algae, including multicellular forms, are known from the pre-Sturtian cellular fossil record (*298*, *302*–*305*). Molecular (sterane) biomarkers suggest that green algae supplanted red algae as the dominant eukaryotic phototrophs sometime between the late Tonian and late Cryogenian (*48*, *49*, *301*). Among eukaryotic heterotrophs, vase-shaped microfossils (VSMs) resembling extant amoebozoans and rhizarians are widely preserved in pre-Sturtian strata around 740 Ma (*306*–*309*), and various protistan morphotypes including VSMs are found in nonglacial strata between the cryochrons (*310*–*313*). Molecular clocks predict that stem-group metazoans predated the Sturtian cryochron (*47*), and sterane biomarkers suggest that a metazoan crown group, demosponges, evolved before the Marinoan cryochron [(*46*–*48*); but see the study by Brocks and Butterfield (*314*)]. A Sturtian origin for crown-group metazoans is estimated by a molecular phylogenetic "clock" (*47*, *315*), although weak pre-Cambrian calibration compromises the accuracy of this estimate (*108*). The fossil record in total is too coarse to correlate extinctions or originations with cryochrons, but the Cryogenian stands out as an anomalous period of low total and within-assemblage eukaryotic diversity (*103*). After the Cryogenian ended, acritarch diversity increased sharply (*316*, *317*), as perhaps did that of benthic macroalgae (*106*, *107*, *318*). The fossil record and molecular phylogeny together indicate that multiple clades of eukaryotic algae and heterotrophs, both single-celled and multicellular, not only survived the Cryogenian glaciations but may have significantly evolved during that period (*319*–*321*).

Waterbelt solutions

There have been concerted efforts to find climate-model solutions that satisfy basic inferences from Cryogenian geology—dynamic ice sheets that reach sea level in the paleotropics (Fig. 5)—while maintaining a finite zone of open water in the warmest area. Some of these efforts were motivated by a perception that the "hard-snowball" hypothesis is implausible in light of the fossil record (*111*, *112*, *114*, *322*, *323*). "Waterbelt" (*116*) is a general term for these "loophole" (*322*) solutions, which have been less accurately called "slushball" or "soft-snowball" solutions in the literature. The modeling task is a difficult one. First, the solutions, by their nature, lie close to the Snowball bifurcation (Fig. 1), yet they must resist falling irrevocably into the Snowball state for millions to tens of millions of years (Fig. 2). This is a tall order, given stochastic, orbital, tectonic, and paleogeographic forcings (*116*). Second, a large hysteresis must exist between the Waterbelt and nonglacial states (*116*) to satisfy the geologically observed abrupt deglaciations and attendant geochemical anomalies—cap carbonates (*27*, *29*, *84*, *154*, *324*, *325*), proxy indicators of high CO_2 (*84*–*88*, *90*), and spikes in weathering (*60*, *89*, *326*). Third, as applied to the Sturtian cryochron, solutions must be compatible with deep-ocean ferruginous anoxia, given widespread synglacial nonvolcanic iron formations (Figs. 5B and 7E). This is a challenge because a narrow tropical ocean will experience intense wind-driven ventilation (*236*, *237*), and the remote ice-covered regions will lack organic productivity, reducing the demand for oxygen by aerobic respiration in those areas. However, the model solutions are interesting in their own right, independent of the needs of Cryogenian geology.

The most-cited Waterbelt solution, HCBP00 (*327*), emerged from a 2D energy-balance model coupled to a dynamic ice-sheet model, with a paleogeography in which a high-latitude supercontinent has promontories and large islands that extend across the deep tropics. Long integration times allow orbital forcing to be included. By incrementally lowering the CO_2 radiative forcing, a Snowball bifurcation is found at which ice sheets abruptly extend to all latitudes. The fully glaciated response from the coupled model was then prescribed in an atmospheric GCM (Genesis 2) with a mixed-layer ocean (that is, no ocean dynamics) and nondynamic sea ice. Over a limited range of CO_2 and continental freeboard, the tropical ice sheets coexist stably with sea-ice edges at ~25° latitude (*327*). The solution was criticized for lacking sea-ice dynamics (*328*, *329*). Sea-ice dynamics facilitate ice-line advance in the mid-latitudes where the Coriolis effect drives sea ice equatorward under the influence of westerly winds. The concern was left unresolved because the wind field in the dynamic sea-ice model (*329*) was imported from a GCM (FOAM) response to Cryogenian paleogeography in the absence of ice. A low-latitude ice margin would produce a much stronger wind field (*236*, *237*), in which Coriolis forcing under the influence of the trade winds might actually retard sea-ice advance.

Another concern with the HCBP00 solution is that the mid- to high-latitude sea-ice caps are arbitrarily limited to 10 m of maximum thickness, and therefore, gravitational flow (*116*, *167*, *168*, *216*) is excluded. Moreover, an artificial heat source was introduced to limit ice thickness (*327*), and this heat source arbitrarily retards ice-cap growth. Additional simulations showed that the sea-ice margins in the HCBP00 solution retreat poleward in response to even modest increases in CO_2 (*330*), simulating the loss of weathering by the ice-covered continents. The hysteresis demanded by the records of Cryogenian deglaciation is not present. It was subsequently found that low-latitude ice sheets do not develop when the tropical ocean is ice-free in a coupled ocean-atmosphere GCM (ECHAM5/MPI-OM), even when mountain topography is prescribed (*166*).

A different class of Waterbelt solutions, called "Jormungand" (*236*), was revealed by simulations with atmospheric GCMs (CAM and ECHAM5) and coupled atmosphere-ocean GCMs, with (CCSM3 and CCSM4) and without (ECHAM5/MPI-OM) sea-ice dynamics. It was found that by prescribing a large difference in broadband albedo between ablative (0.55) and snow-covered (0.79) ice, sea-ice margins are stable at 5° to 15° latitude (*236*). As the floating ice margins enter the tropics in response to weakened radiative forcing, the ablation zones widen as they encroach upon the subsiding limbs of the intensified Hadley cells. This lowers the zonal and planetary albedos, stabilizing the ice margins. The narrow seaway migrates nearly its own width back and forth across the equator with the seasons. Ice sheets develop on elevated continents in the equatorial zone where, unlike Snowball Earth, there is a large excess of precipitation over evaporation (*166*, *236*). Strong hysteresis between Jormungand and nonglacial states has been found in aquaplanet atmosphere-only GCMs, although less so than for the Snowball state (*236*), but more work is needed to clarify the impact of ocean dynamics and continents on Jormungand hysteresis. The low-latitude sea-ice margins destabilize to Snowball states when sea-ice dynamics are switched on in ECHAM5-MPI-OM (*20*) but not in CCSM3 and CCSM4, which include sea-ice dynamics (*19*, *332*). Orbital forcing and sea-glacier flow have yet to be investigated in the Jormungand state.

A third Waterbelt solution, BR15 (*237*), was uncovered using a coupled atmosphere-ocean-sea ice GCM (MITgcm) with simplified paleogeographies. As CO_2 is incrementally lowered, the sea-ice margins stabilize at 21° to 30° because of wind-driven ocean heat transport, which intensifies as the margins converge (consistent with Jormungand), creating a negative feedback (*237*). As with Jormungand, equatorial ice sheets are compatible with the BR15 solution (*166*). A potential destabilizing process involves boundary-layer temperature inversions in the winter hemisphere, where the surface becomes very cold through radiation (*81*, *226*–*228*, *331*). Inversions decouple the ocean from winds, disabling the wind-driven negative feedback. Atmospheric GCMs with high vertical resolution and realistic paleogeography are needed to resolve this issue.

Sea-glacier development on the Snowball ocean

A Snowball Earth ensues when sea ice, having reached a critical latitude, advances uncontrollably to the equator through ice-albedo feedback (Fig. 1). The time scale of the final sea-ice advance is geologically instantaneous, ~150 years in a 3D ocean GCM coupled to a thermodynamic/dynamic sea-ice model and an energy-moisture balance atmosphere model [(*329*); see also the studies by Yang and co-workers (*19*, *332*)]. The first-formed sea ice on the low-latitude ocean would resemble rapidly growing sea ice in the polar winters of today and have ~4‰ salinity after several months of growth. If surface temperatures fall below ~250 K, then hydrohalite ($NaCl{\cdot}2H_2O$) begins to crystallize in brine inclusions within the ice. If temperatures are below ~250 K in daytime, then the resultant increase in bare-ice albedo causes additional cooling (*286*). Where the cold ice is ablating by sublimation, the hydrohalite crystals accumulate as a surface lag, with an albedo higher than fresh snow (*284*, *287*, *288*). However, when produced in the laboratory, the hydrohalite lag is a loose powder that would be susceptible to dispersal by winds (*284*).

After a few millennia, the oceanic ice cover outside the tropics is expected to reach thicknesses of several hundred meters, built up from above by frost deposition and snowfall and from below by freezing of seawater. This ice should be sufficiently thick to flow as "sea glaciers" (*216*, *224*), analogous to unconfined ice shelves but not dependent on continental sources of ice (*116*, *167*, *168*, *216*, *291*). The sea glaciers would flow into the tropics and displace the thinner sea ice. They are composed of two ice types (Fig. 12C), "meteoric ice" (compressed snow) and "marine ice" (frozen seawater). Without continents, dynamic steady state requires that sublimation and accumulation of meteoric ice are in balance, as are melting and freezing of marine ice (Fig. 15B). Sublimation of marine ice cannot occur in steady state in the absence of a return flux to the ocean (Fig. 15A) (*333*). If continents are present, then the situation is reversed. Sublimation of marine ice must occur (Fig. 15D) to balance the subglacial meltwater flux into the ocean from continental ice sheets (Fig. 15C). Sublimation of marine ice is observed in some models (*81*, *168*, *239*), and geological evidence supports meltwater discharge at tidewater grounding lines of Cryogenian ice sheets (*96*, *334*). Surface exposure of marine ice strongly influences climate and sea-glacier dynamics because of its low albedo (*224*).

The high albedo of bare meteoric ice is the result of light scattering by air bubbles and cracks (*225*), and that of bare sea ice is caused by brine inclusions, air bubbles, and cracks (*335*). Marine ice formed at water depths of >400 m (Fig. 13C) lacks air bubbles and brine inclusions (*224*). Consequently, it has a low bare-ice albedo (0.27), much lower than either meteoric or sea ice (*224*). Both bubbles and brine inclusions migrate downward, toward the warm end of a temperature gradient. However, laboratory experiments show that, for the expected rates of sublimation on Snowball Earth (Fig. 9, E and F), the downward migration does not outrun the sublimation front (*284*, *285*); thus, the albedos of meteoric and sea ice can remain high as sublimation proceeds.

Steady-state sea-glacier ice thicknesses and meridional velocities in different GCM-ice model couplings with 0.1 and 100 mbar of CO_2 are shown in Fig. 8 (C and D). The prescribed conditions were described earlier in the "Atmosphere Dynamics and the Hydrologic Cycle" section. Continents are neglected, and the ice albedo is set to 0.6 everywhere (*81*). The treatment was extended to spherical geometry and two horizontal dimensions, with a Cryogenian paleogeography (Fig. 16), still with uniform surface albedo (*291*). The models all indicate thick ice at the equator with modest thickening toward the poles (Figs. 8C and 12C) and maximum flow velocities near the equilibrium line latitude (Figs. 8D, 12C, and 16, A and B). With temperature-dependent ice viscosity, low-latitude ice thicknesses actually increase slightly as the surface warms (*291*). The thinnest ice is found in low-latitude embayments (Fig. 16), particularly those that are long and narrow, have large bay-head basins or inland seas, and receive cold ice (*290*–*292*). With uniform surface albedo, embayment ice remains too thick to allow sub-ice photosynthesis (Fig. 16, A and B), but this may not be true if the ice was significantly more transparent (*224*), if ablation rates were enhanced because the embayment was bordered by dark bare land (*100*), or if the embayment had a higher-than-average geothermal flux, as expected in young, actively spreading, oceanic rift basins (Fig. 5). Low-latitude embayments may have been critical for phototrophs in early stages of cryochrons, when sea ice elsewhere was too thick for sub-ice photosynthesis and too cold for dust retention (Fig. 13A).

Grounding-line crack systems

Sea-glacier flow appears to foreclose the possibility of widespread photosynthesis beneath tropical sea ice, but it suggests another setting where liquid water and sunlight might intercept. Shear cracks would perpetually develop where a fast-flowing sea glacier is in contact with landfast ice (Fig. 17). Where inland ice sheets drained into the ocean through outlet ice streams, they might simply merge with the sea glacier without deep cracks. But where the inland ice was frozen to the bed, away from

ice streams, shear stress would be relieved by deep crack systems in which water pressure would hold opposing ice cliffs apart. A modern analog occurs on the north side of the Pine Island Ice Shelf (West Antarctica) near the calving front (Fig. 17A). The ice shelf is ~0.5 km thick at this point (*336*), and a dextral shear couple exists between landfast ice and fast-flowing (~2.8 km year^{-1}) shelf ice. The cracks are more open close to the calving front (Fig. 17A), which presumably would not exist on a Snowball Earth until the terminal deglaciation.

The seawater that filled a newly formed crack would encounter the cold atmosphere and freeze at the surface, forming new sea ice with inclusions of seawater that would salinate by progressive freezing as the sea ice thickened and chilled. Brine inclusions in modern sea ice provide habitats for prokaryotic and eukaryotic phototrophs (mainly diatoms), as well as heterotrophic protistans and metazoans (*337*). The organisms must be tolerant not only of hypersalinity but also of hyperoxia, because photosynthetically produced O_2 cannot diffuse out of a closed brine inclusion. The thickness of sea-glacier ice (Figs. 8C and 16, A and B) is such that sea ice in cracks would reside in 0.1-km-deep "canyons" and receive direct sunlight for only a short period of the day (Fig. 17B), if at all, unless they were fortuitously oriented in the ecliptic plane.

Dust sources and accumulation rates

There were three sources of dust on Snowball Earth, volcanic, detrital, and cosmic (*78*). The modern production rate of volcanic tephra (ash and coarser-grained ejecta) amounts to an accumulation rate, if spread evenly over the globe, of roughly 10^{-6} m year^{-1} (*78*, *338*). The terrestrial volcanic flux would be somewhat reduced on Snowball Earth due to loading by ice sheets (*339*), but this effect would wane over time as ice sheets contracted with CO_2 rise (Fig. 10). The modern global average accumulation rate of detrital dust is roughly 5×10^{-7} m year^{-1} and was 2 to 20 times higher (10^{-6} to 10^{-5} m year^{-1}) at the Last Glacial Maximum (LGM), mainly due to decreased vegetation (*78*, *340*). The LGM dust flux is a reasonable minimum estimate for Snowball Earth (*77*–*81*), given extensive ice-free land area (*24*, *92*, *100*, *230*, *232*, *258*, *341*, *342*), arid and poorly vegetated soils produced by intense cryogenic weathering associated with large diurnal and seasonal temperature fluctuations (*77*, *343*), production of loess through the grinding action of glaciers charged with rock debris (*344*), and strong summer and katabatic winds (*81*, *226*–*228*, *258*, *342*). In comparison, the modern global average accumulation rate of cosmic dust, 1.5×10^{-10} m year^{-1}, is negligible (*78*). There is no reason to suspect that the Cryogenian cosmic dust flux was significantly higher than modern values (*345*). Taking the LGM flux of detrital dust alone amounts to a global average accumulation rate of 1 to 10 m My^{-1}. Considering the duration of a Snowball Earth, where did so much dust actually accumulate?

Cryoconite holes and ponds

Dust that is trapped in the accumulation zones of ice sheets and the sea glacier will be buried by new snow and entrained in meteoric ice (Fig. 12). Roughly half the ice that accumulates in ice sheets drains into the sea glacier, whereas the rest deposits its dust load in peripheral moraines (Fig. 10). The total ice-sheet area shrinks from 0.8 to 0.2 of continental (including shelf) area over a cryochron (*100*) or from 0.32 to 0.08 of global surface area. Assuming that the sea glacier occupies 0.6 of

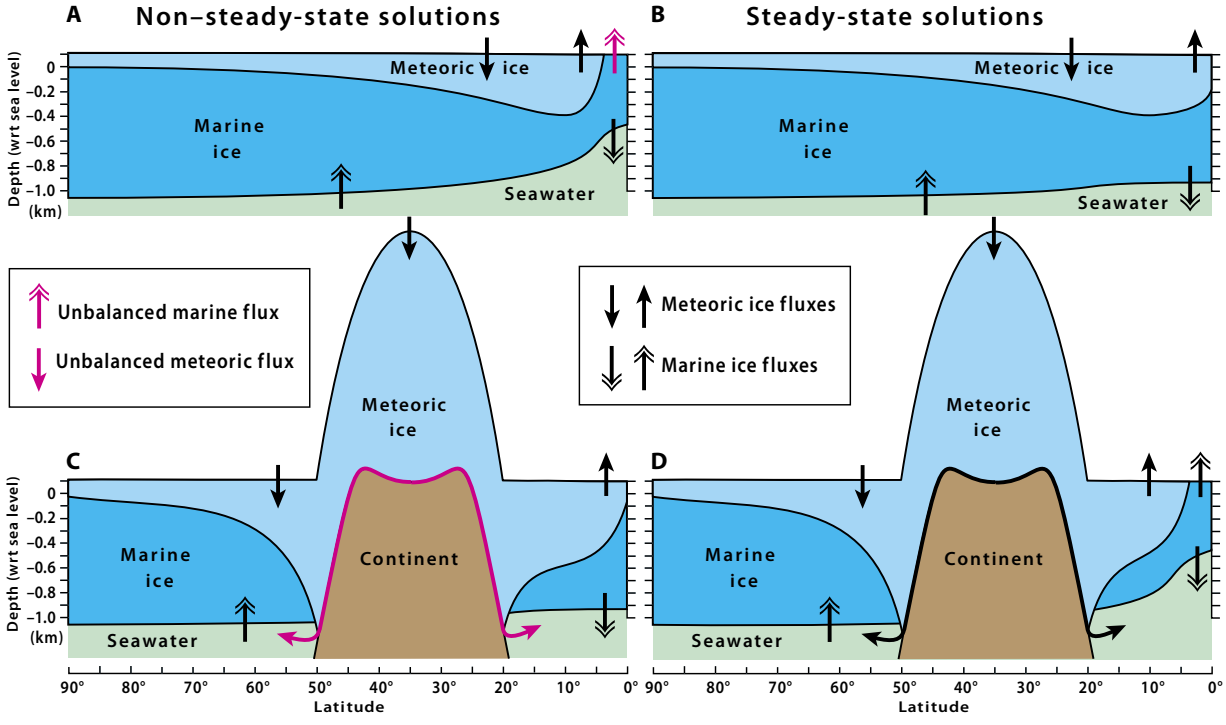

Fig. 15. Non–steady-state and steady-state hydrologic cycling on Snowball Earth, with and without continents. (**A**) Non–steady-state Snowball aquaplanet on which low-albedo marine ice (*496*) outcrops in the sublimation zone. Sublimation of marine ice (magenta arrow) is not balanced by a return flux to the seawater–marine ice subsystem (*333*). (**B**) Steady-state Snowball aquaplanet on which only meteoric ice is exposed. (**C**) Non–steady-state Snowball Earth with continents. Meteoric ice-sheet meltwater enters the ocean at ice grounding lines (magenta arrows) but is not balanced by a return flux to the atmosphere–meteoric ice subsystem, because only meteoric ice is exposed. (**D**) Steady-state Snowball Earth with continents. Ice-sheet meltwater injected into the ocean is balanced by sublimation of outcropping marine ice. Cryoconite meltwater flushing (Fig. 18B) functions essentially like a grounded ice sheet, fluxing meteoric water into the subglacial ocean.

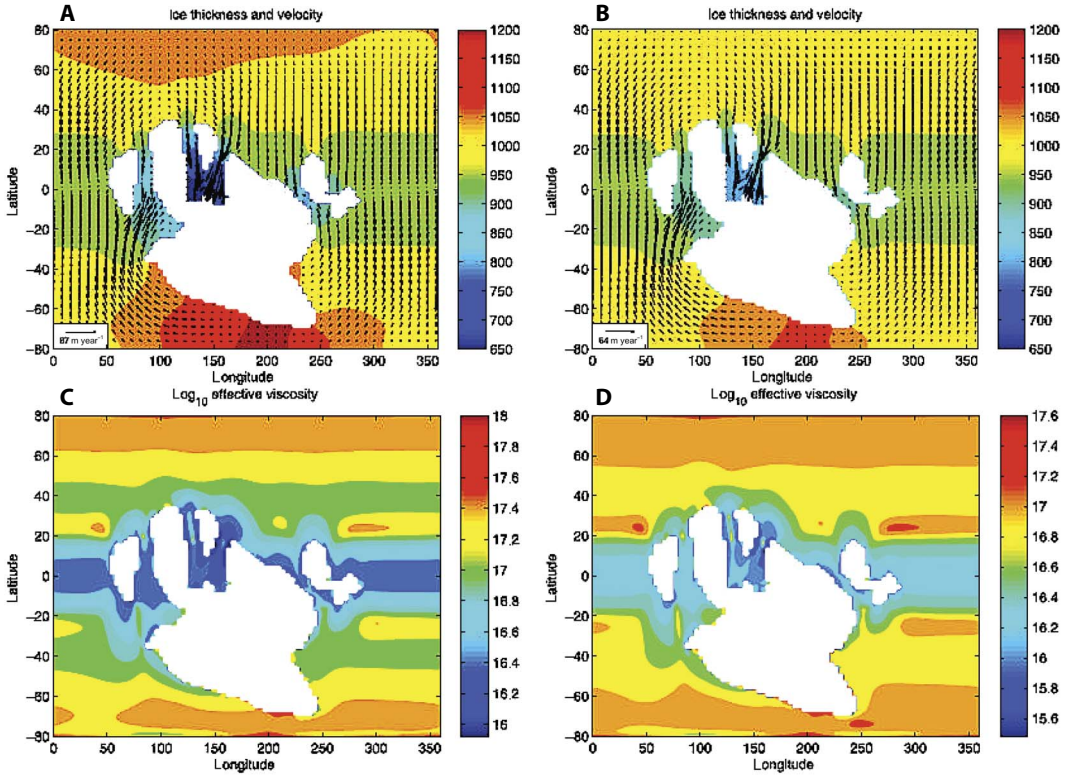

Fig. 16. 2D sea-glacier flow model in a Cryogenian paleogeography. Steady-state ice thickness (scale bar in meters) and velocity field (arrows, in meters per year, with every fourth velocity vector shown) with surface temperatures smoothly fitted to NCAR GCM results assuming a surface albedo of 0.6 and CO_2 = 0.1 mbar (**A**) and 100 mbar (**B**) (*291*). Paleogeography from the study by Li *et al.* (*179*). Tropical ice thickness changes as CO_2 rises are minimal, because surface warming softens the ice, reducing the meridional thickness gradient. (**C** and **D**) Log_{10} of the effective viscosity (*291*) with the same albedo and CO_2 forcings as (A) and (B), respectively. The thinnest, softest, and fastest-flowing ice occurs in meridional sounds and gulfs.

global surface area, the total area of accumulation that will be advected to the sublimation zone of the sea glacier will be 0.76 to 0.64 of global surface area. Because the sea-glacier sublimation area is 0.12 of global surface area in Cryogenian paleogeography, the dust accumulation rate in the sublimation zone, assuming zero recycling by winds (or meltwater flushing, as discussed in the next section), will be 6.3 to 5.3 times the global average dust flux. Taking the conservative LGM dust flux of 1 to 10 m My^{-1} leads to average accumulation rates in the sea-glacier sublimation zone of roughly 6 to 60 m My^{-1}. The total thickness of dust that would have accumulated over the 58-My Sturtian cryochron is 0.35 to 3.5 km. It seems improbable that the equatorial sea glacier could mechanically support a supraglacial moraine of this thickness. Hence, let us examine the scenario more closely.

At the onset of a Snowball Earth, when sublimative surfaces are extremely cold, dust will not stick but will be lofted by winds and filtered out of the air by the firn (uncompacted snow) in accumulation zones (*346*). Modern examples exist in the "blue ice" areas of the Transantarctic Mountains (Fig. 13A), where both dust and rock fragments (including meteorites) are advected to the sublimation surface, but only stones too large for aeolian transport accumulate. Cryoconite and cryoconite holes are absent on such a cold surface. In the early phase of a Snowball cryochron, cryoconite holes may only develop in equatorial marine embayments, where sublimative ice is flanked by low-albedo ice-free land (*290*–*292*). Elsewhere, dust will be continuously recycled, poleward by wind and equatorward by ice, while accumulating within the sea glacier, rather than on its sublimative surface.

As atmospheric CO_2 rises and the subsurface ice becomes dustier, the ablative surface warms and dust begins to stick. The ice albedo drops rapidly. As surface dust accumulates, it clumps and absorbs sunlight, creating meltwater films in which cyanobacteria grow. They secrete heavily pigmented extracellular polysaccharide that darkens the dust, increases its wind resistance, and contributes to mass wasting of the ice (*276*, *277*, *347*). Clumps of dark dust sink to an equilibrium depth of 0.4 to 0.6 m in the ice, forming cryoconite holes (Fig. 13B). Whereas polar cryoconite holes contain liquid water only in summer and may be permanently ice-capped (Fig. 14A), cryoconite holes on the equatorial sea glacier may contain liquid water throughout the year. They will be insulated at night by caps of ice and exposed to the atmosphere when afternoon temperature at equinox reaches the melting point (Fig. 14B). The absence of winter freeze-up makes cryoconite holes on an equatorial sea glacier a less stringent habitat than those on modern polar ice shelves and glaciers. The limitation to growth is the availability of mineral nutrients from the dust. Dominance of cyanobacteria is a hallmark of oligotrophy in cold environments (*348*).

If the rate of dust accumulation on the sublimation surface of the sea glacier is anywhere near 6 to 60 m My^{-1}, then cryoconite will rapidly (on a Snowball time scale) saturate the surface (*77*, *78*, *167*, *168*). Cryoconite holes will coalesce to form meter-deep cryoconite ponds (*261*, *293*–*295*). The sublimation zone area in Cryogenian paleogeography is roughly 6×10^7 km^2 or 0.12 of global surface area (Fig. 18A). Solar energy absorbed by a semicontinuous layer of cryoconite has a marked effect on ablation-zone ice thickness (Fig. 18B), particularly near the

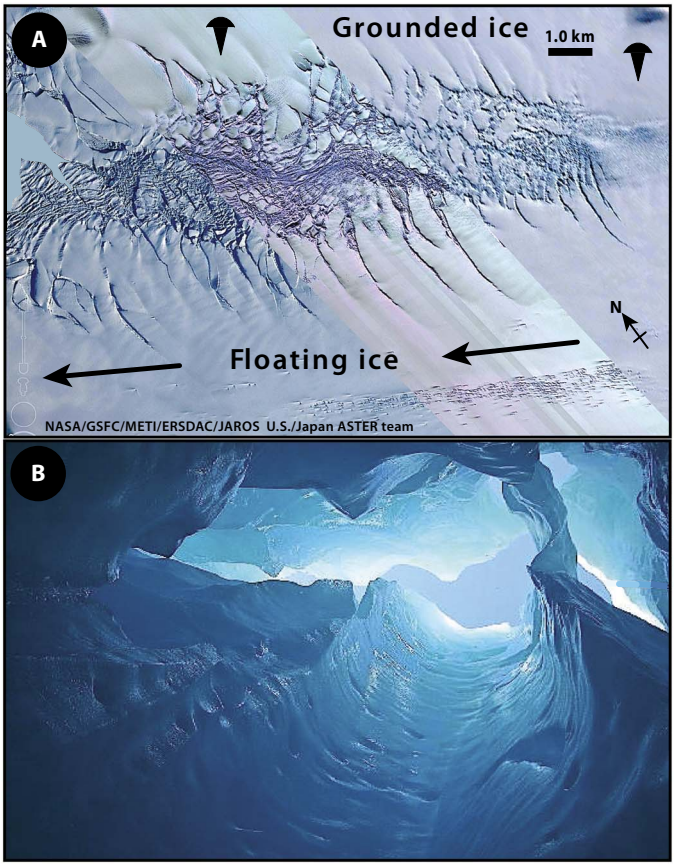

Fig. 17. Shear cracks on ice shelves. (**A**) Dextral shear produces a crack system where fast-flowing (~2.8 km year^{-1}) 0.5-km-thick shelf ice abuts grounded ice on the north side of the Pine Island Ice Shelf, West Antarctica. Crack system is best developed within 20 km of the calving front. Arrows indicate ice-shelf flow direction, and tacks indicate landfast ice. Satellite imagery courtesy of NASA/GSFC/METI/ERSDAC/JAROS U.S./Japan ASTER team. (**B**) Thickness of a sea glacier on Snowball Earth (Figs. 8C and 16) implies that cracks were deeply recessed, weakly illuminated, and more important as conduits for air-sea gas exchange than for phototrophy.

snowline latitude where the dusty surface is first exposed (*168*). In a 1D (meridional) ice-atmosphere-dust climate model, operating within the framework of a 1D energy-balance model, sublimation zone ice thicknesses are about 0.2 and 0.1 km for dust fluxes of 10^{-6} and 10^{-5} m year^{-1}, respectively (*168*). For comparison, the equivalent ice thickness in the same model in the absence of cryoconite is 0.74 km (*168*). In the cryoconite-rich zone, the temperature difference between the top and bottom of the sea glacier is nearly zero; thus, the equilibrium ice thickness in the absence of flow would be zero. The modeled ice thicknesses of 0.1 to 0.2 km are maintained by the inflow of cold ice (*168*). The inflows are characterized by quasi-periodic, reciprocating, semicentennial, ice surges (*168*).

Meltwater flushing and the cryoconite thermostat

How could a Cryogenian Snowball Earth persist for 5×10^7 years encircled by an equatorial cryoconite moraine hundreds to thousands of meters thick? Such a moraine would significantly lower the planetary albedo, but it would also shield the underlying ice from penetrative radiation. One possibility is that overthickened areas of the moraine would become gravitationally unstable, leading to localized ice collapses and dumping of morainal sediment into the subglacial ocean. The collapsed areas would quickly "heal" by glacial inflow, resulting in a thinner moraine. Because the morainal load is spread out, collapses should not occur until the sea glacier has become quite thin.

An alternative stabilizing feedback that does not require a thick moraine involves meltwater flushing through enlarged cracks, called moulins, and consequent cryoconite cleansing (*168*). As cryoconite accumulates, the rate of meltwater production rises. Drainage systems develop, linking the cryoconite ponds to flushing conduits, or moulins—subvertical shafts that originate as cracks and are maintained by the latent heat of falling meltwater and the hydrostatic pressure of seawater acting over 90% of their depth. The drainage systems cleanse the ice surface of cryoconite and flush it into the subglacial ocean (Fig. 18B). This raises the ice albedo and reduces the meltwater production rate. If the dust flux wanes, then meltwater production slows and cryoconite accumulates. If the dust flux waxes, then meltwater production quickens and cryoconite is removed. The resulting "cryoconite thermostat" (*168*) maintains a relatively warm and thin equatorial sea glacier (compare Figs. 12C and 18B) but is incapable of triggering terminal deglaciation at low CO_2. A critical CO_2 threshold is still required, although it will be substantially less than if cryoconite was absent. In the sea-glacier model with cryoconite (Fig. 18B), marine ice is exposed in the sublimation zone (unlike Fig. 12C), as required by a steady-state hydrologic cycle (Fig. 15D).

Meltwater flushing, the carbon cycle, and atmospheric oxygen

The organic contents of modern cryoconite on Himalayan, Tibetan, and Arctic glaciers range from 3 to 13 wt %, with the highest average contents (11 wt %) in the Arctic (*276*). Within cryoconite holes and ponds, organic production is nearly balanced by aerobic respiration over the seasonal cycle (*278*, *349*). But what happens to the organic content of cryoconite that is flushed into the subglacial ocean (Fig. 18B)? That ocean is generally assumed to have contained little dissolved oxygen (*24*, *74*, *350*), consistent with the wide distribution of Sturtian synglacial iron formation (Figs. 4B and 5B). Pre-Sturtian deep water was largely ferruginous, with intermittent to persistent euxinia in highly productive coastal areas (*351*–*354*). In the Snowball ocean, O_2 influx at cracks and moulins would have been offset by consumption of O_2 by seafloor weathering and submarine volcanic outgassing (*74*). In the absence of O_2, respiration depends on sulfate and Fe (III) as terminal electron acceptors. The subglacial ocean had two sources of sulfate and Fe(III). The injection of meltwater generated beneath ice sheets (Fig. 15D) delivered dissolved sulfate and suspended Fe (III) as products of oxidative subglacial weathering (*171*). Cryoconite flushing delivered sulfate derived from volcanic aerosols and Fe(III) from detrital dust. If the fluxes of sulfate and Fe(III) were inadequate to respire all the flushed cryoconite organic matter, in the water column or in the sediment, then organic burial would have created a source of atmospheric O_2 (Fig. 18B). A source of O_2 was needed to meet the consumptive demands of subaerial volcanic outgassing and rock weathering, because the absence of mass-independent S isotope fractionation ($\delta^{33}S \geq 0.3‰$) in Cryogenian sediments (*355*) implies that the Snowball atmosphere did not become anoxic.

It has been hypothesized that Snowball glaciations of Siderian (2.5 to 2.3 Ga) and Cryogenian age (Fig. 2B) were responsible for irreversible increases in atmospheric O_2 (*356*). Cryoconite flushing and resultant organic burial are processes by which this might have been achieved (*296*). Although there is some proxy support for stepwise increases in atmospheric O_2 coincident with Cryogenian glaciations [(*357*–*360*); but see the study by Blamey *et al.* (*361*)], the existing record of atmospheric oxygenation between 0.8 and 0.4 Ga overall remains inadequate to

confidently defend or refute the hypothesis (*356*) that Cryogenian glaciation drove atmospheric O_2 irreversibly from a Proterozoic to a Phanerozoic steady state.

Cryoconite flushing and volcanic ash deposition

Discrete layers of volcanic ash (Fig. 19A) are occasionally found within stratified glaciomarine deposits of Cryogenian age (*32*, *56*, *58*, *59*, *83*, *362*–*364*). Where intrabasinal volcanism is absent, the ash layers are assumed to be far-traveled and subaerially erupted. It has been argued that the deposition of these layers indicates ice-free conditions (*83*). But what if the ash was deposited first on ice and then glacially advected to the low-latitude sublimation surface of the sea glacier (Fig. 12C), where it resided until flushed through a moulin into the subglacial ocean (Fig. 18B)? Glacial flow is nearly linear, so a patch or streamer of volcanic ash would maintain its integrity in transport, becoming more concentrated after it reaches the edge of the sublimation zone (*168*). The ash-rich cryoconite would be susceptible to dispersal by ocean currents once it is flushed, but this is also the case for ash deposited on an ice-free ocean. The Snowball ocean is turbulent (see the "Subglacial ocean dynamics" section) but less turbulent than the mixed layer of an ice-free ocean. The deposition of discrete layers of far-traveled volcanic ash may, in fact, be more likely in an ice-covered ocean than in one that is ice-free.

This could be good and bad for geology. It implies that roughly two-thirds (see above) of all the volcanic ash that erupted subaerially on a Snowball Earth would enter the marine sediment record at low latitude. This would narrow the search for dateable ash layers but leave many areas barren. Low-latitude bias is a testable prediction of airborne ash deposition through a sea glacier. Most of the known synglacial ash layers—in the Sturtian of Oman (*362*, *365*), western Laurentia (*32*, *363*, *364*) and South Australia (*366*), and the Marinoan of Namibia (*56*, *83*) and Tasmania (*59*)—were inferentially deposited at low latitudes (Fig. 5). The Marinoan Nantuo Formation of South China, an ash-bearing synglacial sequence (*58*) with a paleomagnetic latitude of ~33°N (*367*, *368*), requires a different explanation (Fig. 5).

It is generally assumed that U-Pb ages of primary igneous zircons from volcanic ash layers date the time when the layer was deposited. Passage through ice implies a time lag between eruption (zircon crystallization) and final deposition. The magnitude of the lag depends on the distance traveled, the average speed of the ice, and the residence time of the ash on the sublimation surface. For most eruption locations, the transit time in ice will be <0.3 My, at any CO_2 level (Fig. 15, A and B). By taking 1.0 m as an upper bound on the average sustainable cryoconite thickness over the entire sublimation zone, an LGM dust flux of 10^{-5} to 10^{-6} m year^{-1} globally for a Snowball Earth (*77*, *78*) gives a residence time on the sublimation surface of 18 to 180 ky assuming no input from continental ice sheets. Even with large local departures from these estimates, the time lag between eruption and sedimentation will generally be within the analytical uncertainty of U-Pb dating.

Cryoconite ponds as habitats for Cryogenian eukaryotes

Cryoconite ponds are colder, fresher, shallower, and more oxygenated than the ambient pre-Sturtian ocean (*351*–*354*). Slow-growing algae adapted for low-light conditions (for example, red algae) are competitively disadvantaged, whereas those adapted for fresh water and high oxidative stress (for example, chlorophyte green algae) are advantaged (*273*, *282*, *293*, *294*). Sterane biomarker data suggest that green algae supplanted red algae as the dominant marine eukaryotic primary producers sometime between the late Tonian and the Cryogenian nonglacial interlude (*46*, *49*, *301*).

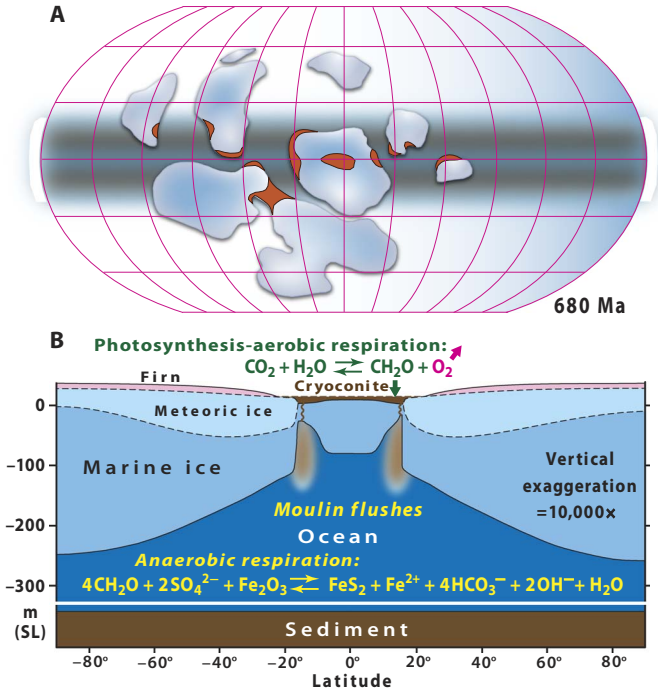

Fig. 18. Cryoconite ponds and cryoconite meltwater flushing on Snowball Earth (*297*). (**A**) Global paleogeography during the Sturtian cryochron at 680 Ma (*34*). Brown continental areas schematically indicate dry-valley dust sources (*100*). Gray areas in the low-latitude sublimation zone of the sea glacier are schematic cryoconite ponds. (**B**) Snapshot of a 2D ice-flow model of a Snowball Earth with a global dust accumulation rate of 10 m My^{-1} (*168*). Dark cryoconite and exposed marine ice make sublimative ice warm and thin. Hemispheric asymmetry at low latitude reflects unsteady, quasi-periodic, reciprocal ice surges from the respective subtropics in the model. Flushing of meltwater and cryoconite through moulins is shown schematically. The apparent ice walls at 18° latitude have actual slopes of 1 m km^{-1}. Organic production is nearly balanced by aerobic respiration within cryoconite holes and ponds. Flushed cryoconite organic matter is subject to anaerobic respiration in the water and sediment columns. Fe(III) and sulfate are sourced from the flushed cryoconite and sub–ice-sheet weathering. If anaerobic respiration is incomplete, organic matter is buried and O_2 is added to the atmosphere. SL, sea level.

Although cryoconite ponds may have offered oases for algae, fungi, and protistans during at least the warmer phases of the cryochrons, their suitability as a habitat for early metazoans is less certain (*296*). Lacking a regulatory mechanism for intracellular salinity, early sponges and cnidarians may have been stenohaline—osmotically intolerant of salinities outside the normal range of seawater. Experiments demonstrate that pumping by the modern estuarine sponge *Microciona prolifera* (Ellis & Solander) slows markedly below 15 and above 40 parts per trillion (ppt) of chloride, and the organism does not survive prolonged exposure to waters below 10 or above 45 ppt (*369*, *370*). Modern freshwater sponges belong to a single family (Spongillidae), representing a derived trait unlikely to be primitive (*371*, *372*). Those metazoans that do inhabit modern cryoconite holes (nematodes, rotifers, and tardigrades) are bilaterians (*283*), whose crown groups probably did not emerge until after the Cryogenian glaciations (Fig. 3) (*373*). In contrast, estimated crown group first appearance ages for demosponges and cnidarians fall within the Sturtian cryochron (*47*, *108*), consistent with sterane biomarker data (*48*).

If not in cryoconite ponds, where did early sponges and cnidarians live on Snowball Earth? As benthic filter feeders, living beneath or

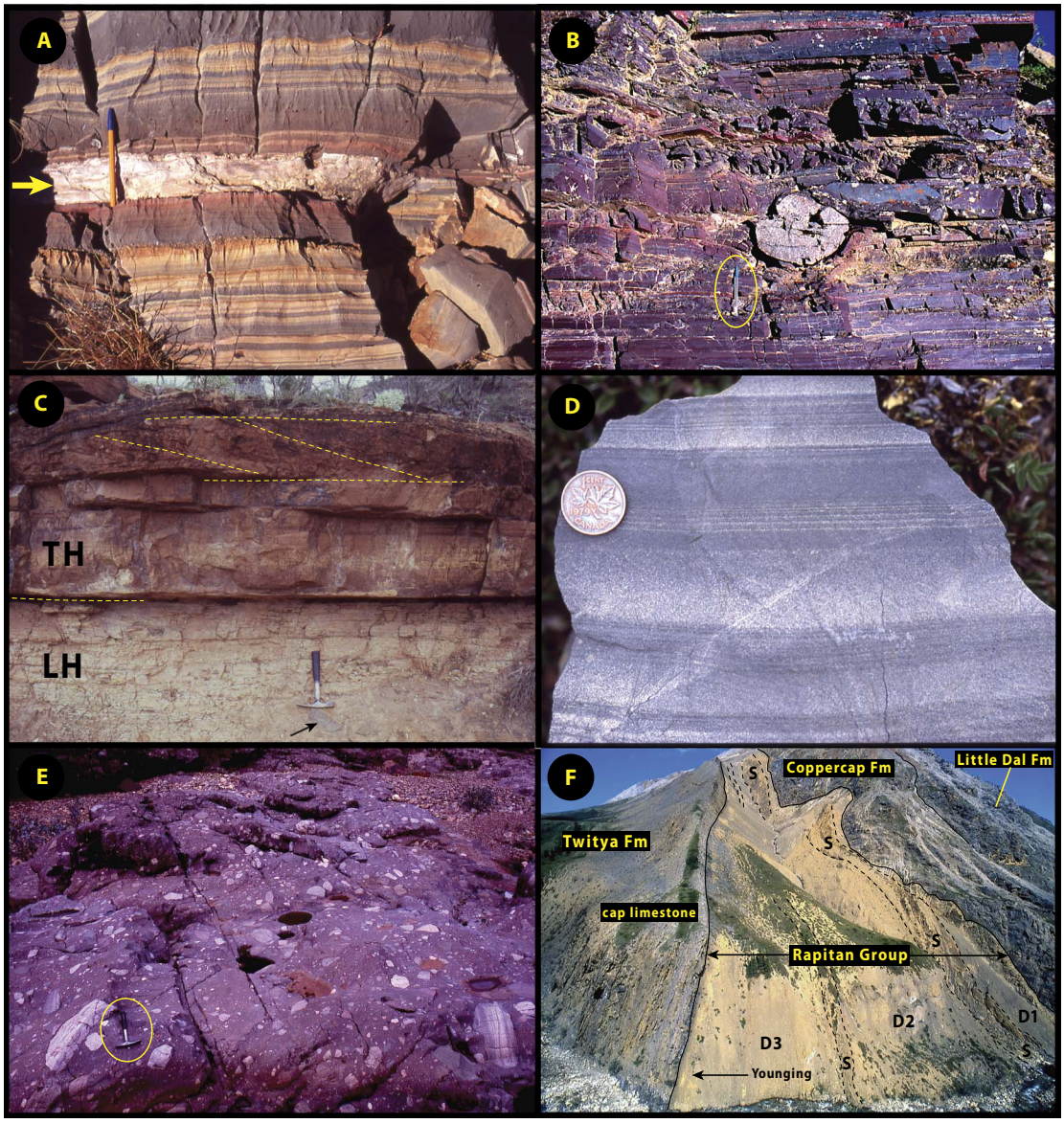

Fig. 19. Cryogenian glacial deposits and cap carbonates. (**A**) Volcanic ash layer (arrow) in Marinoan marine periglacial Ghaub Formation on the foreslope of the Otavi Group carbonate platform, Fransfontein, Namibia. Detrital carbonate host includes suspension fallout (tan) and turbidites (gray). The pen is 15 cm long. The reddish color is Fe stain related to the ash layer. Such Marinoan ash layers are cited as evidence for open water (*83*), but the ash could have fallen anywhere on a sea glacier and could have been advected to the sublimation zone (Fig. 12C), where it would eventually be flushed through a moulin into the subglacial ocean (Fig. 18B). The flushing process would concentrate the ash spatially as many interconnected ponds may drain through a single moulin. The potential for dispersal by currents in the subglacial ocean is a fate that is shared by ash falling into an ice-free ocean. (**B**) Sturtian synglacial iron formation with ice-rafted dropstone (extrabasinal quartz monzonite) in the uppermost Sayunei Formation (Rapitan Group), near Hayhook Lake, Mackenzie Mountains, Northwest Territories, Canada. The pen is 15 cm long. The iron formation occurs directly beneath a kilometer-thick ice grounding-zone diamictite complex (Shezal Formation) and is inferred to have been deposited in front of an advancing tidewater ice margin. (**C**) Sturtian cap dolostone [basal Tapley Hill Formation (TH)] with low-angle cross-bedding sharply overlies syndeglacial siltstone [Lyndhurst/Wilyerpa Formation (LH)] bearing ice-rafted dropstones (arrow), Kingsmill Creek, near Tillite Gorge, Arkaroola Wilderness Sanctuary, Northern Flinders Ranges, South Australia. The 1- to 2-m-thick siltstone is underlain by ~1.5 km of synglacial boulder diamictite (E) of the Sturtian Merinjina/Bolla Bollana Formation (Umbaratana Group). The hammer handle is 33 cm long. The shallow-water cap dolostone is unusually well developed for a Sturtian cap-carbonate sequence (*476*). (**D**) A typical Sturtian cap carbonate—micritic organic-rich limestone with graded calcilutite turbidites, basal Twitya Formation (Windermere Supergroup), Gayna River, Mackenzie Mountains, Northwest Territories, Canada. The coin is 2 cm in diameter. (**E**) Massive Sturtian diamictite of the Merinjina/Bolla Bollana Formation, Tillite Gorge, Arkaroola Wilderness Sanctuary, Northern Flinders Ranges, South Australia. A ~1.5-km-thick ice grounding-zone deposit, composed of massive and stratified diamictites and conglomerate (*497*, *498*), is draped by deglacial siltstone and a shallow-water Sturtian cap dolostone (C). (**F**) Sturtian glaciomarine sequence (Rapitan Group) and cap limestone [basal Twitya Formation (Fm)] near Stoneknife River (64°41.822′N, 129°53.629′W), Mackenzie Mountains, Northwest Territories, Canada. The 114-m-thick Rapitan Group comprises three massive (D1, D2, and D3) and two stratified (S) diamictite units. It disconformably overlies carbonates of the Little Dal and Coppercap formations. The sharp-based, 40-m-thick cap limestone features hummocky cross-bedding basally, indicating accumulation above storm wave base. The cap limestone is gradationally overlain by dark gray shale (maximum flooding) and a siltstone-dominated highstand system tract hundreds of meters thick. Paleomagnetic data (*33*, *127*) indicate a subtropical paleolatitude for this location at the Sturtian glacial onset, consistent with the carbonate-rich pre- and post-Sturtian succession (*148*).

downstream of a moulin would be trophically logical (Fig. 18B) in water >33 m deep to avoid chronic dislodgement by "anchor" ice (*374*). The showstopper for this scenario might be the salinity of subglacial seawater. If we take the volume of the sea glacier under high and low dust fluxes (*168*) and the volume of all continental ice sheets during early (low CO_2), middle, and late (high CO_2) phases of a cryochron (*100*), then salinities of the residual seawater would be 46.6 to 47.6 ppt in the early and middle phases and 38.2 to 39.2 ppt in the late phase, assuming nonglacial Cryogenian seawater had a salinity of 35 ppt, equal to modern values. If the salinity tolerances given in the previous paragraph are representative of early sponges and cnidarians, then the early and middle phases of a cryochron are problematic. Steep, time-dependent salinity gradients would exist close to moulins and subglacial meltwater discharge sites at ice grounding lines (*375*). These are schizohaline environments, requiring salinity-induced dormancy for survival during periods of low-salinity stress. However, experiments suggest that low temperatures reduce low-salinity tolerance in dormancy (*376*). One possibility is that ice-free Cryogenian seawater, following a major evaporite "dump" ~800 Ma (*361*, *377*–*379*), was >5 ppt less saline than the modern ocean. Failing this solution, the schizohaline nature of the Snowball ocean presents a paradox for the early evolution of sponges and possibly cnidarians. The paradox disappears if the 24-isopropylcholestane biomarker from the Cryogenian of Oman (*46*, *48*) is not diagnostic of sponges (*380*), molecular-clock dating of the animal radiation (for example, Fig. 3) is wildly erroneous, and the choanoflagellate-animal divide did not actually occur until the earliest Cambrian (*381*). The origin of animals would then be unrelated to Snowball Earth.

Expanded freshwater oligotrophy on Snowball Earth and the origin of modern marine planktonic cyanobacteria

The last common ancestors of major clades of modern marine planktonic cyanobacteria were Neoproterozoic in age, according to phylogenomic (135 proteins and 2 ribosomal RNAs), Bayesian relaxed molecular clock (18 proteins, SSU, LSU, and *rpoC1*), and Bayesian stochastic character-mapping analyses from 131 cyanobacterial genomes (*382*, *383*). These clades include important nitrogen fixers, both filamentous (for example, Nostocales) and unicellular (for example, *Cyanothece* and *Crocosphaera*), as well as the most abundant organisms in the modern ocean, the non–nitrogen-fixing picocyanobacteria *Synechococcus* and *Prochlorococcus* (the marine *SynPro* clade). These clades all evolved in the early Mesoproterozoic (Fig. 2) and inhabited fresh water until Cryogenian time. Thereafter, they were marine (*383*). The unicellular planktonic *SynPro* clade evolved from a filamentous benthic ancestor (*383*). The modern planktonic filamentous form, *Trichodesmium*, apparently evolved from a Mesoproterozoic benthic filamentous marine ancestor (*383*). The clade represented by *Trichodesmium* may have survived Cryogenian Snowball Earth in marine hydrothermal environments. But what caused the freshwater clades to invade the ocean in mid-Neoproterozoic time?

Aside from *Trichodesmium*, the above clades are prominent in modern polar nonmarine ecosystems, including cryoconite holes and ponds, glacial meltwater streams, and meromictic (salinity-stratified) ice-capped lakes (*271*, *272*). Nitrogen-fixing *Nostoc* is a major component of benthic mats in these environments, and the globally highest known concentrations of *Synechococcus*, up to 15 million cells ml^{-1}, are found in the summer mixolimnion of a well-studied Antarctic saline lake (*384*, *385*). *Synechococcus* is also the dominant photosynthetic cell type in High Arctic coastal lakes (*272*). In contrast, picocyanobacteria are notably rare or absent in the polar oceans (*272*, *348*, *386*), where diatoms are the dominant phytoplankton. These observations suggest that the success of cyanobacteria in polar nonmarine ecosystems is not due to cold tolerance but to tolerance of oligotrophy (nutrient starvation) (*348*).

On the Snowball Earth, the total area of oligotrophic freshwater ecosystems greatly expanded (Fig. 18A). Cryoconite holes and ponds dotted the sublimation zone of the sea glacier, amounting to 12% of global surface area. As atmospheric P_{CO_2} (partial pressure of CO_2) rose, ice sheets receded (Fig. 10), causing dust and surface meltwater production to rise and meromictic ice-capped lakes to multiply. The Sturtian cryochron gave freshwater oligotrophs 58 My to press their advantage. When it ended, the former cryoconite dwellers, along with the coastal lacustrine populations, dispersed by postglacial marine inundation, found themselves in the meltwater lid of the global ocean (*154*). Surface waters warmed rapidly, to their benefit, and salinification (to which they were not intrinsically sensitive) was gradual over tens of thousands of years, because whole-ocean mixing was retarded by the stable density stratification (*387*). The evolving planktonic cyanobacterial clades were soon pushed away from nutrient-rich coastal waters but found permanent homes for which they were preadapted in the oligotrophic ocean gyres (*388*).

SUBGLACIAL OCEAN DYNAMICS AND THE FATE OF FLUSHED CRYOCONITE

What was the fate of the cryoconite that was flushed into the subglacial ocean? Where should we look to find its sedimentary record, including the molecular and body fossils that record should contain? We are unaware of a Cryogenian abyssal sediment record, but this may be more through lack of recognition than lack of preservation (*389*). Decametric accumulations of fine-grained detrital sediment do occur in many Cryogenian synglacial sequences deposited on paleocontinental margins (Fig. 5). Some may be composed of cryoconite, whereas others settled from suspension plumes sourced from discharges of sub–ice-sheet meltwater at ice grounding lines (Fig. 15D) (*375*). Grounding-line meltwater plumes could occur at any paleolatitude, and their organic content would likely be detrital. Cryoconite deposits should only occur at low paleolatitudes, and recent modeling of Snowball ocean circulation (*390*–*393*) is directly relevant to the search for Cryogenian cryoconite deposits.

Subglacial ocean dynamics

The modern ocean has a stable density stratification over most of its area because of heating from the top by solar radiation (*394*). Deep water is close to the freezing point because it originates as polar surface water. The rate-limiting step in the meridional overturning circulation (MOC) is lifting the cold dense deep water back to the surface. This is accomplished through the input of mechanical energy, which is provided by tides and winds (*395*, *396*). On account of the large sea-level fall (*397*), tidal mixing was stronger in the Snowball ocean because little tidal energy was dissipated on shelves (*398*). However, the centrality of wind-driven mixing in the dynamics of the modern ocean misled many into assuming that if the ocean was shielded from winds by a global ice cover, the circulation should tend to stagnate.

The Snowball ocean has no stabilizing density stratification to overcome. It is heated only at the base, by the geothermal flux, and loses heat at the top by diffusion through the ice. Because sea-glacier flow maintains a near-uniform ice thickness (Fig. 8C), the rate of heat loss increases with latitude because of the surface air temperature gradient

(*393*). Sea-glacier flow transports latent heat and fresh water but is ponderously slow (Fig. 16, A and B). In contrast to the modern ocean, the basally heated Snowball ocean is turbulent and weakly stratified (Fig. 20, A and B) (*17*, *390*–*393*). The modern ocean also receives geothermal heat, but the average geothermal flux (~0.1 W m^{-2}) is three orders of magnitude less than the absorbed solar flux.

The first attempt to model the circulation of a subglacial ocean was published, as an appendix, in 2011 (*17*). In a coupled MITgcm, a global ice cover is allowed to thicken, in the absence of geothermal input, to 200 m at the poles and 175 m at the equator, at which point the rate of cooling slows. This is explicitly a nonequilibrium solution at a quasi–steady state. Equatorward ice flow advects latent heat and fresh water, whereas eddy-induced circulation in the subglacial ocean results in low-latitude upwelling and high-latitude sinking (*17*). Even without basal heating, the circulation is remarkably strong, reaching 30 sverdrup (1 sverdrup = 10^6 m^3 s^{-1}) at high latitudes (*17*) or about 50% stronger than the North Atlantic MOC in the present ocean.

More comprehensive studies (*390*–*392*) using the same MITgcm ocean model are coupled to 1D and 2D ice-flow models. Geothermal heating is included, with enhanced heating over an MOR, like that which accommodated the breakup of Rodinia (Fig. 5). The MOR is prescribed at the equator or alternatively at 20° or 40°N. Geothermal input is balanced by diffusive heat loss through the ice cover. Seawater salinity and its freezing point are adjusted for a glacioeustatic fall of ~1.0 km. The model is run in 2D without continents (Fig. 20, A to G and I) and in 3D with a Marinoan paleogeography (Fig. 21). The equatorial sector is modeled at high resolutions with a simplified continent (Fig. 20H). A strong MOC (on the order of 30 sverdrup), driven by weak meridional density gradients due to geothermal and surface heating, is concentrated within 5° of the equator because of the vanishing of the Coriolis force (Figs. 20C and 21, B and E) (*390*, *391*). The temperature and salinity ranges in the ocean interior are only ~0.3°C and ~0.4 ppt, respectively, in the 2D model (Fig. 20, A and B) and even smaller in the 3D simulations (*391*).

The equatorial zone of intense MOC (EMOC) is accompanied by strong zonal jets that reverse direction with depth (*390*–*392*). With the MOR at the equator (Fig. 20, F and G), the shallow flow is eastward, and the deep flow is westward. The jets become antisymmetric when the MOR is located off the equator, with the shallow flow directed westward in the hemisphere with greater geothermal input and eastward in

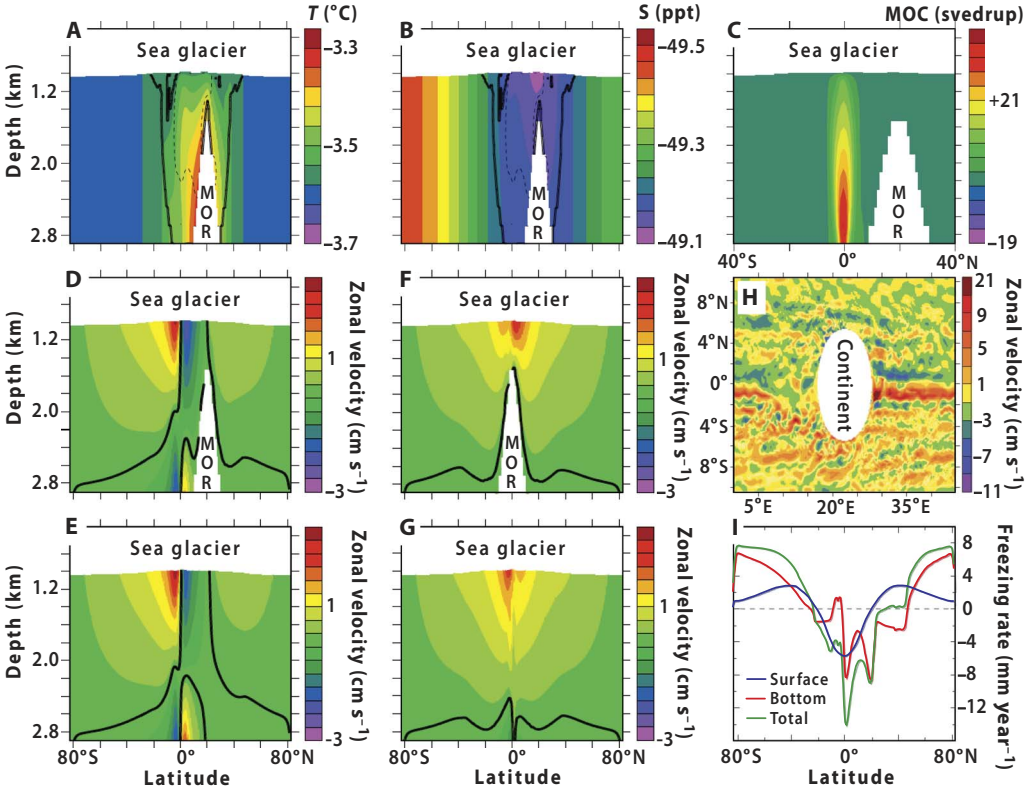

Fig. 20. Snowball Earth ocean dynamics. Results of a 2D (depth and meridian) ocean model (MITgcm) coupled to a 1D (meridian) ice-flow model (*390*, *391*). Mid-ocean ridge (MOR) has an associated geothermal anomaly, and its elevation is corrected for glacial eustatic lowering. Depth is relative to glacial sea level. (**A**) Temperature, (**B**) salinity, (**C**) MOC stream function, and (**D**) zonal velocity, all with the MOR at 20°N. The total ranges of temperature and salinity are small. Strong low-latitude MOC (35 sverdrup) compares with the present high-latitude North Atlantic MOC (~20 sverdrup). (**E**) As in (D), but with the MOR removed and geothermal anomaly retained. (**F**) As in (D), but with the MOR located at the equator. (**G**) As in (F), but with the MOR removed and geothermal anomaly retained. At shallow depth beneath the sea glacier, zonal flow is directed eastward when the geothermal flux is symmetrical about the equator (F and G). When the geothermal flux is antisymmetrical (D and E), a westward-flowing jet occurs at shallow depth and low latitude in the warmer hemisphere, whereas an eastward-flowing jet occurs in the colder hemisphere. Zonal flow pattern is governed by the geothermal field, not by MOR topography. (**H**) Results of 3D high-resolution sector ocean model showing time-dependent turbulent eddy field. Snapshot of zonal velocity field at 125 m below the ice (1150 m below the surface). The white oval indicates an idealized continent. (**I**) Freezing rate (negative values imply melting) at the ice base (red) and prescribed sublimation and deposition rates at the ice surface (blue) as a function of latitude in the 2D model. The comparison shows that basal freezing/melting contributes as much as if not more than surface deposition/sublimation to sea-glacier thickness.

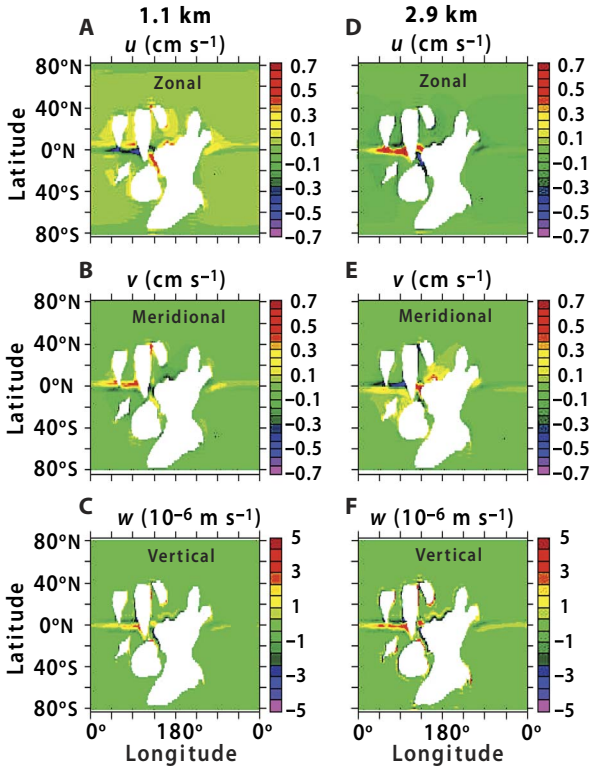

Fig. 21. Snowball Earth ocean circulation, 3D results with Marinoan paleocontinents. (**A** to **F**) Zonal (A and D), meridional (B and E), and vertical velocity (C and F) fields at depths of −1.1 km (A to C) and −2.9 km (D to F) relative to the ice surface (*391*). Ice thicknesses are as given in Fig. 20 (A to D). Scale bars are in centimeters per second (A, B, D, and E) and 10^{-6} m s^{-1} (C and F). Positive velocities are westward (A and D), northward (B and E), and upward (C and F). Zonal and meridional velocities change sign with depth, but vertical velocities do not. Strong vertical mixing (C and F) in the zone where cryoconite flushing occurs (Fig. 18B) expedites abyssal sedimentation of finely suspended material. Zonal shallow jets (A) direct flushed cryoconite toward western or eastern ocean margins, in response to excess geothermal input (as in Fig. 20C) from the northern hemisphere.

the opposite (southern) hemisphere (Figs. 20, D and E, and 21, A and D). The high-resolution, eddy-resolving 3D experiments show an eddy-rich flow field (Fig. 20H). Away from the equator, rows of eddy-driven jets, spaced ~2° apart, resemble eddy-driven jets in the present-day Southern Ocean or the zonal jets in Jupiter's atmosphere in miniature. Both the eddy-driven jets and the equatorial jets, which are not eddy-driven, would be deflected sideways were they to intersect a continent in a well-stratified ocean like the modern ocean. In the unstratified Snowball ocean, the same jets are deflected vertically, creating upwellings where the jets diverge from a continental margin and downwellings where they converge. Coastal upwelling of relatively warm water increases the local rate of ice melting, but open water is unlikely because of ice influx (*392*).

Both the EMOC and the jets exhibit strong time-dependent behaviors (*392*). The eddy-driven jets continually migrate toward the equator. EMOC intensity undergoes short-lived bursts at decadal to multidecadal frequencies, driven in part by pulses of melting associated with cavities in the ice cover. Their magnitude and frequency are strongly dependent on continental boundaries (*392*). Consequently, circulation in the Snowball ocean is richly variable in space and time.

Turbulent eddies outside the EMOC zone have also been studied, at still higher resolution, in the MITgcm (*393*). A turbulent circulation is driven by potential energy released as geothermal heat spread uniformly across the seafloor. The diffusive heat flux through an ice cover of uniform thickness increases with latitude, according to gradients in surface temperature at different atmospheric CO_2 levels. Potential energy release is dominated by baroclinic instability, which drives geostrophic turbulence that transports buoyancy poleward and upward along surfaces of constant density (isopycnals), thereby maintaining a barely statically stable stratification (*393*). Consistent with the coarser-scale results (*390*–*392*), the temperature and salinity gradients in the subglacial ocean are much smaller than in today's ocean (*393*). The new results confirm that a Snowball ocean is well mixed, with eddy velocities and diffusivities within one order of magnitude of the modern ocean (*393*).

How does this help us to find ancient cryoconite? Cryoconite flushing occurs where circulation in the Snowball ocean is strongest (Fig. 21). This should decrease the residence time of cryoconite in the water column, by sweeping it more rapidly onto the seafloor, where grains and flocs are captured. In the modern ocean, respiration in the water column is more efficient than anaerobic remineralization after burial, but sedimentation rate may be less important for organic burial in the anoxic (locally suboxic) Snowball ocean. The azimuthal directions of cryoconite dispersal will be strongly controlled by the zonal jets that hug the base of the sea glacier and are strongest close to the equator (Figs. 20, D to G, and 21A). Cryoconite should therefore accumulate preferentially at low paleolatitudes and on westward-facing continental margins when geothermal input is symmetrical and on westward- or eastward-facing margins, depending on the hemisphere, when the geothermal input is asymmetric.

Sturtian reprise of iron formation

Iron formation is a fine-grained sedimentary rock type with >15 wt % Fe that is most common in successions older than 1.85 Ga (*399*). The only regional-scale iron formations younger than 1.85 Ga are those within Cryogenian synglacial deposits, most or all of Sturtian age (Figs. 4 and 5) (*131*, *159*, *160*, *400*). The main iron-bearing species in Cryogenian iron formations is hematite (Fe_2O_3), typically associated with variable amounts of authigenic chert or jasper (SiO_2) and Fe-rich carbonate. The chert reflects the proclivity of dissolved silica to adsorb onto the hydrous surfaces of ferric oxyhydroxide (ferrihydrite) particles in the water column (*401*), whereas the Fe-rich carbonate is a by-product of the anaerobic respiration of organic matter where Fe(III) is the terminal electron acceptor (*402*, *403*). Cryogenian iron formation is intimately associated in some areas with Mn oxide–rich sediments (*404*). In the absence of local volcanic-hydrothermal activity, iron formation implies (i) anoxic waters where Fe(II) can accumulate in solution; (ii) a limited sulfur flux to prevent complete titration of dissolved iron as Fe sulfide (*405*) or, alternatively, insufficient organic substrate to support microbial sulfate reduction (*406*); and (iii) an oxidizing agent to localize insoluble Fe oxide production.

The reprise of Fe(±Mn) formation after a hiatus of 1.13 Ga was classically taken as evidence for the existence of a Cryogenian Snowball Earth (*24*, *350*). "The presence of floating pack ice should reduce evaporation, act to decouple oceanic currents from wind patterns and, by inhibiting oceanic to atmosphere exchange of O_2, would enable the oceanic bottom waters to stagnate and become anoxic. Over time, ferrous iron generated at the mid-oceanic ridges or leached from the bottom sediments would build up in solution and, when circulation became established toward the end of the glacial period, the iron could oxidize to form a 'last-gasp' blanket of banded iron-formation deposition in

upwelling areas" (*24*). It was subsequently argued that runoff, the main source of sulfate for the ocean, would be attenuated on a Snowball Earth because of the limited hydrologic cycle (*405*), and the hydrothermal Fe/S flux ratio would increase because of glacioeustatic decompression of MORs (*407*). The preferential occurrence of iron formation in the Sturtian cryochron (Fig. 4) might reflect the dominance of basalt weathering in the preceding 10^8 years (*60*, *160*, *174*, *196*, *400*), the synchroneity of paleoequatorial Franklin LIP emplacement with the Sturtian onset (*32*, *199*), intensified seafloor weathering accompanying the initial breakup of the long-lived supercontinent Rodinia (*75*), and the removal of LIP basaltic lava plateaus by Sturtian glacial erosion (*174*). Anomalously high P/Fe ratios in Sturtian iron formations compared with those of other ages (*408*) are compatible with light-limited productivity in the ice-covered ocean (*409*).

Yet, there are problems with the classic scenario (*24*, *350*) in the geological details. The iron formations tend not to occur at the top of Sturtian successions (*409*, *410*), where, in the classic model, they should have been closely associated with cap carbonates, nor are iron formations associated with ocean upwelling areas as originally hypothesized (*24*), but instead, they tend to be localized in semirestricted rift basins and fjords (*219*, *400*, *404*). Finally, pre-Sturtian deep water was already anoxic and ferruginous (*351*–*353*), which implies that the Sturtian reprise of iron formation involved more than glacially induced anoxia. Snowball ocean dynamics provides insights regarding the localization of synglacial iron formation.

Redox-sensitive trace elements and Fe isotopes suggest that Sturtian iron formations formed at redoxclines in the water column, where ferruginous (anoxic and Fe-rich) seawater upwelled into oxygenated water masses (*160*, *350*, *411*–*415*). Unlike chemical sediments in general, Cryogenian iron formations are typically associated with coarse-grained clastic deposits, notably boulder-bearing stratified diamictite (Fig. 7E). Faceted and striated clasts and ice-rafted dropstones (Fig. 19B) identify tidewater glaciers as proximal sources of the debris, which usually includes extrabasinal rocks. This interpretation of the sedimentary facies association makes a compelling case for subglacial meltwater discharge as an oxidizing agent in the precipitation of ferrihydrite or other iron-formation precursors (*404*, *409*, *414*, *415*). The meltwater contains O_2 derived from air bubbles in meteoric ice, assuming O_2 exists in the ambient atmosphere. The low-density meltwater tends to pond between the ferruginous seawater brine and the sea glacier (Fig. 22) but is rapidly dissipated by eddy turbulence in the open ocean (*390*). Flushing conduits for cryoconite meltwater (Fig. 18B), another oxidant source, may be unable to generate localized iron formations because they discharge into the zone of most intense ocean mixing (Figs. 20, C to H, and 21). On the other hand, silled basins like glacial fjords and segmented rift basins offer protection from ocean eddies (Fig. 22) (*390*). They appear to be most consistent with the distribution and facies association of many Sturtian iron formations (*131*, *404*, *409*, *414*, *415*) and may account for their selective occurrence globally (Fig. 5B) (*390*).

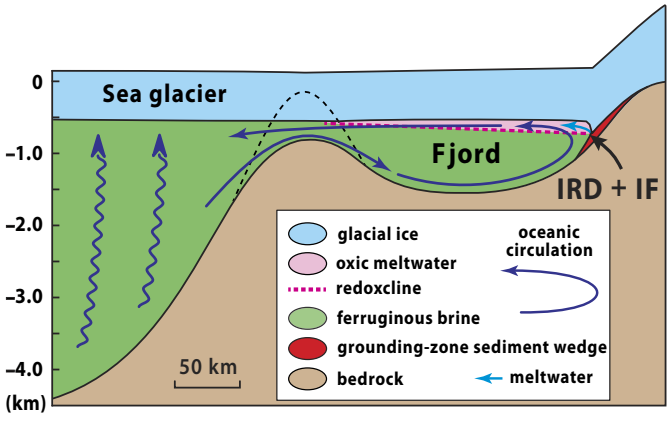

Fig. 22. Depositional model for synglacial iron formation. Fe isotope and redox proxy data suggest that Sturtian iron formations (Figs. 4B and 5B) were deposited at redoxclines where ferruginous waters upwelled into oxygenated meltwater (*160*, *412*). Sedimentary facies associations (Figs. 7E and 19B) and stratigraphic relations imply that iron formation (IF) was deposited near ice grounding lines in semirestricted basins (for example, rift basins, glacial fjords, and overdeeps) (*220*, *400*, *404*, *409*, *415*). Ice-rafted debris (IRD) is concentrated proximal to the ice grounding line because shelf ice moves seaward more slowly than free-floating icebergs.

CAP CARBONATES AND SNOWBALL EARTH AFTERMATHS

"Cap carbonates" (Figs. 19, C, D, and F, and 23 to 26) are laterally continuous, meter- to decameter-thick units of lithologically distinctive carbonate (dolomite and/or limestone) that sharply overlie Cryogenian glacial deposits globally (*97*, *131*, *154*, *155*, *416*, *417*). They typically extend well beyond the areas of subjacent glacial deposits (*156*, *416*, *418*), being associated with marine flooding events ("transgressions") of large magnitude (Fig. 26). Syn- and post-deglacial flooding results from ice-sheet meltdown and ocean thermal expansion (*387*), respectively, modified by ice-sheet gravitational effects and isostatic adjustment of the continental and oceanic lithosphere (*419*). Deposition of cap carbonate extended to at least 50° paleolatitude (*31*, *34*, *35*, *368*), well beyond the Phanerozoic range of nonskeletal carbonate production (*177*). This suggests an anomalous state of carbonate oversaturation in the surface ocean. Cap carbonates are associated with a variety of seafloor cements, including macroscopic crystal fans of former aragonite (Fig. 25H). The crystal fans occur in deposits of intermediate water depth, and locally, they persist through decameters of strata (Figs. 24 and 26C) (*97*, *416*, *420*–*422*). This implies a critical oversaturation seldom attained in the ocean at such depths subsequent to ~1.5 Ga (*423*). In scale and distribution, cap carbonates are unique to Cryogenian glacial aftermaths, and they present a paradox (*176*) inasmuch as (nonskeletal) carbonate deposition is favored by warm surface water and low acidity, seemingly at odds with Snowball deglaciation.

The abrupt superposition of cap carbonate on stratified or massive diamictite led some early workers to postulate a depositional hiatus (*424*). However, the global distribution of the same stratigraphic relationship (Figs. 7C, 19, C and F, 23, and 25, A and B) made this unlikely as a general solution, as did the gradational nature of the contact itself at a fine scale (*97*). Moreover, extrabasinal debris, presumed to be ice-rafted, is occasionally observed within the basal 0.5 m of the cap carbonate, arguing against a hiatus (*425*). The general paucity of pebble lags or other evidence for reworking of the underlying glacial deposits (Figs. 19C, 23, and 25, A and B) suggests that Cryogenian deglacial transgressions were very rapid. As for the cap carbonates, if they were not deposited rapidly, they would have been diluted by detrital input (for example, loess), given the global deglacial environment. A detrital origin for cap carbonate, as carbonate loess (*426*), does not account for its intimate association with seafloor cements (Figs. 7F and 25, E and H) or for the consistent C isotope patterns exhibited by cap carbonates in many areas (*97*, *156*, *427*). It is therefore surprising that magnetostratigraphic records (*428*–*431*), where detrital hematite carries the natural remanent magnetization, imply that certain cap carbonates accumulated extremely slowly,

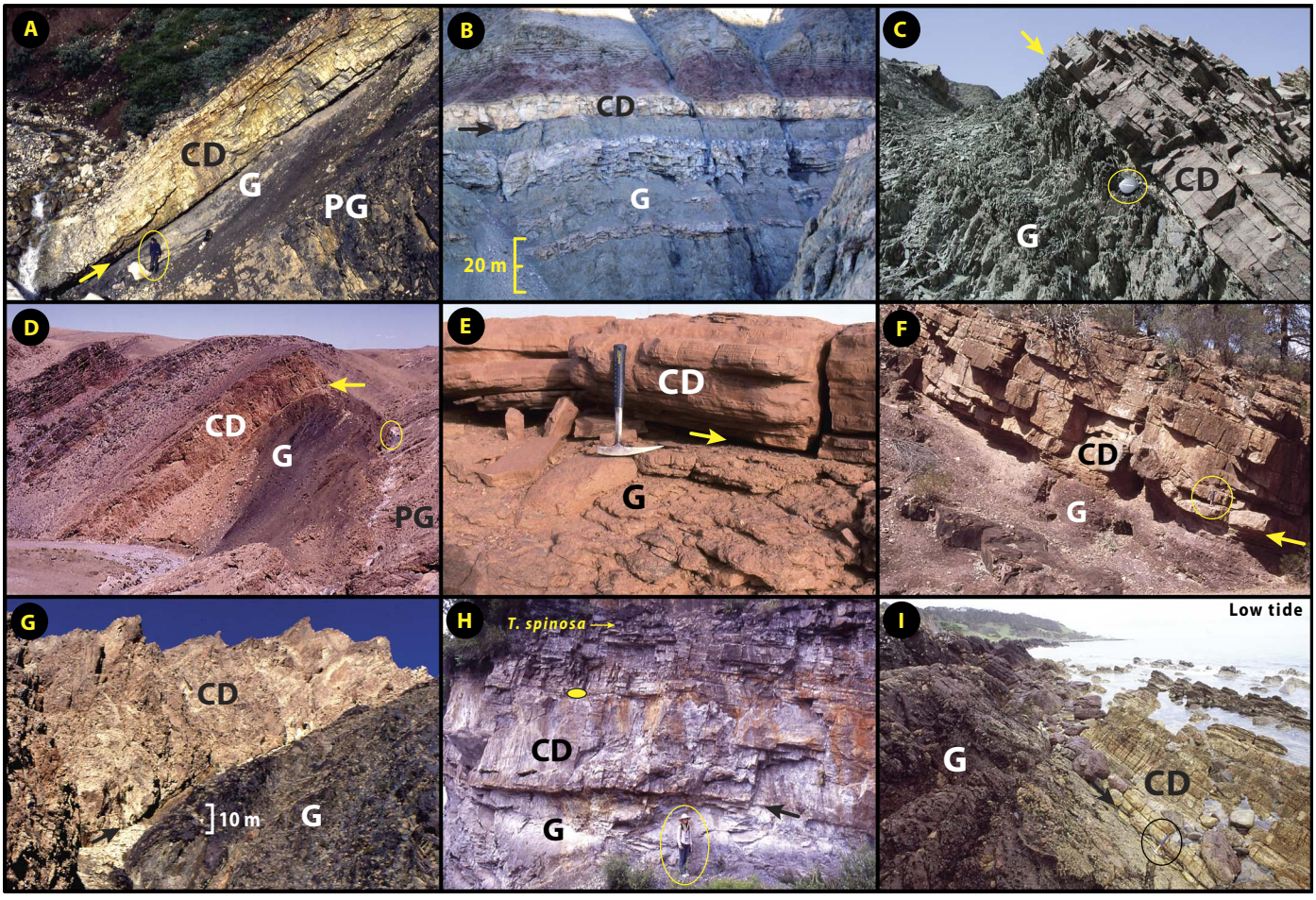

Fig. 23. Global distribution of sharp-based Marinoan postglacial cap dolostones. Distribution of Marinoan cap dolostones over 110° paleolatitude, from South China at 45°N (H) to West Africa at 65°S (E) (Fig. 5A), records an anomalous state of carbonate oversaturation in the surface ocean despite extreme CO_2 acidification in the Snowball aftermath (*73*, *74*, *84*–*91*). Other Marinoan cap dolostones are imaged in Figs. 7C and 25B. PG, preglacial carbonate strata; G, glacial-periglacial deposits; CD, cap dolostone. Arrows mark sharp basal contacts. (**A**) Ravensthroat Formation (CD) on Stelfox Member, Ice Brook Formation (G), and Keele Formation (PG), Arctic Red River, Mackenzie Mountains, Northwest Territories, Canada (*409*, *416*, *499*). (**B**) Basal Canyon Formation (CD) on Storeelv Formation (G), Tillitekløft, Kap Weber, Kejser Franz Joseph Fjord, East Greenland (*139*, *334*). Resistant layers of quartz sandstone within glacial diamictite were eroded from unlithified preglacial marine sandstones. Photo courtesy of E. W. Domack. (**C**) Basal Zhamoketi Formation (CD) on Tereeken Formation (G), Yukkengol, Quruqtagh, Xinjiang, China (*500*). A lens cap is used for scale. Photo courtesy of S.-H. Xiao. (**D**) Basal Ol Formation (CD) on Khongor Formation (G) and Taishir Formation (PG), Khongoryn, Zavkhan, western Mongolia (*143*, *501*). (**E**) Amogjar unit (CD) on Jbéliat Group (G), Atar, Adrar, Taoudeni Basin, Mauritania (*161*). (**F**) Nuccaleena Formation (CD) on Elatina Formation (G), Elatina Creek, Central Flinders Ranges, South Australia (*427*). (**G**) Sentinel Peak Member (CD) of the Noonday Dolomite on Wildrose Member (G) of the Kingston Peak Formation, Goller Wash, Panamint Range, Death Valley area, eastern California, USA (*469*, *470*). (**H**) Basal Doushantuo Formation (CD) on Nantuo Formation (G), Huajipo section, Yangtze Gorges, northern Hunan, South China (*417*). *Tianzhushania spinosa* arrow indicates the first appearance of chert nodules preserving diapause cysts containing eggs and embryos of stem-group metazoans (*502*, *503*). The yellow oval marks a volcanic ash layer yielding zircons dated at 635.2 ± 0.5 Ma (*57*). (**I**) Cumberland Creek Dolostone (CD) on Cottons Breccia (G), Grimes Creek, King Island, Tasmania (*504*). Igneous zircons from the topmost meter of the Cottons Breccia are dated at 636.41 ± 0.45 Ma (*59*).

over several 10^4 or 10^5 years, provided one assumes that the time scale for a 635-Ma geomagnetic polarity reversal was broadly similar to that of the most recent polarity reversals (*432*). This assumption, however, must now be questioned in light of revised histories of inner-core inception and growth (*433*–*435*), as discussed in the "Time scale for cap-carbonate transgressions" section.

Cap carbonates and sequence stratigraphy

Before proceeding, we need to clarify and distinguish the terms "cap carbonate," "cap-carbonate sequence," and "cap dolostone." The first and last were popularized by field geologists in Australia, where they are directly overlain by deeper-water shale or siltstone, making their lithology-based definition self-evident. But what about the successions in Namibia (*436*), Amazonia (*437*), Mongolia (*143*), and elsewhere, where the background sediments are also carbonates? Terrigenous and/or carbonate successions can be described in terms of "sequence stratigraphy" (Fig. 24), which relates to inferred secular changes in relative sea level (Fig. 26). A "cap-carbonate sequence" (*29*) is the depositional sequence associated with net coastal marine inundation and sedimentation, resulting from global ice-sheet meltdown and whole-ocean warming (*387*, *419*). The sequence comprises a deepening-upward "transgressive system tract" (TST), a "maximum flooding" (MF) interval or zone, and a shallowing-upward "highstand system tract" (HST) that ends at a subaerial exposure surface ("sequence boundary") or its

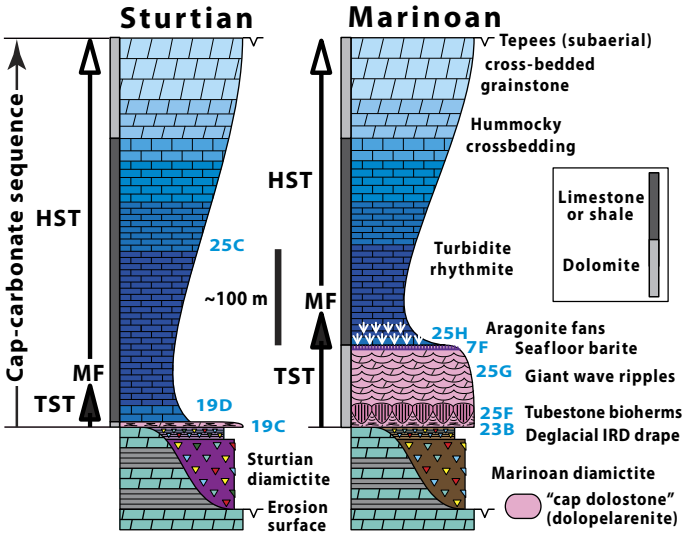

Fig. 24. Lithostratigraphic comparison of idealized Sturtian and Marinoan cap-carbonate sequences. Closed arrows indicate the upward-deepening TST, MF indicates the maximum flooding stage, and open arrows indicate the upward-shallowing HST. TSTs are thin or absent in most Sturtian examples (but see Fig. 19C). Vertical bar indicates limestone (dark gray) or dolostone (light gray). "Cap dolostone" was deposited in surface water (above prevailing wave base) diachronously during shelf flooding, based on sedimentary structures indicated on the right. Numbers in blue are keyed to images in the accompanying figures. Tubestone stromatolite (*441*), giant wave ripples (*443*), and seafloor barite (*91*) are rare or absent outside of Marinoan cap dolostones, and benthic aragonite fans are developed to the same degree only in carbonates >1.5 Ga (*423*, *505*). Sheet-crack cements (Fig. 25E) substitute for tubestone stromatolite in downslope areas (*425*). Relatively condensed Sturtian TSTs may reflect more deeply subsided continental margins because of the greater duration of the Sturtian cryochron (Fig. 2). Expanded Sturtian TSTs would be shifted landward, where net subsidence was less, but the record was more susceptible to later erosion.

downslope conformity. In sequence-stratigraphic terms, the synglacial sediments represent "lowstand" deposits (Fig. 26A) and are preceded in some areas (*97*) by a distinct "falling-stand" wedge (Fig. 26A).

On subsiding margins (*148*, *150*, *157*, *437*), cap-carbonate sequences are anomalously thick (hundreds of meters), reflecting accommodation space created by tectonic subsidence accumulated over the preceding cryochron (*436*), when sedimentation rates were low (*169*). Conversely, cap-carbonate sequences are condensed through the lack of accommodation on margins where subsidence rates are low (*161*, *417*). Cap-carbonate sequences commonly lack evident higher-order parasequences, unlike other depositional sequences of comparable magnitude in the same succession (*144*). "Cap carbonates" make up part (rarely all) of the TST in cap-carbonate sequences. As noted, the overlying MF interval and HST may be terrigenous (*148*, *150*) and/or carbonate (*143*, *144*, *437*) in composition.

"Cap dolostone" is a particular type of cap carbonate, most often Marinoan in age, which is composed of pale-colored (beige or pinkish) dolomite with a palimpsest peloidal texture—a "dolopelarenite" in Folk's classification (*438*)—and a suite of sedimentary structures indicating wave action and phototropy. The structures include low-angle swaley cross-stratification (*131*, *439*), tubestone- and gutter-type stromatolites (*416*, *440*–*442*), and giant wave ripples (*31*, *443*). Cap dolostones commonly end stratigraphically below the MF interval (Fig. 24), meaning that they do not encompass the entire TST. Locally, a postglacial unit of deeper-water limestone turbidites appears stratigraphically below the cap dolostone (*425*). Most Marinoan cap-carbonate sequences begin with cap dolostones (Fig. 23), whereas Sturtian cap dolostones (Fig. 19C) are exceptional.

Cap carbonates and postglacial ocean stratification

A central challenge in the interpretation of cap-carbonate sequences is the rapidly changing physical and chemical stratification of the ocean at that time (Fig. 26) (*154*, *387*, *444*, *445*). The subglacial Snowball ocean was hypersaline, close to the freezing point, and geochemically evolved (*74*, *75*, *84*) through volcanic outgassing, basalt-seawater exchange reactions (at high and low temperatures and reduced hydrostatic pressures), and weathering of fine-grained continental detritus injected by ice-sheet and cryoconite meltwater discharges (Figs. 15D and 18B). Note that proxy data for the Snowball ocean are severely limited because normal marine carbonate was not produced during the cryochrons owing to ocean acidification. Purported synglacial marine carbonate cements (*446*) are apparently preglacial in age, based on field relations. At a Snowball termination, rapid melting of the sea glacier and all existing ice sheets floods the ocean with low-density meltwater (*97*, *154*), forming a gravitationally stable lid, roughly 1 to 2 km deep, over the evolved Snowball brine (Fig. 26B). The meltwater lid rapidly warms beneath the CO_2-rich atmosphere—sea surface temperatures are predicted to reach 40° and 60°C at the poles and equator, respectively (*387*). Surface warming enhances the stable density stratification. The meltwater lid equilibrates chemically with the CO_2-rich atmosphere, driving pH lower. Rapid weathering of subaerially exposed carbonate platforms and loess provides alkalinity to the deepening and warming meltwater lid. Runoff and warming drive the meltwater to critical $CaCO_3$ oversaturation (*84*, *447*). Doubt has been expressed that weathering was sufficiently strong to accomplish this, noting that runoff does not scale linearly with atmospheric CO_2 (*75*, *448*). However, it is not only the higher runoff that catalyzes weathering as ice sheets retreat but also the lowstand of sea level (*84*), low pH of meteoric waters (*449*), and the enormous reactive surface area of shattered rock and unweathered loess particles (*447*).

Giant wave ripples (*443*) and other wave-generated features show that cap dolostones were deposited in the mixed layer of the meltwater lid (Fig. 26B), with some input of Snowball-evolved brine through vertical mixing (*445*). Their primary mineralogy is unknown—dolomitization is postulated to occur at shallow depth below the sediment-water interface (*449*–*451*), possibly mediated microbially during methanogenesis (*452*). On some time scale, the stable density stratification of the meromictic ocean is destroyed by tide- and wind-driven mixing (*387*). Geochemically evolved Snowball water then mixes into the surface ocean, where it can be expressed in the neritic carbonate record. How can its geochemical signature be recognized and mapped within cap-carbonate sequences? One possible expression is the rapid upward decrease in radiogenic isotopes, $^{87}Sr/^{86}Sr$ and $^{187}Os/^{188}Os$, observed in the Sturtian cap limestone of northwestern Canada (*60*). In Marinoan cap-carbonate sequences, a candidate horizon is the top of the cap dolostone (Fig. 24), which is marked in some areas (*91*, *131*, *155*, *409*, *453*) by a remarkable layer of seafloor barite (Fig. 7F). Anoxic Snowball brine could be enriched in Ba through seafloor weathering of igneous and detrital feldspar. Barite would be precipitated wherever sulfate was first encountered. Regionalization of seafloor barite could relate to upwellings, consistent in Marinoan paleogeographies (*34*, *368*) with Ekman pumping on the northern Australian and western Laurentian margins (Fig. 5A), where seafloor barite is best developed (*155*, *409*). The top of the barite horizon

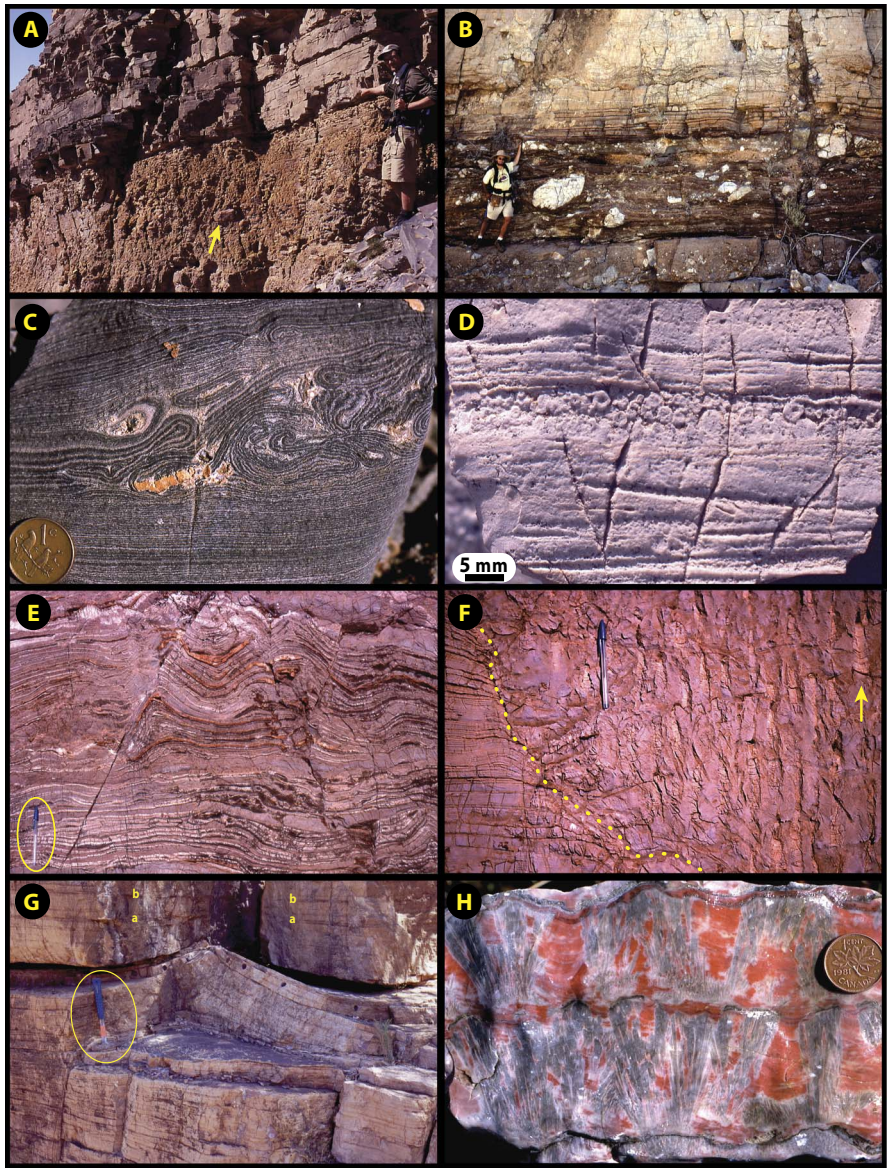

Fig. 25. Distinctive features of Sturtian and Marinoan cap carbonates. (**A**) Sharp sedimentary contact between Sturtian glaciomarine Maikhan Ul Formation with ice-rafted dropstones (arrow) and overlying organic-rich and fossiliferous cap limestone (basal Taishir Formation), Zavkhan basin, western Mongolia (*63*, *143*). Co-author F.A.M. points to the contact. (**B**) Sharp sedimentary contact between Marinoan glaciomarine Ghaub Formation (Bethanis Member) with ice-rafted dropstones and overlying cap dolostone (Keilberg Member of the Maieberg Formation) on the foreslope of the Otavi carbonate platform, northern Namibia (*97*). Co-author G.P.H. points to the contact. (**C**) Microbialaminite with roll-up structures in Sturtian cap carbonate (middle Rasthof Formation), northern Namibia. The coin is 2 cm in diameter. Roll-ups are associated with neptunian dikes and indicate that biomats were cohesive and pliable (*475*, *478*), but the metabolic basis for their growth, inferentially below the photic zone, remains undetermined. (**D**) Macropeloids and low-angle cross-stratification in characteristically organic-poor Marinoan cap dolostone, Keilberg Member of the Maieberg Formation, northern Namibia (*97*). Sorted peloids and low-angle cross-stratification are characteristic of cap dolostones and indicate sedimentation at depths above fair-weather wave base. Coarse grain size suggests that macropeloids were less dense than pure carbonate when deposited. (**E**) Sheet-crack cements composed of fibrous isopachous dolomite (tinted orange by desert varnish where selectively silicified) occur regionally in the basal 2 m of the Marinoan cap dolostone in downslope settings in Namibia (*425*). The pen (circled) is 15 cm long. Sheet cracks and cements imply pore-fluid overpressure and an alkalinity pump, respectively, at shallow depth beneath the sediment-water interface at the onset of cap carbonate sedimentation. Overpressure could be related to rapid base-level fall due to the gravitational effect on the ocean of the loss of nearby ice sheets (*419*). (**F**) Upward-expanding mound of tubestone stromatolite (Figs. 24 and 26B) characterized internally by geoplumb (paleovertical) tubes (arrow) that were filled by carbonate mud as the mound grew. Mound margin (dotted line) is flanked by mechanically bedded dolopelarenite (lower left), Marinoan cap dolostone (Keilberg Member), northern Namibia (*97*). (**G**) Giant wave ripple (Fig. 24) in the Marinoan cap dolostone (Nuccaleena Formation) at Elatina Creek, central Flinders Ranges, South Australia. Note gradual amplification at the level of the hammer (circled, 35 cm long) and correlation of overlying layers a and b. Such unusually large and steep wave ripples occur in Marinoan cap dolostones on several paleocontinents, and the regional and global mean paleo-orientations of their crestlines are meridional (*31*, *443*). Single wave trains aggrade as much as 1.4 m vertically, implying steady growth under the influence of long-period waves during Marinoan deglaciation (*443*). Intraclasts and composite grains are typically absent, suggesting that the characteristic steepness of the ripples is not related to early lithification [contra Lamb *et al.* (*506*)]. (**H**) Calcitized crystal fans (gray) formed as prismatic aragonite seafloor cement (Figs. 24 and 26C) in the Hayhook Formation stratigraphically above the Marinoan cap dolostone in the Mackenzie Mountains, Northwest Territories, Canada (*409*, *416*). Growth of seafloor cement was coeval with sedimentation of lime mud (pink) from suspension. Seafloor aragonite precipitates up to 90 m thick occur in Marinoan cap limestones and mark the return of a depositional style last common before ~1.5 Ga (*421*, *423*).

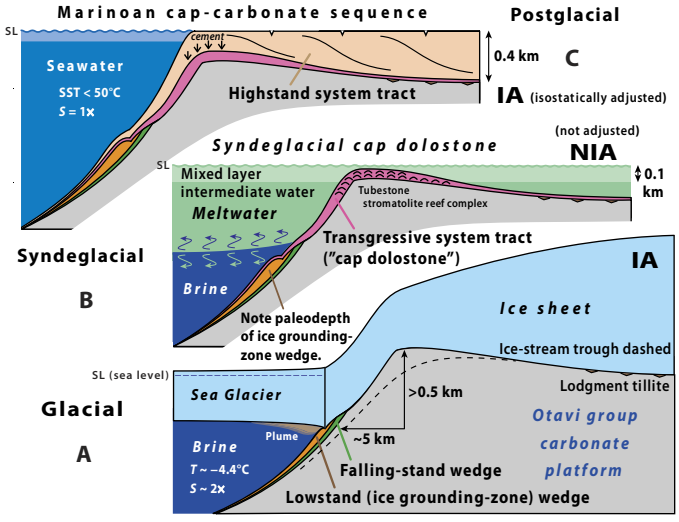

Fig. 26. Three-stage paleoceanographic model for Marinoan cap-carbonate sequences. (**A**) During the Snowball cryochron, net base-level fall (glacial eustasy > glacial isostasy + ice gravity) causes falling-stand and ice grounding-zone wedges to form on the continental slope, whereas lodgement till is deposited locally above sea level. Salinity of seawater may double, as a result of freshwater sequestration in ice sheets and sea glacier, and the freezing point is lowered accordingly. Glacial action supplies carbonate eroded from the platform to the ocean as suspended load in meltwater plume and grounding-zone wedge. (**B**) During deglaciation, meltwater production and surface warming create stable density stratification (*387*). The kilometer-thick meltwater lid (Glacial Lake Harland) includes an oxygenated mixed layer and intermediate water that is at least regionally anoxic, presumably due to respiration of surface organic export production. Marinoan cap dolostone was deposited diachronously from the meltwater mixed layer as base level rose and the glacierized landscape was flooded. The time scale for base-level rise may exceed the ice-sheet melting time scale because of whole-ocean warming and thermal expansion as destratification occurs (*387*) and over the peripheral bulges of former ice sheets, which collapse on the time scale of isostatic adjustment (IA) (*419*). (**C**) After ice sheets have melted, the meltwater lid mixes with the chemically evolved Snowball brine, which finally warms (*387*). The HST of cap-carbonate sequences fills in areas where net accommodation remains after GIA and hydro-isostatic adjustments. Landward progradation is inferred from inclined surfaces of constant carbonate $\delta^{13}C$ (*97*).

generally coincides exactly with a mineralogical and petrographic switch. Dolopelarenite is replaced by Ca-micrite, interspersed with benthic crystal fans of former aragonite (Fig. 7F). The significance of this change in mineralogy has not been explained. The change in textures remains evident even where the limestone was replaced during burial dolomitization. It was previously inferred (*156*) that the tops of Marinoan cap dolostones are diachronous and record the base of the mixed layer entirely within the meltwater lid (Fig. 26B). If this were true, then the top of cap dolostones should invariably coincide with storm wave base, the upward disappearance of storm-related bedforms. On the other hand, if the top of cap dolostones marks the invasion of evolved Snowball water, storm wave base should cross that horizon diachronously, from within the cap dolostone to above it in a landward direction. In some sections, wave-worked strata pass upward into turbidites within the cap dolostone (*156*), showing that the change in seafloor mineralogy did not invariably coincide with the base of the mixed layer. Identifying the destratification horizon within cap-carbonate sequences is important for many reasons, one being that it should be possible to estimate the time scale for post-Snowball ocean destratification in models (*387*) with useful ($\log_{10}$) accuracy.

The time scale for mixing and warming the stratified ocean of a Snowball aftermath has been estimated from energy constraints and in a 1D vertical mixing model (*387*). Assuming that a 2-km-deep meltwater lid at 15°C was emplaced, on a time scale of 2 ky, over a 2-km-deep brine at −4°C, energetic constraints suggest that the time scale for whole-ocean mixing would be ~6×10^4 years, with an uncertainty range between 10^4 and 10^5 years (*387*). In the 1D vertical mixing model, the time scale for complete destratification and whole-ocean warming (to a uniform 50°C) is 5.8×10^4 years for a 2-km-deep meltwater lid and 4.2×10^4 years for a 1-km-deep meltwater lid (*387*). The rate at which the meltwater is emplaced has only a small effect (<11%) on the mixing time (*387*). The geological significance of these results highlights the need for improved understanding of small-scale turbulent mixing.

Time scale for cap-carbonate transgressions

Although Sturtian and Marinoan cap carbonates have been radiometrically dated (Table 1), existing geochronology does not resolve the time scale over which they were deposited. Sedimentary structures in cap carbonates are consistent with rapid accumulation (*420*, *425*, *440*, *443*), but this evidence is qualitative. On the other hand, the increase in base level corresponding to the TST of cap-carbonates sequences (Fig. 24) is the result of known physical processes amenable to numerical modeling (*387*, *419*). The key processes are ice-sheet melting, gravitational interaction between ice sheets and the ocean, changes in planetary rotation, isostatic adjustments of the solid earth to shifting loads of ice and meltwater, and the thermal expansion of seawater. The net result is a complex evolving mosaic of base-level changes of large magnitude (*419*).

Snowball deglaciation is accompanied by a large rise in the global mean sea level due to the melting of grounded ice sheets (*419*). The magnitude of this rise is in the 0.2 to 1.0 km range, depending on the ice-sheet volume, which is a function of CO_2 and orography at the time when terminal deglaciation began (*100*). The time scale for Snowball deglaciation in a coupled ice-sheet–energy-balance model is ~2 ky (*327*). This is a realistic estimate given the preponderance of low-latitude Cryogenian ice sheets (Fig. 10), energetic considerations (*116*), and the numerous positive feedbacks in the climate system, particularly ice-albedo, ice-elevation, and ocean-stratification feedbacks. For comparison, the mass-balance changes of modern glaciers across the entire European Alps (at 46°N) averaged −1.63 m $year^{-1}$ water equivalent from 2003 to 2013 (*454*). Even without feedbacks, this rate would remove a 3.6-km-thick ice sheet in 2 ky. As Snowball ice sheets recede, assuming they hold 1000 m of sea-level change equivalent, gravitational and deformational effects cause sea level to fall by several 10^1 m in the near field (*419*). These effects are sufficient to counteract the global mean sea level rise associated with the melting, resulting in a net fall of 10^2 m in the near field (Fig. 27). In the far field, where the gravitational and deformational effects act in tandem with eustasy, sea level rises by over a kilometer (*419*). These results do not include thermal expansion of seawater (*387*), but evidence for early base-level falls is observed in the basal meters of Marinoan cap dolostones in downslope locations (*425*).

The preponderance of low-latitude ice sheets (Figs. 5 and 10) suggests that deglaciation may have been accompanied by reorientation of the rotation axis relative to the solid Earth, also known as true polar wander (*455*). This would in turn drive a significant sea-level signal (*456*, *457*). To accurately model true polar wander and related sea-level changes in response to deglaciation, the longitudinal distribution of the ice sheets must be well constrained, and any "excess ellipticity" of the planet due to lower-mantle convection must be taken into account.

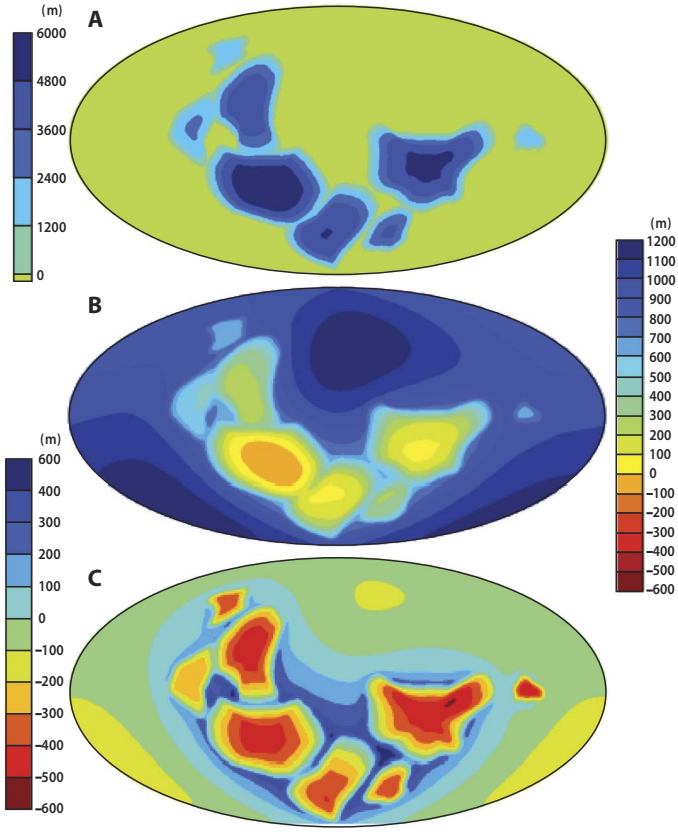

Fig. 27. Relative sea-level (base-level) changes at Snowball terminations. Predicted base-level changes for a globally synchronous Marinoan deglaciation, during which ice sheets decrease in thickness linearly from a glacial maximum (A) to zero thickness in 2 ky while maintaining equilibrium profiles (*419*). Predictions incorporate the effects of glacial eustasy (global mean sea level), ocean–ice-sheet gravitational attraction, and GIA and hydro-isostatic adjustment on a rotating planet. However, they do not incorporate the effects of ocean warming and thermal expansion (*387*). (**A**) Cryogenian paleogeography (*419*) assumes maximum (*165*, *239*) rather than fractional (*100*) ice-sheet volume at the termination. Scale bars are in meters relative to sea level. (**B**) Net base-level changes computed over the 2-ky deglaciation phase. Negative change is base-level fall. Scale bar is in meters. (**C**) Net base-level changes computed over the 10-ky interval following the end of deglaciation. The scale bar is in meters. Note the time dependency of base-level changes and their sensitivity to location across the ocean-continent interface. Preterminal ice-sheet recession (*100*) changes the spatial distribution of ice-gravity and isostatic effects and reduces their amplitudes as well as that of eustasy.

Glacio-isostatic adjustment (GIA) results in the rise of surfaces formerly occupied by grounded ice sheets and subsidence of surfaces formerly raised as peripheral bulges or loaded by rising sea level (*419*). Subsidence of peripheral bulges causes water depths to continue increasing in those areas long after all the ice sheets have vanished (Fig. 27). Cap-carbonate sequences are typically found on ancient continental margins, areas that may have been occupied by peripheral bulges in late glacial times. Consequently, the TST (Fig. 24) of those sequences will not be limited to the deglaciation time scale but will continue for up to 6×10^4 years afterward (Fig. 27). This helps to reconcile rapid deglaciation with magnetostratigraphic constraints in such areas (*419*).

Ocean warming and thermal expansion cause the global mean sea level to continue rising after complete deglaciation. The time scale for whole-ocean warming is effectively the ocean mixing time, which ranges from 4×10^4 to 6×10^4 years (*387*), as noted above. Assuming, as before, a 2-km-deep brine at −4°C and a lid of the same depth at 15°C, the increase in the global mean sea level due to whole-ocean warming to a uniform 50°C is 40 to 50 m, depending on hypsometry (*387*). Although substantial, the estimated sea-level rise due to ocean warming is small when compared with the counteracting effect of GIA or "rebound," acting over the same time scale in areas that were loaded by grounded ice sheets when deglaciation began (*419*). Where ice sheets receded before terminal deglaciation (Fig. 10), the GIA response would be asynchronous with the cap-carbonate sequence but would still factor in the net base-level changes.

Deglaciation modeling (*387*, *419*) indicates that the time scale of marine transgression can be up to 20 to 30 times longer than the deglaciation time scale of ~2 ky. This constitutes an upper limit on the TST time scale at a given location, depending on when cap carbonate accumulation began at the site. The extended time scale (*387*, *419*) goes partway toward reconciliation with an actualistic interpretation of cap dolostone magnetostratigraphy (*428*–*431*). However, the GIA and ocean-warming time scales are still too fast by a factor of 4 or more to account for a full magnetic polarity reversal within ~0.5% (~4 cm) of the total stratigraphic thickness of the Marinoan cap dolostone in South Australia (*430*), assuming a constant sedimentation rate and a reversal duration of 2 to 10 ky, increasing with site latitude, as inferred from high-resolution sedimentary records of the most recent four reversals (*432*).

Recent experiments suggest that molten core electrical and thermal conductivities are significantly higher than previously thought (*458*–*462*). The data imply that core cooling is more rapid, and thus, inner-core inception is more recent (400 to 700 Ma) than has long been assumed (*433*–*435*). If the solid inner core were small or absent, the time scale for a 635-Ma geomagnetic reversal could be very much less than for recent reversals, assuming the reversal time scale is set by a diffusive process in the solid phase (*463*). Anomalous Ediacaran field behaviors (*464*–*466*) are possible manifestations of low-intensity fields and/or a small or absent inner core. Before inner-core inception, the geodynamo inferred from pre-Neoproterozoic paleomagnetic data must have been driven by a process other than the release of latent heat by inner-core growth (*467*). A smaller Cryogenian inner core offers a potential route to full reconciliation of the postglacial marine transgression and magnetic-reversal time scales in Marinoan cap dolostones.

How and why are Sturtian and Marinoan cap carbonates distinct?

Sturtian and Marinoan cap carbonates have basic features in common —sharp basal contacts, overthickened depositional sequences, and C isotope excursions to mantle-like values. However, they also have systematic differences (*130*, *131*, *468*). Most Marinoan examples begin with a cap dolostone (Fig. 24), a highly oxidized unit with sedimentary features indicating wave action (normal and reverse-graded peloids, low-angle swaley cross-lamination, and giant wave ripples) and phototrophy (tubestone- and gutter-type stromatolites). The area-weighted, median and average thicknesses of 29 Marinoan cap dolostones on 15 paleocontinents are 9 and 18 m, respectively (*131*, *156*), and the thickest sections (up to 200 m) accumulated closest to the paleoequator (*31*, *469*). They constitute part or all of relatively expanded TSTs (Fig. 24), and tubestone stromatolite may also occupy the HST in some cases (*470*). No fossil has been recovered from a Marinoan cap dolostone, although Zn and Cd isotopic evidence suggests that biological export production ramped up during the Marinoan TST in South Australia (*471*, *472*). Sedimentary barite ($BaSO_4$) occurs widely in Marinoan

cap dolostones (Fig. 4A), as void-filling cement in tepee-type breccias (*161*, *162*) or as singular, regional-scale horizons of seafloor cement (Fig. 6F) (*91*, *155*, *409*, *453*). Other seafloor cements, originally composed of aragonite crystal fans (Fig. 25H), are locally a major constituent of the deeper-water limestone micrites overlying Marinoan cap dolostones (*97*, *416*, *420*–*422*, *473*). The cements appear to be localized by seafloor topography (*97*). It is conceivable that incipient aragonite crystal fans precipitated on the shallow seafloor of the underlying cap dolostone precursor but were dispersed by wave action and accreted onto peloids, subsequently dolomitized. No sedimentary barite or former aragonite cement has ever been described from an undisputed Sturtian cap-carbonate sequences.

Most Sturtian cap carbonates begin with comparatively deeper-water facies—typically gray-colored, organic-rich, micritic limestone with basal hummocky cross-stratification as the shallowest-water bedforms (Figs. 19D and 25A) (*60*, *130*, *143*, *474*). Carbonate content may decrease upward, but where shallow-water bedforms are absent, it is uncertain whether the loss of carbonate is a function of water depth or secular change. In carbonate-dominated areas like western Mongolia (*143*) and northern Namibia (*144*), the Sturtian cap-carbonate sequence is essentially an HST, with the MF at or near the base and the TST absent or highly condensed. Likewise, the C isotope negative excursion is highly condensed and commonly base-truncated, the descending $\delta^{13}C$ branch missing altogether (*65*, *130*, *143*, *475*). Locally, however, as in the Arkaroola Wilderness Sanctuary in the Northern Flinders Ranges of South Australia, a 4.5-m-thick Sturtian cap dolostone (basal Tapley Hill Formation) composed of size-sorted peloids (*476*) with low-angle cross-bedding (Fig. 19C) is better developed than the Marinoan cap dolostone (Nuccaleena Formation) in the same area. In western Mongolia, northern Namibia, and Zambia, a variety of agglutinated testate microfossils have been recovered from Sturtian cap carbonates and tentatively identified with different clades of unicellular eukaryotic heterotrophs (*310*–*313*, *477*). In Namibia, they are hosted in the lower HST by a bizarre succession of likely nonphototrophic stromatolites and microbialaminites (Fig. 25C) with neptunian dikes and early void-filling cements (*442*, *475*, *478*, *479*). Sturtian and Marinoan cap carbonates are distinct and distinctive.

The condensed or missing TST in most Sturtian cap-carbonate sequences may be accounted for in different ways. First, Sturtian ice sheets may have receded, and global average sea level may have risen before the tropical sea-glacier collapsed (*93*). In this case, the TST would be synglacial, and sea-glacier collapse would occur at a highstand. The cap-carbonate sequence would follow the sudden backstepping of grounded sea-glacier ice, with an attendant shower of ice-rafted debris. The potential for base-level rise would be limited to whole-ocean warming, because coastal forebulges would have already collapsed. Second, surface waters (the meltwater lid) may have failed to reach critical oversaturation until after the glacioeustatic rise was complete. This would account for the basally truncated isotopic records of Sturtian compared with Marinoan cap-carbonate sequences (*130*, *143*, *475*, *480*–*483*). The occurrence of locally well-developed Sturtian TSTs (Fig. 19C) could relate to local sources of alkalinity during marine inundation of glacierized landscapes. However, delayed saturation does not explain why the TSTs are not expressed by siliciclastic sediments, in the absence of carbonate. Third, Sturtian continental margins, particularly the newly rifted margins of inner Rodinia (Fig. 5) where Cryogenian strata are common, simply subsided more deeply because of the greater longevity of the Sturtian cryochron (Fig. 2A). TSTs would then be missing or condensed in many areas because the mixed layer never touched bottom, even at the lowstand. Truncation of isotopic records would follow from initial undersaturation of bottom waters due to water depth. In this explanation, well-developed TSTs should have formed farther inland, where net subsidence was less. There, they would have been more susceptible to subsequent removal by erosion. Hence, they exist (Fig. 19C) but are uncommon. The third explanation predicts that Sturtian TSTs occur preferentially where subsidence rate was low and/or synglacial accumulation was high.

CONCLUSIONS AND GEOLOGICAL IMPLICATIONS

The recent development of a radiometric chronology has transformed the debate over Cryogenian glaciation. Each of the two glaciations was long-lived and terminated synchronously on multiple paleocontinents, satisfying key predictions of the Snowball Earth hypothesis. The occurrence of two such episodes in close temporal proximity argues against chance causes. Existing theory did not predict their gross inequality in duration, nor was the brevity of the nonglacial interlude between them anticipated by geologists. Now, more than ever, there is a pressing need for tighter age constraints on the onset of the younger Cryogenian (Marinoan) glaciation.

Cryogenian paleogeography was dominated by the long-lived supercontinent Rodinia and its tropical breakup. Atmospheric CO_2 was consequently lowered through enhanced silicate weathering and organic burial. The onset of the first Cryogenian (Sturtian) glaciation ended a 1.5-Gy nonglacial interval and coincided with the emplacement of a basaltic LIP across the paleoequator on a windward continental margin, ideally situated for intense chemical weathering. The igneous rocks were erupted through a sedimentary basin rich in sulfate evaporites, possibly leading to stratospheric injection of radiatively active sulfate aerosol by thermal plumes associated with long-lived fissure eruptions. A cold ambient climate would have lowered the height of the equatorial tropopause, making the stratosphere more accessible to plumes in the zone of maximum insolation.

The cold dry troposphere and the small thermal inertia of the frozen surface make a Snowball climate unlike any with tropical surface water. The Hadley circulation is vigorous but reversed in the annual mean, giving rise to subtropical snow belts and an equatorial sublimative desert. Seasonality is strong at all latitudes. Ice sheets thicken and flow, and although ice fluxes are relatively low, their erosive and depositional effects are cumulative over tens of millions of years. Because of the reflective surface, clouds and aerosols have net warming effects that allow a Snowball Earth to spontaneously deglaciate at high atmospheric CO_2 concentration.

In a coupled atmosphere–ice-sheet model, the mass balance of Snowball ice sheets becomes sensitive to precession-like orbital forcing as CO_2 accumulates. This is consistent with multiple advance-retreat cycles of ice fronts and grounding lines recorded in Cryogenian sedimentary deposits. Model ice sheets flow faster as CO_2 rises, but their collective mass diminishes over time, particularly in the lowest latitudes. Ice-free land surfaces are ever-present, and their concentration in the zone of summer surface winds promotes a strong dust flux. Secular warming and ice-sheet recession during a Snowball episode produce a "sawtooth" pattern that is opposite to that of Quaternary ice ages, which have ice maxima and are coldest at terminations.

Once the tropical ocean freezes over, sea ice thickens rapidly and, after a few 10^4 years, flows equatorward gravitationally, sustained in dynamic steady state by freezing and melting at the base and by sublimation, snowfall, and frost deposition at the top. Terrestrial dust and

volcanic ash are entrained in the floating "sea glacier" and accumulate at the sublimative surface of the equatorial zone. At first, the sublimative surface is too cold for dust retention, except perhaps in low-albedo coastal embayments. Elsewhere, dust is recycled back into the firn by winds. As atmospheric CO_2 rises, ice surfaces warm and dust is retained, forming meltwater-filled "cryoconite" (dark ice-dust) holes and ponds over the sublimation zone area of 6×10^7 km^2 (0.12 of global surface area). Modern cryoconite ecosystems are populated by cyanobacteria (~10 wt % by weight of cryoconite is organic matter of cyanobacterial origin), green algae, fungi, protists, and certain metazoa (rotifers, nematodes, and tardigrades). These freshwater oligotrophic ecosystems expanded greatly during Snowball glaciations. Molecular clocks suggest that major clades of modern marine planktonic cyanobacteria, including N_2 fixers and non–N_2-fixing picocyanobacteria, radiated from freshwater ancestors around this time, and sterane biomarkers record that green algae became the dominant eukaryotic primary producers following Cryogenian glaciation.

Dust flux estimates imply accumulation rates in the sublimation zone of 6 to 60 m My^{-1}, rapidly saturating the surface with cryoconite. On modern ice shelves, cryoconite is episodically flushed into the subglacial ocean through moulins, in response to excess meltwater production. Meltwater flushing cleanses the ice surface and increases its albedo, creating a stabilizing feedback ("dust thermostat") that allows the sea glacier and cryoconite ecosystems to coexist until CO_2 reaches a high concentration. Cryoconite flushing allows organic matter to be buried on the seafloor, generating atmospheric oxygen. It is also a process by which subaerially erupted volcanic ash may be advected through the ice cover onto the seafloor, suggesting that the search for dateable ash horizons within Cryogenian glacial sequences should focus on paleolatitudes ≤20°.

Cryoconite flushed into the subglacial ocean is subject to ocean currents. Despite the absence of wind-driven mixing, the subglacial ocean is turbulent and well mixed. Unlike an open ocean, it is heated only at the base, by the geothermal flux, preferentially at MORs. It loses heat at the top by diffusion through the ice, preferentially at the poles. Intense vertical mixing is concentrated close to the equator, and zonal jets reverse in direction with depth and also across the equator when geothermal input is asymmetric. Rows of secondary zonal jets stretch well away from the equator. The primary jets should direct the movement of cryoconite in the ocean and govern its deposition as sediment "drift." Upwellings or downwellings occur at continental margins where jets are directed seaward or landward, respectively, and both the jets and upwellings exhibit strong time-dependent behavior, the latter forming cavities in the warm basal ice. The result is a Snowball Earth ocean that is nearly isothermal, isohaline, well mixed, and weakly stratified.

The only economic-grade sedimentary Fe(±Mn) formations younger than 1.8 Ga are intimately associated with Sturtian glaciomarine deposits. They are not associated with ocean upwellings or glacial terminations but typically occur with ice-proximal deposits in semirestricted rift basins or fjords. Redox proxy data and Fe isotopes suggest deposition where ferruginous brine mixes with oxygenated meltwater at a persistent redoxcline. Silled basins may be favored for iron formation because point-source meltwater injections at the grounding lines of outlet glaciers are less rapidly dissipated than in the turbulent Snowball open ocean.

"Cap carbonates" are unique in scale and distribution to Cryogenian glacial terminations. They indicate an extraordinary degree of carbonate oversaturation in the mixed layer and thermocline. Rapid deglaciation and warming result in a stable density stratification, in which a cold, geochemically evolved brine is trapped beneath a 1- to 2-km-deep meltwater lid. The time scale for destratification is tentatively estimated as 10 to 100 ky, but the stratigraphic expression of ocean destratification is a key issue for future work. Whole-ocean mixing and warming cause the global mean sea level to rise by 40 to 60 m on a time scale that greatly exceeds the estimated 2 ky for ice-sheet meltdown and glacioeustatic rise. However, it remains far short of reconciling cap carbonate accumulation rates with an actualistic duration of paleomagnetic polarity reversals. Faster reversals due to a low-intensity field or a small inner core are still called for.

Snowball Earth is a fully dynamic planet, on which the atmosphere and ocean dynamics are profoundly influenced by the presence of the intervening ice sheet. Its sedimentary record is widespread, accessible, and well preserved in many areas. In the 6 years since the last reviews of Neoproterozoic climate dynamics (*115*, *116*), remarkable progress has been made in elucidating the circumstances surrounding the Cryogenian glaciations, the conditions that allowed the Snowball states to self-terminate, and the processes that produced the glacier-related deposits. Much remains to be learned from modeling, from field and laboratory observations, and from their mutual interaction. The increasingly multidisciplinary nature of research on Cryogenian glaciation (Fig. 28) is a welcome and essential development. It is inconceivable that events of the magnitude and duration indicated would have left no mark on the evolution of life. Their imprint is starting to be found in the fossil biomarker record and in the phylogenomics of living organisms. It is a sobering realization that a world that had not experienced an evident ice age for over 1.5 Gy should suddenly have been locked in ice for 58 My.

In the past decade, no new development was more consequential or unanticipated than the astounding Cryogenian time scale, which was forged by protégés of S. A. Bowring from U-Pb isotope systematics of that tiny fraction of ancient volcanic aerosols composed of the accessory mineral zircon ($ZrSiO_4$), complemented by isochron ages from hydrogenous Re and Os concentrated in sedimentary organic matter.

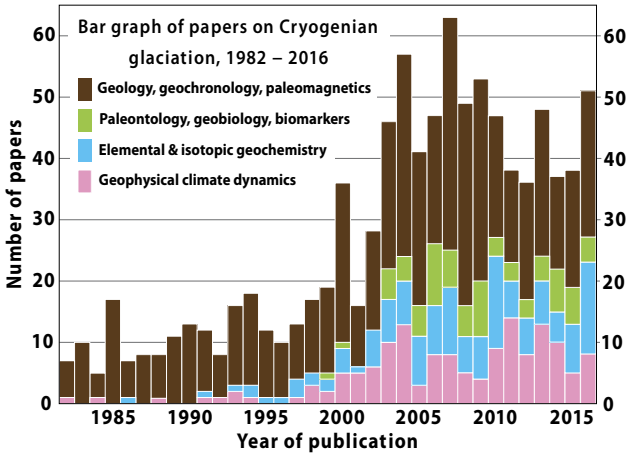

Fig. 28. Bar graph of peer-reviewed papers on Cryogenian glaciation by discipline and year, 1982 to 2016. Papers are assigned to one of four disciplinary categories. Note the relative growth of geophysical and geochemical papers after 1996 and geobiological papers after 2002. From the 1870s through the 1980s, research on "eo-Cambrian" glaciation was almost exclusively geological (*55*). The 70 chapters by various authors in the work of Arnaud *et al.* (*175*) are not tallied here. Forward modeling papers (in all categories) account for only ~25% of the current total.

REFERENCES AND NOTES

1. M. I. Budyko, On the origin of the glacial epochs. *Meteorol. Hydrol.* **11**, 3–12 (1968).
2. E. Eriksson, Air-ocean-icecap interactions in relation to climatic fluctuations and glaciation cycles. *Meteorol. Monogr.* **8**, 68–92 (1968).
3. M. I. Budyko, The effect of solar radiation variations on the climate of the Earth. *Tellus* **21**, 611–619 (1969).
4. W. D. Sellers, A global climatic model based on the energy balance of the Earth–atmosphere system. *J. Appl. Meteorol.* **8**, 392–400 (1969).
5. I. M. Held, M. J. Suarez, Simple albedo feedback models of the icecaps. *Tellus* **26**, 613–629 (1974).
6. R. T. Weatherald, S. Manabe, The effects of changing the Solar constant on the climate of a general circulation model. *J. Atmos. Sci.* **32**, 2044–2059 (1975).
7. M. Ghil, Climate stability for a Sellers-type model. *J. Atmos. Sci.* **33**, 3–20 (1976).
8. G. R. North, R. F. Cahalan, J. A. Coakley Jr., Energy balance climate models. *Rev. Geophys. Space Phys.* **19**, 91–121 (1981).
9. J. Bendtsen, Climate sensitivity to changes in solar insolation in a simple coupled climate model. *Clim. Dyn.* **18**, 595–609 (2002).
10. Y. Donnadieu, G. Ramstein, F. Fluteau, D. Roche, The impact of atmospheric and oceanic heat transports on the sea-ice-albedo instability during the Neoproterozoic. *Clim. Dyn.* **22**, 293–306 (2004).
11. C. J. Poulsen, R. L. Jacob, Factors that inhibit snowball Earth simulation. *Paleoceanography* **19**, PA4021 (2004).
12. P. H. Stone, M. S. Yao, The ice-covered Earth instability in a model of intermediate complexity. *Clim. Dyn.* **22**, 815–822 (2004).
13. M. Ishiwatari, K. Nakajima, S. Takehiro, Y.-Y. Hayashi, Dependence of climate states of gray atmosphere on solar constant: From the runaway greenhouse to the snowball states. *J. Geophys. Res.* **112**, D13120 (2007).
14. J. Marotzke, M. Botzet, Present-day and ice-covered equilibrium states in a comprehensive climate model. *Geophys. Res. Lett.* **34**, L16704 (2007).
15. G. H. Roe, M. B. Baker, Notes on a catastrophe: A feedback analysis of snowball earth. *J. Clim.* **23**, 4694–4703 (2010).
16. A. Voigt, J. Marotzke, The transition from the present-day climate to a modern Snowball Earth. *Clim. Dyn.* **35**, 887–905 (2010).
17. D. Ferreira, J. Marshall, B. Rose, Climate determinism revisited: Multiple equilibria in a complex climate model. *J. Clim.* **24**, 992–1012 (2011).
18. A. Voigt, D. S. Abbot, R. T. Pierrehumbert, J. Marotzke, Initiation of a Marinoan Snowball Earth in a state-of-the-art atmosphere-ocean general circulation model. *Clim. Past* **7**, 249–263 (2011).
19. J. Yang, W. R. Peltier, Y. Hu, The initiation of modern soft and hard Snowball Earth climates in CCSM4. *Clim. Past* **8**, 907–918 (2012).
20. A. Voigt, D. S. Abbot, Sea-ice dynamics strongly promote Snowball Earth initiation and destabilize tropical sea-ice margins. *Clim. Past* **8**, 2079–2092 (2012).
21. B. E. J. Rose, D. Ferreira, J. Marshall, The role of oceans and sea ice in abrupt transitions between multiple climate states. *J. Clim.* **26**, 2862–2879 (2013).
22. K. Menou, Climate stability of habitable Earth-like planets. *Earth Planet. Sci. Lett.* **429**, 20–24 (2015).
23. T. C. Spiegl, H. Paeth, H. E. Frimmel, Evaluating key parameters for the initiation of a Neoproterozoic Snowball Earth with a single Earth System Model of intermediate complexity. *Earth Planet. Sci. Lett.* **415**, 100–110 (2015).
24. J. L. Kirschvink, Late Proterozoic low-latitude global glaciation: The Snowball Earth, in *The Proterozoic Biosphere: A Multidisciplinary Study*, J. W. Schopf, C. Klein, D. Des Maris, Eds. (Cambridge Univ. Press, 1992), pp. 51–52.
25. W. B. Harland, Evidence of Late Precambrian glaciation and its significance, in *Problems in Palaeoclimatology*, A. E. M. Nairn, Ed. (Interscience, 1964), pp. 119–149.
26. B. J. J. Embleton, G. E. Williams, Low palaeolatitude of deposition for late Precambrian periglacial varvites in South Australia: Implications for palaeoclimatology. *Earth Planet. Sci. Lett.* **79**, 419–430 (1986).
27. P. F. Hoffman, A. J. Kaufman, G. P. Halverson, D. P. Schrag, A Neoproterozoic Snowball Earth. *Science* **281**, 1342–1346 (1998).
28. D. A. D. Evans, Stratigraphic, geochronological, and paleomagnetic constraints upon the Neoproterozoic climatic paradox. *Am. J. Sci.* **300**, 347–433 (2000).
29. P. F. Hoffman, D. P. Schrag, The snowball Earth hypothesis: Testing the limits of global change. *Terra Nova* **14**, 129–155 (2002).
30. I. J. Fairchild, M. J. Kennedy, Neoproterozoic glaciation in the Earth System. *J. Geol. Soc. London* **164**, 895–921 (2007).
31. P. F. Hoffman, Z.-X. Li, A palaeogeographic context for Neoproterozoic glaciation. *Palaeogeogr. Palaeoclimatol. Palaeoecol.* **277**, 158–172 (2009).
32. F. A. Macdonald, M. D. Schmitz, J. L. Crowley, C. F. Roots, D. S. Jones, A. C. Maloof, J. V. Strauss, P. A. Cohen, D. T. Johnston, D. P. Schrag, Calibrating the Cryogenian. *Science* **327**, 1241–1243 (2010).
33. D. A. D. Evans, T. D. Raub, Neoproterozoic glacial palaeolatitudes: A global update, in *The Geological Record of Neoproterozoic Glaciations*, E. Arnaud, G. P. Halverson, G. Shields-Zhou, Eds. (Geological Society of London, 2011), pp. 93–112.
34. Z.-X. Li, D. A. D. Evans, G. P. Halverson, Neoproterozoic glaciations in a revised global palaeogeography from the breakup of Rodinia to the assembly of Gondwanaland. *Sediment. Geol.* **294**, 219–232 (2013).
35. D. A. Evans, N. J. Beukes, J. L. Kirschvink, Low-latitude glaciation in the Palaeoproterozoic era. *Nature* **386**, 262–266 (1997).
36. J. L. Kirschvink, E. J. Gaidos, L. E. Bertani, N. J. Beukes, J. Gutsmer, L. N. Maepa, R. E. Steinberger, Paleoproterozoic snowball Earth: Extreme climatic and geochemical global change and its biological consequences. *Proc. Natl. Acad. Sci. U.S.A.* **97**, 1400–1405 (2000).
37. I. N. Bindeman, A. K. Schmitt, D. A. D. Evans, Limits of hydrosphere-lithosphere interaction: Origin of the lowest-known $\delta^{18}O$ silicate rock on Earth in the Paleoproterozoic Karelian rift. *Geology* **38**, 631–634 (2010).
38. I. N. Bindeman, N. S. Serebryakov, Geology, petrology and O and H isotope geochemistry of remarkably ^{18}O depleted Paleoproterozoic rocks of the Belamorian Belt, Karelia, Russia, attributed to global glaciation 2.4 Ga. *Earth Planet. Sci. Lett.* **306**, 163–174 (2011).
39. I. N. Bindeman, N. S. Serebryakov, A. K. Schmitt, J. A. Vazquez, Y. Guan, P. Y. Azimov, B. Y. Astafiev, J. Palandri, L. Dobrzhinskaya, Field and microanalytical isotopic investigation of ultradepleted in ^{18}O Paleoproterozoic "Slushball Earth" rocks from Karelia, Russia. *Geosphere* **10**, 308–339 (2014).
40. D. Herwartz, A. Pack, D. Krylov, Y. Xiao, K. Muehlenbachs, S. Sengupta, T. Di Rocco, Revealing the climate of snowball Earth from $\Delta^{17}O$ systematics of hydrothermal rocks. *Proc. Natl. Acad. Sci. U.S.A.* **112**, 5337–5341 (2015).
41. J. M. Moore, H. Tsikos, S. Polteau, Deconstructing the Transvaal Supergroup, South Africa: Implications for Palaeoproterozoic palaeoclimate models. *J. Afr. Earth Sci.* **33**, 437–444 (2001).
42. P. F. Hoffman, The Great Oxidation and a Siderian snowball Earth: MIF-S based correlation of Paleoproterozoic glacial epochs. *Chem. Geol.* **362**, 143–156 (2013).
43. G. Luo, S. Ono, N. J. Beukes, D. T. Wang, S. Xie, R. E. Summons, Rapid oxygenation of Earth's atmosphere 2.33 billion years ago. *Sci. Adv.* **2**, e1600134 (2016).
44. A. P. Gumsley, K. R. Chamberlain, W. Bleeker, U. Söderlund, M. O. de Kock, E. R. Larsson, A. Bekker, Timing and tempo of the Great Oxidation Event. *Proc. Natl. Acad. Sci. U.S.A.* **114**, 1811–1816 (2017).
45. D. O. Zakharov, I. N. Bindeman, A. I. Slabunov, M. Ovtcharova, M. A. Coble, N. S. Serebryakov, U. Schaltegger, Dating the Paleoproterozoic snowball Earth glaciations using contemporaneous subglacial hydrothermal systems. *Geology* **45**, 667–670 (2017).
46. G. D. Love, E. Grosjean, C. Stalvies, D. A. Fike, J. P. Grotzinger, A. S. Bradley, A. E. Kelly, M. Bhatia, W. Meredith, C. E. Snape, S. A. Bowring, D. J. Condon, R. E. Summons, Fossil steroids record the appearance of *Demospongiae* during the Cryogenian period. *Nature* **457**, 718–721 (2009).
47. D. H. Erwin, M. Laflamme, S. M. Tweedt, E. A. Sperling, D. Pisani, K. J. Peterson, The Cambrian conundrum: Early divergence and later ecological success in the early history of animals. *Science* **334**, 1091–1097 (2011).
48. G. D. Love, R. E. Summons, The molecular record of Cryogenian sponges—A response to Antcliffe (2013). *Palaeontology* **58**, 1131–1136 (2015).
49. J. J. Brocks, A. J. M. Jarrett, E. Sirantoine, F. Kenig, M. Moczydłowska, S. Porter, J. Hope, Early sponges and toxic protists: Possible sources of cryostane, an age diagnostic biomarker antedating the Sturtian Snowball Earth. *Geobiology* **14**, 129–149 (2016).
50. G. A. Shields-Zhou, S. Porter, G. P. Halverson, A new rock-based definition for the Cryogenian Period (circa 720–635 Ma). *Episodes* **39**, 3–8 (2016).
51. B. J. Cooper, 'Snowball Earth': The early contribution from South Australia. *Earth Sci. Hist.* **29**, 121–145 (2010).
52. D. Mawson, R. C. Sprigg, Subdivision of the Adelaide System. *Aust. J. Sci.* **13**, 69–72 (1950).
53. G. M. Narbonne, S. Xiao, G. A. Shields, J. G. Gehling, The Ediacaran Period, in *The Geologic Time Scale*, F. M. Gradstein, J. G. Ogg, M. D. Schmitz, G. M. Ogg, Eds. (Elsevier, 2012), pp. 413–435.
54. H. W. Ahlmann, O. H. Kulling, Scientific results of the Swedish-Norwegian Arctic Expedition in the summer of 1931. *Geogr. Ann. Stockholm* **16**, 161–253 (1934).
55. P. F. Hoffman, A history of Neoproterozoic glacial geology, 1871–1997, in *The Geological Record of Neoproterozoic Glaciations*, E. Arnaud, G. P. Halverson, G. Shields-Zhou, Eds. (Geological Society of London, Memoirs 36, 2011), pp. 17–37.
56. K.-H. Hoffmann, D. J. Condon, S. A. Bowring, J. L. Crowley, U-Pb zircon date from the Neoproterozoic Ghaub Formation, Namibia: Constraints on Marinoan glaciation. *Geology* **32**, 817–820 (2004).
57. D. Condon, M. Zhu, S. A. Bowring, W. Wang, A. Yang, Y. Jin, U-Pb ages from the Neoproterozoic Doushantuo Formation, China. *Science* **308**, 95–98 (2005).
58. S. Zhang, G. Jiang, Y. Han, The age of the Nantuo Formation and Nantuo glaciation in South China. *Terra Nova* **20**, 289–294 (2008).
59. C. R. Calver, J. L. Crowley, M. T. D. Wingate, D. A. D. Evans, T. D. Raub, M. D. Schmitz, Globally synchronous Marinoan deglaciation indicated by U-Pb geochronology of the Cottons Breccia, Tasmania, Australia. *Geology* **41**, 1127–1130 (2013).

60. A. D. Rooney, F. A. Macdonald, J. V. Strauss, F. Dudás, C. Hallmann, D. Selby, Re-Os geochronology and coupled Os-Sr isotope constraints on the Sturtian snowball Earth. *Proc. Natl. Acad. Sci. U.S.A.* **111**, 51–56 (2014).
61. G. M. Cox, J. V. Strauss, G. P. Halverson, M. D. Schmitz, W. C. McClelland, R. S. Stevenson, F. A. Macdonald, Kikiktat volcanics of Arctic Alaska—Melting of harzburgitic mantle associated with the Franklin large igneous province. *Lithosphere* **7**, 275–295 (2015).
62. P. Liu, X. Li, S. Chen, Z. Lan, B. Yang, X. Shang, C. Yin, New SIMS U–Pb zircon age and its constraint on the beginning of the Nantuo glaciation. *Sci. Bull.* **60**, 958–963 (2015).
63. A. D. Rooney, J. V. Strauss, A. D. Brandon, F. A. Macdonald, A Cryogenian chronology: Two long-lasting synchronous Neoproterozoic glaciations. *Geology* **43**, 459–462 (2015).
64. G. Song, X. Wang, X. Shi, G. Jiang, New U-Pb age constraints on the upper Banxi Group and synchrony of the Sturtian glaciation in South China. *Geosci. Front.* **8**, 1161–1173 (2017).
65. W. Yu, T. J. Algeo, Y. Du, Q. Zhou, P. Wang, Y. Xu, L. Yuan, W. Pan, Newly discovered Sturtian cap carbonate in the Nanhua Basin, South China. *Precambrian Res.* **293**, 112–130 (2017).
66. P. R. Dunn, B. P. Thomson, K. Rankama, Late Pre-Cambrian glaciation in Australia as a stratigraphic boundary. *Nature* **231**, 498–502 (1971).
67. A. R. Crawford, B. Daily, Probable non-synchroneity of Late Precambrian glaciations. *Nature* **230**, 111–112 (1971).
68. N. Eyles, N. Januszczak, 'Zipper-rift': A tectonic model for Neoproterozoic glaciations during the breakup of Rodinia after 750 Ma. *Earth Sci. Rev.* **65**, 1–73 (2004).
69. J. C. G. Walker, P. B. Hays, J. F. Kasting, A negative feedback mechanism for the long-term stabilization of Earth's surface temperature. *J. Geophys. Res.* **86**, 9776–9782 (1981).
70. M. Turbet, F. Forget, J. Leconte, B. Charnay, G. Tobie, CO_2 condensation is a serious limit to the deglaciation of Earth-like planets. arXiv:1703.04624v1 [astro-ph.EP] (2017).
71. F. Forget, R. T. Pierrehumbert, Warming early Mars with carbon dioxide clouds that scatter infrared radiation. *Science* **278**, 1273–1276 (1997).
72. D. Kitzmann, Revisiting the scattering greenhouse effect of CO_2 ice clouds. *Astrophys. J. Lett.* **817**, L18 (2016).
73. G. Le Hir, G. Ramstein, Y. Donnadieu, Y. Goddéris, Scenario for the evolution of atmospheric pCO_2 during a snowball Earth. *Geology* **36**, 47–50 (2008).
74. G. Le Hir, Y. Goddéris, Y. Donnadieu, G. Ramstein, A geochemical modelling study of the evolution of the chemical composition of seawater linked to a "snowball" glaciation. *Biogeosciences* **5**, 253–267 (2008).
75. T. M. Gernon, T. K. Hincks, T. Tyrrell, E. J. Rohling, M. R. Palmer, Snowball Earth ocean chemistry driven by extensive ridge volcanism during Rodinia breakup. *Nat. Geosci.* **9**, 242–248 (2016).
76. S. R. Gislason, E. H. Oelkers, Mechanism, rates, and consequences of basaltic glass dissolution: II. An experimental study of the dissolution rates of basaltic glass as a function of pH and temperature. *Geochim. Cosmochim. Acta* **67**, 3817–3832 (2003).
77. D. S. Abbot, I. Halevy, Dust aerosol important for Snowball Earth deglaciation. *J. Clim.* **23**, 4121–4132 (2010).
78. D. S. Abbot, R. T. Pierrehumbert, Mudball: Surface dust and Snowball Earth deglaciation. *J. Geophys. Res.* **115**, D03104 (2010).
79. G. Le Hir, Y. Donnadieu, G. Krinner, G. Ramstein, Toward the snowball earth deglaciation. *Clim. Dyn.* **35**, 285–297 (2010).
80. D. S. Abbot, A. Voigt, M. Branson, R. T. Pierrehumbert, D. Pollard, G. Le Hir, D. D. B. Koll, Clouds and snowball Earth deglaciation. *Geophys. Res. Lett.* **39**, L20711 (2012).
81. D. S. Abbot, A. Voigt, D. Li, G. Le Hir, R. T. Pierrehumbert, M. Branson, D. Pollard, D. D. B. Koll, Robust elements of Snowball Earth atmospheric circulation and oases for life. *J. Geophys. Res. Atmos.* **118**, 6017–6027 (2013).
82. D. S. Abbot, Resolved snowball Earth clouds. *J. Clim.* **27**, 4391–4402 (2014).
83. A. R. Prave, D. J. Condon, K. H. Hoffmann, S. Tapster, A. E. Fallick, Duration and nature of the end-Cryogenian (Marinoan) glaciation. *Geology* **44**, 631–634 (2016).
84. J. A. Higgins, D. P. Schrag, Aftermath of a snowball Earth. *Geochem. Geophys. Geosyst.* **4**, 1028 (2003).
85. H.-M. Bao, J. R. Lyons, C. Zhou, Triple oxygen isotope evidence for elevated CO_2 levels after a Neoproterozoic glaciation. *Nature* **453**, 504–506 (2008).
86. H. Bao, I. J. Fairchild, P. M. Wynn, C. Spötl, Stretching the envelope of past surface environments: Neoproterozoic glacial lakes from Svalbard. *Science* **323**, 119–122 (2009).
87. S. A. Kasemann, A. R. Prave, A. E. Fallick, C. J. Hawkesworth, K.-H. Hoffmann, Neoproterozoic ice ages, boron isotopes, and ocean acidification: Implications for a snowball Earth. *Geology* **38**, 775–778 (2010).
88. X. Cao, H. Bao, Dynamic model constraints on oxygen-17 depletion in atmospheric O_2 after a snowball Earth. *Proc. Natl. Acad. Sci. U.S.A.* **110**, 14546–14550 (2013).
89. S. A. Kasemann, P. A. E. Pogge von Strandmann, A. R. Prave, A. E. Fallick, T. Elliott, K.-H. Hoffmann, Continental weathering following a Cryogenian glaciation: Evidence from calcium and magnesium isotopes. *Earth Planet. Sci. Lett.* **396**, 66–77 (2014).
90. F. Ohnemueller, A. R. Prave, A. E. Fallick, S. A. Kasemann, Ocean acidification in the aftermath of the Marinoan glaciation. *Geology* **42**, 1103–1106 (2014).
91. P. W. Crockford, B. R. Cowie, D. T. Johnston, P. F. Hoffman, I. Sugiyama, A. Pellerin, T. H. Bui, J. Hayles, G. P. Halverson, F. A. Macdonald, B. A. Wing, Triple oxygen and multiple sulfur isotope constraints on the evolution of the post-Marinoan sulfur cycle. *Earth Planet. Sci. Lett.* **435**, 74–83 (2016).
92. A. M. Spencer, *Late Pre-Cambrian Glaciation in Scotland* (Geological Society of London, Memoirs 6, 1971).
93. M. B. Edwards, *Sedimentology of the Upper Proterozoic Glacial Record, Vestertana Group, Finnmark, North Norway* (Geological Survey of Norway, Bulletin 394, 1984).
94. M. Deynoux, Terrestrial or waterlain glacial diamictites? Three case studies from the late Proterozoic and late Ordovician glacial drifts in West Africa. *Palaeogeogr. Palaeoclimatol. Palaeoecol.* **51**, 97–141 (1985).
95. P. Kellerhals, A. Matter, Facies analysis of a glaciomarine sequence, the Neoproterozoic Mirbat Sandstone Formation, Sultanate of Oman. *Eclogae Geol. Helv.* **96**, 49–70 (2003).
96. E. W. Domack, P. F. Hoffman, An ice grounding-line wedge from the Ghaub glaciation (635 Ma) on the distal foreslope of the Otavi carbonate platform, Namibia, and its bearing on the Snowball Earth hypothesis. *Geol. Soc. Am. Bull.* **123**, 1448–1477 (2011).
97. P. F. Hoffman, Strange bedfellows: Glacial diamictite and cap carbonate from the Marinoan (635 Ma) glaciation in Namibia. *Sedimentology* **58**, 57–119 (2011).
98. A. H. N. Rice, M. B. Edwards, T. A. Hansen, *Neoproterozoic Glacial and Associated Facies in the Tanafjord–Varangerfjord Area, Finnmark, North Norway* (Geological Society of America, Field Guide 26, 2012).
99. C. V. Rose, A. C. Maloof, B. Schoene, R. C. Ewing, U. Linnemann, M. Hofmann, J. M. Cottle, The end-Cryogenian glaciation of South Australia. *Geosci. Can.* **40**, 256–293 (2013).
100. D. I. Benn, G. Le Hir, H. Bao, Y. Donnadieu, C. Dumas, E. J. Fleming, M. J. Hambrey, E. A. Mcmillan, M. S. Petronis, G. Ramstein, C. T. E. Stevenson, P. M. Wynn, I. J. Fairchild, Orbitally forced ice sheet fluctuations during the Marinoan Snowball Earth glaciation. *Nat. Geosci.* **8**, 704–708 (2015).
101. I. J. Fairchild, E. J. Fleming, H. Bao, D. I. Benn, I. Boomer, Y. V. Dubliansky, G. P. Halverson, M. J. Hambrey, C. Hendy, E. A. Mcmillan, C. Spötl, C. T. E. Stevenson, P. M. Wynn, Continental carbonate facies of a Neoproterozoic panglaciation, north-east Svalbard. *Sedimentology* **63**, 443–497 (2016).
102. E. J. Fleming, D. I. Benn, C. T. E. Stevenson, M. S. Petronis, M. J. Hambrey, I. J. Fairchild, Glacitectonism, subglacial and glacilacustrine processes during a Neoproterozoic panglaciation, north-east Svalbard. *Sedimentology* **63**, 411–442 (2016).
103. P. A. Cohen, F. A. Macdonald, The Proterozoic record of eukaryotes. *Paleobiology* **41**, 610–632 (2015).
104. H. J. Hofmann, G. M. Narbonne, J. D. Aitken, Ediacaran remains from intertillite beds in northwestern Canada. *Geology* **18**, 1199–1202 (1990).
105. A. C. Maloof, C. V. Rose, R. Beach, B. M. Samuels, C. C. Calmet, D. H. Erwin, G. R. Poirier, N. Yao, F. J. Simons, Possible animal-body fossils in pre-Marinoan limestones from South Australia. *Nat. Geosci.* **3**, 653–659 (2010).
106. P. A. Cohen, F. A. Macdonald, S. Pruss, E. Matys, T. Bosak, Fossils of putative marine algae from the Cryogenian glacial interlude of Mongolia. *Palaios* **30**, 238–247 (2015).
107. Q. Ye, J. Tong, S. Xiao, S. Zhu, Z. An, L. Tian, J. Hu, The survival of benthic macroscopic phototrophs on a Neoproterozoic snowball Earth. *Geology* **43**, 507–510 (2015).
108. M. dos Reis, Y. Thawornwattana. K. Angelis, M. J. Telford, P. C. J. Donoghue, Z. Wang, Uncertainty in the timing of origin of animals and the limits of precision in molecular timescales. *Curr. Biol.* **25**, 2939–2950 (2015).
109. F. A. Macdonald, A. R. Prave, R. Petterson, E. F. Smith, S. B. Pruss, K. Oates, F. Wachter, D. Trotzuk, A. E. Fallick, The Laurentian record of Neoproterozoic glaciation, tectonism, and eukaryotic evolution in Death Valley, California. *Geol. Soc. Am. Bull.* **125**, 1203–1223 (2013).
110. A. H. Knoll, *Life on a Young Planet: The First Three Billion Years of Evolution on Earth* (Princeton Univ. Press, 2003).
111. A. N. Olcott, A. L. Sessions, F. A. Corsetti, A. J. Kaufman, T. F. de Oliviera, Biomarker evidence for photosynthesis during Neoproterozoic glaciation. *Science* **310**, 471–474 (2005).
112. F. A. Corsetti, A. N. Olcott, C. Bakermans, The biotic response to Neoproterozoic snowball Earth. *Palaeogeogr. Palaeoclimatol. Palaeoecol.* **232**, 114–130 (2006).
113. P. A. Allen, J. L. Etienne, Sedimentary challenge to Snowball Earth. *Nat. Geosci.* **1**, 817–825 (2008).
114. M. Moczydłowska, The Ediacaran microbiota and the survival of Snowball Earth conditions. *Precambrian Res.* **167**, 1–15 (2008).
115. Y. Goddéris, G. Le Hir, Y. Donnadieu, Modelling the Snowball Earth, in *The Geological Record of Neoproterozoic Glaciations*, E. Arnaud, G. P. Halverson, G. Shields-Zhou, Eds. (Geological Society of London, Memoirs 36, 2011), pp. 151–161.
116. R. T. Pierrehumbert, D. S. Abbot, A. Voigt, D. Koll, Climate of the Neoproterozoic. *Annu. Rev. Earth Planet. Sci.* **39**, 417–460 (2011).
117. F. Corfu, A century of U-Pb geochronology: The long quest towards concordance. *Geol. Soc. Am. Bull.* **125**, 33–47 (2013).
118. J. M. Mattinson, Revolution and evolution: 100 years of U-Pb geochronology. *Elements* **9**, 53–57 (2013).

119. M. D. Schmitz, K. F. Kulper, High-precision geochronology. *Elements* **9**, 25–30 (2013).
120. N. M. McLean, J. F. Bowring, S. A. Bowring, An algorithm for U-Pb isotope dilution data reduction and uncertainty propagation. *Geochem. Geophys. Geosyst.* **12**, Q0AA18 (2011).
121. B. Schoene, D. J. Condon, L. Morgan, N. McLean, Precision and accuracy in geochronology. *Elements* **9**, 19–24 (2013).
122. J. M. Mattinson, Extending the Krogh legacy: Development of the CA-TIMS method for zircon U-Pb geochronology. *Can. J. Earth Sci.* **48**, 95–105 (2011).
123. G. Ravizza, K. K. Turekian, Application of the ^{187}Re-^{187}Os system to black shale geochronology. *Geochim. Cosmochim. Acta* **53**, 3257–3262 (1989).
124. R. A. Creaser, P. Sannigrahi, T. Chacko, D. Selby, Further evaluation of the Re-Os geochronometer in organic-rich sedimentary rocks: A test of hydrocarbon maturation effects in the Exshaw formation, Western Canada Sedimentary Basin. *Geochim. Cosmochim. Acta* **66**, 3441–3452 (2002).
125. D. Selby, R. A. Creaser, Direct radiometric dating of the Devonian-Mississippian time-scale boundary using the Re-Os black shale geochronometer. *Geology* **33**, 545–548 (2005).
126. D. Selby, R. A. Creaser, Re–Os geochronology of organic rich sediments: An evaluation of organic matter analysis methods. *Chem. Geol.* **200**, 225–240 (2003).
127. S. W. Denyszyn, H. C. Halls, D. W. Davis, D. A. D. Evans, Paleomagnetism and U-Pb geochronology of Franklin dykes in High Arctic Canada and Greenland: A revised age and paleomagnetic pole constraining block rotations in the Nares Strait region. *Can. J. Earth Sci.* **46**, 689–705 (2009).
128. R. E. Ernst, M. A. Hamilton, U. Söderlund, J. A. Hanes, D. P. Gladkochub, A. V. Okrugin, T. Kolotolina, A. S. Mekhonoshin, W. Bleeker, A. N. LeCheminant, K. L. Buchan, K. R. Chamberlain, A. N. Didenko, Long-lived connection between southern Siberia and northern Laurentia in the Proterozoic. *Nat. Geosci.* **9**, 464–469 (2016).
129. R. E. Ernst, K. L. Buchan, Maximum size and distribution in time and space of mantle plumes: Evidence from large igneous provinces. *J. Geodyn.* **34**, 309–342 (2002).
130. M. J. Kennedy, B. Runnegar, A. R. Prave, K.-H. Hoffmann, M. A. Arthur, Two or four Neoproterozoic glaciations? *Geology* **26**, 1059–1063 (1998).
131. P. F. Hoffman, F. A. Macdonald, G. P. Halverson, Chemical sediments associated with Neoproterozoic glaciation: Iron formation, cap carbonate, barite and phosphorite, in *The Geological Record of Neoproterozoic Glaciations*, E. Arnaud, G. P. Halverson, G. Shields-Zhou, Eds. (Geological Society of London, 2011), pp. 67–80.
132. D. P. Le Heron, M. E. Busfield, F. Kamona, An interglacial on snowball Earth? Dynamic ice behaviour revealed in the Chuos Formation, Namibia. *Sedimentology* **60**, 411–427 (2013).
133. W. A. Yonkee, C. D. Dehler, P. K. Link, E. A. Balgord, J. A. Keeley, D. S. Hayes, M. L. Wells, C. M. Fanning, S. M. Johnston, Tectono-stratigraphic framework of Neoproterozoic to Cambrian strata, west-central U.S.: Protracted rifting, glaciation, and evolution of the North American Cordilleran margin. *Earth Sci. Rev.* **136**, 59–95 (2014).
134. Z. Lan, X.-H. Li, Q. Zhang, Q.-L. Li, Global synchronous initiation of the 2nd episode of Sturtian glaciation: SIMS zircon U-Pb and O isotope evidence from the Jiangkou Group, South China. *Precambrian Res.* **267**, 28–38 (2015).
135. G. H. Spence, D. P. Le Heron, I. J. Fairchild, Sedimentological perspectives on climatic, atmospheric and environmental change in the Neoproterozoic Era. *Sedimentology* **63**, 253–306 (2016).
136. D. P. Le Heron, The significance of ice-rafted debris in Sturtian glacial successions. *Sediment. Geol.* **322**, 19–33 (2015).
137. B. Kendall, R. A. Creaser, D. Selby, Re-Os geochronology of postglacial black shales in Australia: Constraints on the timing of "Sturtian" glaciation. *Geology* **34**, 729–732 (2006).
138. I. J. Fairchild, P. Bonnard, T. Davies, E. J. Fleming, N. Grassineau, G. P. Halverson, M. J. Hambrey, E. M. McMillan, E. McKay, I. J. Parkinson, C. T. E. Stevenson, The Late Cryogenian Warm Interval, NE Svalbard: Chemostratigraphy and genesis. *Precambrian Res.* **281**, 128–154 (2016).
139. M. J. Hambrey, A. A. Spencer, Late Precambrian glaciation of central East Greenland. *Medd. Groenl.* **19**, 1–50 (1987).
140. L.-J. Feng, X.-L. Chu, J. Huang, Q.-R. Zhang, H.-J. Chang, Reconstruction of paleo-redox conditions and early sulfur cycling during deposition of the Cryogenian Datangpo Formation in South China. *Gondwana Res.* **18**, 632–637 (2010).
141. C. Li, G. D. Love, T. W. Lyons, C. T. Scott, L. Feng, J. Huang, H. Chang, Q. Zhang, X. Chu, Evidence for a redox stratified Cryogenian marine basin, Datangpo Formation, South China. *Earth Planet. Sci. Lett.* **331–332**, 246–256 (2012).
142. F. Zhang, X. Zhu, B. Yan, B. Kendall, X. Peng, J. Li, T. J. Algeo, S. Romaniello, Oxygenation of a Cryogenian ocean (Nanhua Basin, South China) revealed by pyrite Fe isotope compositions. *Earth Planet. Sci. Lett.* **429**, 11–19 (2015).
143. U. Bold, E. F. Smith, A. D. Rooney, S. A. Bowring, R. Buchwaldt, F. Dudás, J. Ramezani, J. L. Crowley, D. P. Schrag, F. A. Macdonald, Neoproterozoic stratigraphy of the Zavkhan terrane of Mongolia: The backbone for Cryogenian and early Ediacaran chemostratigraphic records. *Am. J. Sci.* **316**, 1–63 (2016).
144. P. F. Hoffman, G. P. Halverson, *Otavi Group of the western Northern Platform, the Eastern Kaoko Zone and the western Northern Margin Zone*, vol. 2 of *The Geology of Namibia*, R. M. Miller, Ed. (Geological Survey of Namibia, 2008), pp. 13.69–13.136.
145. R. Rieu, P. A. Allen, Siliciclastic sedimentation in the interlude between two Neoproterozoic glaciations, Mirbat area, southern Oman: A missing link in the Huqf Supergroup? *GeoArabia* **13**, 45–72 (2008).
146. G. H. Eisbacher, Re-definition and subdivision of the Rapitan Group, Mackenzie Mountains. *Geol. Surv. Can. Pap.* **77-35**, 1–21 (1978).
147. G. H. Eisbacher, Sedimentary tectonics and glacial record in the Windermere Supergroup, Mackenzie Mountains, northwestern Canada. *Geol. Surv. Can. Pap.* **80-27**, 1–40 (1981).
148. G. M. Narbonne, J. D. Aitken, Neoproterozoic of the Mackenzie Mountains, northwestern Canada. *Precambrian Res.* **73**, 101–121 (1995).
149. E. S. Day, N. P. James, G. M. Narbonne, R. W. Dalrymple, A sedimentary prelude to Marinoan glaciation, Cryogenian (Middle Neoproterozoic) Keele Formation, Mackenzie Mountains, northwestern Canada. *Precambrian Res.* **133**, 223–247 (2004).
150. W. V. Preiss, *The Adelaide Geosycnline: Late Proterozoic Stratigraphy, Sedimentation, Palaeontology and Tectonics* (Geological Survey of South Australia, 1987).
151. D. M. McKirdy, J. M. Burgess, N. M. Lemon, X. Yu, A. M. Cooper, V. A. Gostin, R. J. F. Jenkins, R. A. Both, A chemostratigraphic overview of the late Cryogenian interglacial sequence in the Adelaide Fold-Thrust Belt, South Australia. *Precambrian Res.* **106**, 149–186 (2001).
152. T. A. Fromhold, M. W. Wallace, Regional recognition of the Neoproterozoic Sturtian–Marinoan boundary, northern and central Adelaide Geosyncline, South Australia. *Aust. J. Earth Sci.* **59**, 527–546 (2012).
153. C. V. Rose, N. L. Swanson-Hysell, J. M. Husson, L. N. Poppick, J. M. Cottle, B. Schoene, A. C. Maloof, Constraints on the origin and relative timing of the Trezona δ^{13}C anomaly below the end-Cryogenian glaciation. *Earth Planet. Sci. Lett.* **319–320**, 241–250 (2012).
154. G. A. Shields, Neoproterozoic cap carbonates: A critical appraisal of existing models and the *plumeworld* hypothesis. *Terra Nova* **17**, 299–310 (2005).
155. M. J. Kennedy, Stratigraphy, sedimentology, and isotopic geochemistry of Australian Neoproterozoic postglacial cap dolostones: Deglaciation, δ^{13}C excursions, and carbonate precipitation. *J. Sediment. Res.* **66**, 1050–1064 (1996).
156. P. F. Hoffman, G. P. Halverson, E. W. Domack, J. M. Husson, J. A. Higgins, D. P. Schrag, Are basal Ediacaran (635 Ma) post-glacial "cap dolostones" diachronous? *Earth Planet. Sci. Lett.* **258**, 114–131 (2007).
157. G. P. Halverson, P. F. Hoffman, D. P. Schrag, A. J. Kaufman, A major perturbation of the carbon cycle before the Ghaub glaciation (Neoproterozoic) in Namibia: Prelude to snowball Earth? *Geochem. Geophys. Geosyst.* **3**, 1–24 (2002).
158. N. L. Swanson-Hysell, C. V. Rose, C. C. Calmet, G. P. Halverson, M. T. Hurtgen, A. C. Maloof, Cryogenian glaciation and the onset of carbon-isotope decoupling. *Science* **328**, 608–611 (2010).
159. F. A. Macdonald, J. V. Strauss, C. V. Rose, F. Dudás, D. P. Schrag, Stratigraphy of the Port Nolloth Group of Namibia and South Africa and implications for the age of Neoproterozoic iron formations. *Am. J. Sci.* **310**, 862–888 (2010).
160. G. M. Cox, G. P. Halverson, A. Poirier, D. Le Heron, J. V. Strauss, R. Stevenson, A model for Cryogenian iron formation. *Earth Planet. Sci. Lett.* **433**, 280–292 (2016).
161. G. A. Shields, M. Deynoux, H. Strauss, H. Paquet, D. Nahon, Barite-bearing cap dolostone of the Taoudéni Basin, northwest Africa: Sedimentary and isotope evidence for methane seepage after a Neoproterozoic glaciation. *Precambrian Res.* **153**, 209–235 (2007).
162. Y. Peng, H. Bao, C. Zhou, X. Yuan, ^{17}O-depleted barite from two Marinoan cap dolostone sections, South China. *Earth Planet. Sci. Lett.* **305**, 21–31 (2011).
163. B. A. Wing, A cold, hard look at ancient oxygen. *Proc. Natl. Acad. Sci. U.S.A.* **110**, 14514–14515 (2013).
164. B. Mills, A. J. Watson, C. Goldblatt, R. Boyle, T. M. Lenton, Timing of Neoproterozoic glaciations linked to transport-limited global weathering. *Nat. Geosci.* **4**, 861–864 (2011).
165. Y. Donnadieu, F. Fluteau, G. Ramstein, C. Ritz, J. Besse, Is there a conflict between the Neoproterozoic glacial deposits and the snowball Earth interpretation: An improved understanding with numerical modeling. *Earth Planet. Sci. Lett.* **208**, 101–112 (2003).
166. C. B. Rodehacke, A. Voigt, F. Ziemen, D. S. Abbot, An open ocean region in Neoproterozoic glaciations would have to be narrow to allow equatorial ice sheets. *Geophys. Res. Lett.* **40**, 5503–5507 (2013).
167. D. Li, R. T. Pierrehumbert, Sea glacier flow and dust transport on Snowball Earth. *Geophys. Res. Lett.* **38**, L17501 (2011).
168. J. C. Goodman, D. C. Strom, Feedbacks in a coupled ice-atmosphere-dust model of the glacial Neoproterozoic "Mudball Earth." *J. Geophys. Res.* **118**, 11546–11557 (2013).
169. C. A. Partin, P. M. Sadler, Slow net sediment accumulation sets Snowball Earth apart from younger glacial episodes. *Geology* **44**, 1019–1022 (2016).
170. B. Hallet, L. Hunter, J. Bogen, Rates of erosion and sediment evacuation by glaciers: A review of field data and their implications. *Global Planet. Change* **12**, 213–235 (1996).
171. S. P. Anderson, Biogeochemistry of glacial landscape systems. *Annu. Rev. Earth Planet. Sci.* **35**, 375–399 (2007).

172. P. V. Brady, S. R. Gislason, Seafloor weathering controls on atmospheric CO_2 and global climate. *Geochim. Cosmochim. Acta* **61**, 965–973 (1997).
173. L. A. Coogan, K. M. Gillis, Evidence that low-temperature oceanic hydrothermal systems play an important role in the silicate-carbonate weathering cycle and long-term climate regulation. *Geochem. Geophys. Geosyst.* **14**, 1771–1786 (2013).
174. G. M. Cox, G. P. Halverson, R. K. Stevenson, M. Vokaty, A. Poirier, M. Kunzmann, Z.-X. Li, S. W. Denyszyn, J. V. Strauss, F. A. Macdonald, Continental flood basalt weathering as a trigger for Neoproterozoic Snowball Earth. *Earth Planet. Sci. Lett.* **446**, 89–99 (2016).
175. E. Arnaud, G. P. Halverson, G. Shields-Zhou, *The Geological Record of Neoproterozoic Ice Ages* (Geological Society of London, 2011).
176. I. J. Fairchild, Balmy shores and icy wastes: The paradox of carbonates associated with glacial deposits in Neoproterozoic times, in *Sedimentology Review 1*, V. P. Wright, Ed. (Blackwell, 1993), pp. 1–16.
177. B. N. Opdyke, B. H. Wilkinson, Paleolatitude distribution of Phanerozoic marine ooids and cements. *Palaeogeogr. Palaeoclimatol. Palaeoecol.* **78**, 135–148 (1990).
178. B. N. Opdyke, B. H. Wilkinson, Carbonate mineral saturation state and cratonic limestone accumulation. *Am. J. Sci.* **293**, 217–234 (1993).
179. Z. X. Li, S. V. Bogdanova, A. S. Collins, A. Davidson, B. De Waele, R. E. Ernst, I. C. W. Fitzsimons, R. A. Fuck, D. P. Gladkochub, J. Jacobs, K. E. Karlstrom, S. Lu, L. M. Natapov, V. Pease, S. A. Pisarevsky, K. Thrane, V. Vernikovsky, Assembly, configuration, and break-up history of Rodinia: A synthesis. *Precambrian Res.* **160**, 179–210 (2008).
180. D. A. D. Evans, Reconstructing pre-Pangean supercontinents. *Geol. Soc. Am. Bull.* **125**, 1735–1751 (2013).
181. D. A. D. Evans, The palaeomagnetically viable, long-lived and all-inclusive Rodinia supercontinent reconstruction, in *Ancient Orogens and Modern Analogues*, J. B. Murphy, J. D. Keppie, A. J. Hynes, Eds. (Geological Society of London, 2009), pp. 371–404.
182. E. J. Barron, S. L. Thompson, W. W. Hay, Continental distribution as a forcing factor for global-scale temperature. *Nature* **310**, 574–575 (1984).
183. C. J. Poulsen, R. L. Jacob, R. T. Pierrehumbert, T. T. Huynh, Testing paleogeographic controls on a Neoproterozoic "snowball Earth." *Geophys. Res. Lett.* **29**, 10-1–10-4 (2002).
184. R. P. Fiorella, C. J. Poulsen, Dehumidification over tropical continents reduces climate sensitivity and inhibits snowball Earth initiation. *J. Clim.* **26**, 9677–9695 (2013).
185. H. G. Marshall, J. C. G. Walker, W. R. Kuhn, Long-term climate change and the geochemical cycle of carbon. *J. Geophys. Res.* **93**, 791–801 (1988).
186. Y. Donnadieu, Y. Goddéris, G. Ramstein, A. Nédélec, J. Meert, A 'snowball Earth' climate triggered by continental break-up through changes in runoff. *Nature* **428**, 303–306 (2004).
187. Y. Donnadieu, Y. Goddéris, R. Pierrehumbert, G. Dromart, F. Fluteau, R. Jacob, A GEOCLIM simulation of climatic and biogeochemical consequences of Pangea breakup. *Geochem. Geophys. Geosyst.* **7**, Q11019 (2006).
188. A. H. Knoll, End of the Proterozoic Eon. *Sci. Am.* **265**, 64–73 (1991).
189. J. I. Hedges, R. G. Keil, Sedimentary organic matter preservation: An assessment and speculative synthesis. *Mar. Chem.* **49**, 81–115 (1995).
190. D. P. Schrag, R. A. Berner, P. F. Hoffman, G. P. Halverson, On the initiation of a snowball Earth. *Geochem. Geophys. Geosyst.* **3**, 1–21 (2002).
191. R. E. Ernst, M. T. D. Wingate, K. L. Buchan, Z. X. Li, Global record of 1600–700 Ma Large Igneous Provinces (LIPs): Implications for the reconstruction of the proposed Nuna (Columbia) and Rodinia supercontinents. *Precambrian Res.* **160**, 159–178 (2008).
192. C. Dessert, B. Dupré, L. M. François, J. Schott, J. Gaillardet, G. Chakrapani, S. Bajpai, Erosion of Deccan Traps determined by river geochemistry: Impact on the global climate and the $^{87}Sr/^{86}Sr$ ratio of seawater. *Earth Planet. Sci. Lett.* **188**, 459–474 (2001).
193. J. Hartmann, N. Moosdorf, R. Lauerwald, M. Hinderer, A. J. West, Global chemical weathering and associated P-release—The role of lithology, temperature and soil properties. *Chem. Geol.* **363**, 145–163 (2014).
194. A. D. Jacobson, M. G. Andrews, G. O. Lehn, C. Holmden, Silicate versus carbonate weathering in Iceland: New insights from Ca isotopes. *Earth Planet. Sci. Lett.* **416**, 132–142 (2015).
195. G. Li, J. Hartmann, L. A. Derry, A. J. West, C. You, X. Long, T. Zhan, L. Li, G. Li, W. Qiu, T. Li, L. Liu, Y. Chen, J. Ji, L. Zhao, J. Chen, Temperature dependence of basalt weathering. *Earth Planet. Sci. Lett.* **443**, 59–69 (2016).
196. F. Horton, Did phosphorus derived from the weathering of large igneous provinces fertilize the Neoproterozoic ocean? *Geochem. Geophys. Geosyst.* **16**, 1723–1738 (2015).
197. Y. Goddéris, G. Le Hir, M. Macouin, Y. Donnadieu, L. Hubert-Théou, G. Dera, M. Aretz, F. Fluteau, Z. X. Li, G. P. Halverson, Paleogeographic forcing of the strontium isotopic cycle in the Neoproterozoic. *Gondwana Res.* **42**, 151–162 (2017).
198. G. A. Shields, B. J. W. Mills, Tectonic controls on the long-term carbon isotope mass balance. *Proc. Natl. Acad. Sci. U.S.A.* **114**, 4318–4323 (2017).
199. Y. Goddéris, Y. Donnadieu, A. Nédélec, B. Dupré, C. Dessert, A. Grard, G. Ramstein, L. M. François, The Sturtian 'snowball' glaciation: Fire and ice. *Earth Planet. Sci. Lett.* **211**, 1–12 (2003).
200. F. A. Macdonald, R. Wordsworth, Initiation of Snowball Earth with volcanic sulfur aerosol emissions. *Geophys. Res. Lett.* **44**, 1938–1946 (2017).
201. L. S. Glaze, S. Self, A. Schmidt, S. J. Hunter, Assessing eruption column height in ancient flood basalt eruptions. *Earth Planet. Sci. Lett.* **457**, 263–270 (2017).
202. S. Self, A. Schmidt, T. A. Mather, Emplacement characteristics, time scales, and volcanic gas release rates of continental flood basalt eruptions on Earth, in *Volcanism, Impacts, and Mass Extinctions: Causes and Effects*, G. Keller, A. C. Kerr, Eds. (Geological Society of America, Special Paper 505, 2014), pp. 319–337.
203. J. H. Bédard, B. Hayes, M. Hryciuk, C. Beard, N. Williamson, T. A. Dell'Oro, R. H. Rainbird, J. Prince, W. R. A. Baragar, P. I. Nabelek, D. Weis, B. Wing, J. Scoates, H. R. Naslund, B. Cousens, M.-C. Williamson, L. J. Hulbert, R. Montjoie, É. Girard, R. Ernst, C. J. Lissenberg, *Geochemical Database of Franklin Sills, Natkusiak Basalts and Shaler Supergroup Rocks, Victoria Island, Northwest Territories, and Correlatives from Nunavut and the Mainland* (Geological Survey of Canada, Open File 8009, 2016).
204. D. Thomson, R. H. Rainbird, B. Krapez, Sequence and tectonostratigraphy of the Neoproterozoic (Tonian-Cryogenian) Amundsen Basin prior to supercontinent (Rodinia) breakup. *Precambrian Res.* **263**, 246–259 (2015).
205. J. Thomson, On the geology of the island of Islay. *Trans. Geol. Soc. Glasgow* **5**, 200–222 (1877).
206. H. Reusch, *Skuringmærker og morængrus eftervist i Finnmarken fra en periode meget ældre end 'istiden'* [Glacial striae and boulder-clay in Norwegian Lapponie from a period much older than the last ice age]. *Norges Geol. Unders.* **1**, 78–85 (1891).
207. D. B. Dow, Evidence of a late Pre-Cambrian glaciation in the Kimberley Region of Western Australia. *Geol. Mag.* **102**, 407–414 (1965).
208. C. A. L. Isotta, A. C. Rocha-Campos, R. Yoshida, Striated pavement of the upper Pre-Cambrian glaciation in Brazil. *Nature* **222**, 466–468 (1969).
209. W. Howchin, Glacial beds of Cambrian age in South Australia. *Quart. J. Geol. Soc. London* **64**, 234–259 (1908).
210. M. B. Edwards, Late Precambrian glacial loessites from north Norway and Svalbard. *J. Sediment. Petrol.* **49**, 85–91 (1979).
211. N. Christie-Blick, Neoproterozoic sedimentation and tectonics in west-central Utah. *BYU Geol. Stud.* **42**, 1–30 (1997).
212. R. Rieu, P. A. Allen, J. L. Étienne, A. Cozzi, U. Wiechert, A Neoproterozoic glacially influenced basin margin succession and 'atypical' cap carbonate associated with bedrock paleovalleys, Mirbat area, southern Oman. *Basin Res.* **18**, 471–496 (2006).
213. P. F. Hoffman, K. G. Lamothe, S. J. C. LoBianco, M. S. W. Hodgskiss, E. J. Bellefroid, B. W. Johnson, E. B. Hodgin, G. P. Halverson, Sedimentary depocenters on Snowball Earth: Case studies from the Sturtian Chuos Formation in northern Namibia. *Geosphere* **13**, 811–837 (2017)
214. D. I. Benn, A. R. Prave, Subglacial and proglacial glacitectonic deformation in the Neoproterozoic Port Askaig Formation, Scotland. *Geomorphology* **75**, 266–280 (2006).
215. M. Bestmann, A. H. N. Rice, F. Langenhorst, B. Grasemann, F. Heidelbach, Subglacial bedrock welding associated with glacial earthquakes. *J. Geol. Soc. London* **163**, 417–420 (2006).
216. J. C. Goodman, R. T. Pierrehumbert, Glacial flow of floating marine ice in "Snowball Earth." *J. Geophys. Res.* **108**, 3308 (2003).
217. P. F. Hoffman, D. P. Schrag, Response: Considering a Neoproterozoic snowball Earth. *Science* **284**, 1087 (1999).
218. D. P. Le Heron, M. E. Busfield, A. R. Prave, Neoproterozoic ice sheets and olistoliths: Multiple glacial cycles in the Kingston Peak Formation, California. *J. Geol. Soc. London* **171**, 525–538 (2014).
219. P. K. Link, V. A. Gostin, Facies and paleography of Sturtian glacial strata (Late Precambrian), South Australia. *Am. J. Sci.* **281**, 353–374 (1981).
220. G. H. Eisbacher, Late Proterozoic rifting, glacial sedimentation, and sedimentary cycles in the light of Windermere deposition, western Canada. *Palaeogeogr. Palaeoclimatol. Palaeoecol.* **51**, 231–254 (1985).
221. N. Christie-Blick, L. E. Sohl, M. J. Kennedy, Considering a Neoproterozoic snowball Earth. *Science* **284**, 1087 (1999).
222. P. F. Hoffman, On Cryogenian (Neoproterozoic) ice-sheet dynamics and the limitations of the glacial sedimentary record. *South Afr. J. Geol.* **108**, 557–577 (2005).
223. E. Rignot, J. Mouginot, B. Scheuchl, Ice flow of the Antarctic Ice Sheet. *Science* **333**, 1427–1430 (2011).
224. S. G. Warren, R. E. Brandt, T. C. Grenfell, C. P. McKay, Snowball Earth: Ice thickness on the tropical ocean. *J. Geophys. Res.* **107**, 31-1–31-18 (2002).
225. R. Dadic, P. C. Mullen, M. Schneebeli, R. E. Brandt, S. G. Warren, Effects of bubbles, cracks, and volcanic tephra on the spectral albedo of bare ice near the Transantarctic Mountains: Implications for sea glaciers on Snowball Earth. *J. Geophys. Res.* **118**, 1658–1676 (2013).
226. J. C. G. Walker, Strange weather on snowball Earth, in *Earth Systems Processes–Global Meeting* (Geological Society of America, Session No. T5, 2001).
227. R. T. Pierrehumbert, High levels of atmospheric carbon dioxide necessary for the termination of global glaciation. *Nature* **429**, 646–649 (2004).
228. R. T. Pierrehumbert, Climate dynamics of a hard snowball Earth. *J. Geophys. Res.* **110**, D01111 (2005).

229. A. Voigt, The dynamics of the Snowball Earth Hadley circulation for off-equatorial and seasonally varying insolation. *Earth Syst. Dynam.* **4**, 425–438 (2013).
230. G. E. Williams, D. G. Tonkin, Periglacial structures and paleoclimatic significance of a late Precambrian block field in the Cattle Grid copper mine, Mount Gunson, South Australia. *Aust. J. Earth Sci.* **32**, 287–300 (1985).
231. G. E. Williams, Proterozoic (pre-Ediacaran) glaciation and the high obliquity, low-latitude ice, strong seasonality (HOLIST) hypothesis: Principles and tests. *Earth Sci. Rev.* **87**, 61–93 (2008).
232. R. C. Ewing, I. Eisenman, M. P. Lamb, L. Poppick, A. C. Maloof, W. W. Fischer, New constraint on equatorial temperatures during a Late Neoproterozoic snowball Earth glaciation. *Earth Planet. Sci. Lett.* **406**, 110–122 (2014).
233. G. E. Williams, P. W. Schmidt, G. M. Young, Strongly seasonal Proterozoic climate in low palaeolatitudes: Radically different climate system on the pre-Ediacaran Earth. *Geosci. Front.* **7**, 555–571 (2016).
234. S. Manabe, R. T. Wetherald, Thermal equilibrium of the atmosphere with a given distribution of relative humidity. *J. Atmos. Sci.* **24**, 241–259 (1967).
235. A. Voigt, I. M. Held, J. Marotzke, Hadley cell dynamics in a virtually dry snowball Earth atmosphere. *J. Atmos. Sci.* **69**, 116–128 (2012).
236. D. S. Abbot, A. Voigt, D. Koll, The Jormungand global climate state and implications for Neoproterozoic glaciations. *J. Geophys. Res.* **116**, D18103 (2011).
237. B. E. J. Rose, Stable "Waterbelt" climates controlled by tropical ocean heat transport: A nonlinear coupled climate mechanism of relevance to Snowball Earth. *J. Geophys. Res.* **120**, 1404–1423 (2015).
238. C. Leovy, Weather and climate on Mars. *Nature* **412**, 245–249 (2001).
239. D. Pollard, J. F. Kasting, Climate-ice sheet simulations of Neoproterozoic glaciation before and after collapse to Snowball Earth, in *The Extreme Proterozoic: Geology, Geochemistry, and Climate*, G. S. Jenkins, M. A. S. McMenamin, C. P. McKay, L. Sohl, Eds. (American Geophysical Union, 2004), pp. 91–105.
240. P. M. Sadler, Sediment accumulation rates and the completeness of stratigraphic sections. *J. Geol.* **89**, 569–584 (1981).
241. P. M. Sadler, The influence of hiatuses on sediment accumulation rates, vol. 5 of *GeoResearch Forum*, P. Bruns, H. C. Haas, Eds. (Trans Tech Publications, 1999), pp. 15–40.
242. P. M. Sadler, D. J. Jerolmack, Scaling laws for aggradation, denudation and progradation rates: The case for time-scale invariance at sediment sources and sinks, in *Strata and Time: Probing the Gaps in Our Understanding*, D. G. Smith, R. J. Bailey, P. M. Burgess, A. J. Fraser, Eds. (Geological Society of London, 2014).
243. A. R. Lewis, D. R. Marchant, A. C. Ashworth, L. Hedenäs, S. R. Hemming, J. V. Johnson, M. J. Leng, M. L. Machlus, A. E. Newton, J. I. Raine, J. K. Willenbring, M. Williams, A. P. Wolfe, Mid-Miocene cooling and the extinction of tundra in continental Antarctica. *Proc. Natl. Acad. Sci. U.S.A.* **105**, 10676–10680 (2008).
244. A. E. Shevenell, J. P. Kennett, D. W. Lea, Middle Miocene ice sheet dynamics, deep-sea temperatures, and carbon cycling: A Southern Ocean perspective. *Geochem. Geophys. Geosyst.* **9**, Q02006 (2008).
245. M. C. Rygel, C. R. Fielding, T. D. Frank, L. P. Birgenheier, The magnitude of Late Paleozoic glacioeustatic fluctuations: A synthesis. *J. Sediment. Res.* **78**, 500–511 (2008).
246. B. Dyer, A. C. Maloof, Physical and chemical stratigraphy suggest small or absent glacioeustatic variation during formation of the Paradox Basin cyclothems. *Earth Planet. Sci. Lett.* **419**, 63–70 (2015).
247. J. P. Pu, S. A. Bowring, J. Ramezani, P. Myrow, T. D. Raub, E. Landing, A. Mills, E. Hodgin, F. A. Macdonald, Dodging snowballs: Geochronology of the Gaskiers glaciation and the first appearance of the Ediacaran biota. *Geology* **44**, 955–958 (2016).
248. J. O. Hagen, Glacier surge in Svalbard with examples from Usherbreen. *Nor. Geogr. Tidsskr.* **42**, 203–213 (1988).
249. D. R. MacAyeal, Binge/purge oscillations of the Laurentide ice sheet as a cause of the North Atlantic's Heinrich events. *Paleoceanography* **8**, 775–784 (1993).
250. D. J. Condon, A. R. Prave, D. I. Benn, Neoproterozoic rain-out intervals: Observations and implications. *Geology* **30**, 35–38 (2002).
251. D. Pollard, R. M. DeConto, A coupled ice-sheet/ice-shelf/sediment model applied to a marine-margin flowline: Forced and unforced variations, in *Glacial Sedimentary Processes and Products*, M. Hambrey, P. Christofferson, N. Glasser, B. Hubbard, Eds. (Blackwell, 2007), pp. 37–52.
252. J. Leather, P. A. Allen, M. D. Brasier, A. Cozzi, Neoproterozoic snowball Earth under scrutiny: Evidence from the Fiq glaciation of Oman. *Geology* **30**, 891–894 (2002).
253. J. L. Etienne, P. A. Allen, R. Rieu, E. Le Guerroué, Neoproterozoic glaciated basins: A critical review of the 'Snowball Earth' hypothesis by comparison with Phanerozoic glaciations, in *Glacial Sedimentary Processes and Products*, M. Hambrey, P. Christofferson, N. Glasser, B. Hubbard, Eds. (Blackwell, 2007), pp. 343–399.
254. R. Rieu, P. A. Allen, M. Plötze, T. Pettke, Climatic cycles during a Neoproterozoic "snowball" glacial epoch. *Geology* **35**, 299–302 (2007).
255. M. E. Busfield, D. P. Le Heron, Sequencing the Sturtian icehouse: Dynamic ice behaviour in South Australia. *J. Geol. Soc. London* **171**, 443–456 (2014).
256. F. Hourdin, I. Musat, S. Bony, P. Braconnot, F. Codron, J.-L. Dufresne, L. Fairhead, M.-A. Filiberti, P. Friedlingstein, J.-Y. Grandpeix, G. Krinner, P. LeVan, Z.-X. Li, F. Lott, The LMDZ4 general circulation model: Climate performance and sensitivity to parametrized physics with emphasis on tropical convection. *Clim. Dyn.* **27**, 787–813 (2006).
257. C. Ritz, V. Rommelaere, C. Dumas, Modeling the evolution of Antarctic ice sheet over the last 420,000 years: Implications for altitude changes in the Vostok region. *J. Geophys. Res.* **106**, 31943–31964 (2001).
258. G. E. Williams, Late Neoproterozoic periglacial aeolian sand sheet, Stuart Shelf, South Australia. *Aust. J. Earth Sci.* **45**, 733–741 (1998).
259. J. R. O'Neil, Hydrogen and oxygen isotope fractionation between ice and water. *J. Phys. Chem.* **72**, 3683–3684 (1968).
260. T. Torii, S. Murata, N. Yamagata, Geochemistry of the Dry Valley lakes. *J. R. Soc. N. Z.* **11**, 387–399 (1981).
261. W. F. Vincent, *Microbial Ecosystems of Antarctica* (Cambridge Univ. Press, 1988).
262. P. B. Price, T. Sowers, Temperature dependence of metabolic rates for microbial growth, maintenance, and survival. *Proc. Natl. Acad. Sci. U.S.A.* **101**, 4631–4636 (2004).
263. R. E. Cameron, Farthest south algae and associated bacteria. *Phycologia* **11**, 133–139 (1972).
264. S. B. Pointing, Y. Chan, D. C. Lacap, M. C. Y. Lau, J. A. Jurgens, R. L. Farrell, Highly specialized microbial diversity in hyper-arid polar desert. *Proc. Natl. Acad. Sci. U.S.A.* **106**, 19964–19969 (2009).
265. J. C. Priscu, C. H. Fritsen, E. A. Adams, S. J. Giovannoni, H. W. Paerl, C. P. McKay, P. T. Doran, D. A. Gordon, B. D. Lanoil, J. L. Pinckney, Perennial Antarctic lake ice: An oasis for life in a polar desert. *Science* **280**, 2095–2098 (1998).
266. D. T. Andersen, D. Y. Sumner, I. Hawes, J. Webster-Brown, C. P. McKay, Discovery of large conical stromatolites in Lake Untersee, Antarctica. *Geobiology* **9**, 280–293 (2011).
267. A. E. Murray, F. Kenig, C. H. Fritsen, C. P. McKay, K. M. Cawley, R. Edwards, E. Kuhn, D. M. McKnight, N. E. Ostrom, V. Peng, A. Ponce, J. C. Priscu, V. Samarkin, A. T. Townsend, P. Waugh, S. A. Young, P. T. Yung, P. T. Doran, Microbial life at −13 °C in the brine of an ice-sealed Antarctic lake. *Proc. Natl. Acad. Sci. U.S.A.* **109**, 20626–20631 (2012).
268. D. R. Marchant, G. H. Denton, C. C. Swisher III, N. Potter Jr., Late Cenozoic Antarctic paleoclimate reconstructed from volcanic ashes in the Dry Valleys region of southern Victoria Land. *Geol. Soc. Am. Bull.* **108**, 181–194 (1996).
269. B. C. Parker, G. M. Simmons Jr., K. G. Seaburg, D. D. Cathey, F. C. T. Allnutt, Comparative ecology of plankton communities in seven Antarctic oasis lakes. *J. Plankton Res.* **4**, 271–286 (1982).
270. L. F. Stanish, J. R. Spears, Diatom ecology and microbial mat structure and function in Antarctic Dry Valleys. *Palaios* **28**, 267–269 (2013).
271. W. F. Vincent, J. Laybourn-Parry, *Polar Lakes and Rivers: Limnology of Arctic and Antarctic Aquatic Ecosystems* (Oxford Univ. Press, 2008).
272. W. F. Vincent, A. Quesada, Cyanobacteria in high latitude lakes, rivers and seas, in *Ecology of Cyanobacteria II: Their Diversity in Space and Time*, B. A. Whitton, Ed. (Springer, 2012), pp. 371–385.
273. R. W. Gerdel, F. Drouet, The cryoconite of the Thule area, Greenland. *Trans. Am. Microsc. Soc.* **79**, 256–272 (1960).
274. N. F. McIntyre, Cryoconite hole thermodynamics. *Can. J. Earth Sci.* **21**, 152–156 (1984).
275. R. A. Wharton Jr., C. P. McKay, G. M. Simmons Jr., B. C. Barker, Cryoconite holes on glaciers. *BioScience* **35**, 499–503 (1985).
276. N. Takeuchi, Optical characteristics of cryoconite (surface dust) on glaciers: The relationship between light absorbancy and the property of organic matter contained in the cryoconite. *Ann. Glaciol.* **34**, 409–414 (2002).
277. A. Hodson, K. Cameron, C. Bøggild, T. Irvine-Fynn, H. Langford, D. Pearce, S. Banwart, The structure, biological activity and biogeochemistry of cryoconite aggregates upon an Arctic valley glacier: Longyearbreen, Svalbard. *J. Glaciol.* **56**, 349–362 (2010).
278. E. A. Bagshaw, M. Tranter, A. G. Fountain, K. A. Welch, H. Basagic, W. B. Lyons, Biogeochemical evolution of cryoconite holes on Canada Glacier, Taylor Valley, Antarctica. *J. Geophys. Res.* **112**, G04S35 (2007).
279. A. G. Fountain, T. H. Nylen, M. Tranter, E. Bagshaw, Temporal variations in physical and chemical features of cryoconite holes on Canada Glacier, McMurdo Dry Valleys, Antarctica. *J. Geophys. Res.* **113**, G01S92 (2008).
280. N. A. M. Chrismas, A. M. Anesio, P. Sánchez-Baracaldo, Multiple adaptations to polar and alpine environments within cyanobacteria: A phylogenomic and Bayesian approach. *Front. Microbiol.* **6**, 1070 (2015).
281. N. A. M. Chrismas, G. Barker, A. M. Anesio, P. Sánchez-Baracaldo, Genomic mechanisms for cold tolerance and production of exopolysaccharides in the Arctic cyanobacterium *Phormidesmis priestleyi* BC1401. *BMC Genomics* **17**, 533 (2016).
282. B. C. Christner, B. H. Kvitko II, J. N. Reeve, Molecular identification of Bacteria and Eukarya inhabiting an Antarctic cryoconite hole. *Extremophiles* **7**, 177–183 (2003).
283. K. Zawierucha, M. Kolicka, N. Takeuchi, Ł. Kaczmarek, What animals can live in cryoconite holes? A faunal review. *J. Zool.* **295**, 159–169 (2015).

284. B. Light, R. E. Brandt, S. G. Warren, Hydrohalite in cold sea ice: Laboratory observations of single crystals, surface accumulations, and migration rates under a temperature gradient, with application to "Snowball Earth." *J. Geophys. Res.* **114**, C07018 (2009).
285. R. Dadic, B. Light, S. G. Warren, Migration of air bubbles in ice under a temperature gradient, with application to "Snowball Earth." *J. Geophys. Res.* **115**, D18125 (2010).
286. R. C. Carns, R. E. Brandt, S. G. Warren, Salt precipitation in sea ice and its effect on albedo, with application to Snowball Earth. *J. Geophys. Res. Oceans* **120**, 7400–7412 (2015).
287. B. Light, R. C. Carns, S. G. Warren, The spectral albedo of sea ice and salt crusts on the tropical ocean of Snowball Earth: 1. Laboratory measurements. *J. Geophys. Res. Oceans* **121**, 4966–4979 (2016).
288. R. C. Carns, B. Light, S. G. Warren, The spectral albedo of sea ice and salt crusts on the tropical ocean of Snowball Earth: 2. Optical modeling. *J. Geophys. Res. Oceans* **121**, 5217–5230 (2016).
289. E. Costas, A. Flores-Moya, V. López-Rodas, Rapid adaptation of phytoplankters to geothermal waters is achieved by single mutations: Were extreme environments 'Noah's Arks' for photosynthesizers during the Neoproterozoic 'snowball Earth'? *New Phytol.* **180**, 922–932 (2008).
290. A. J. Campbell, E. D. Waddington, S. G. Warren, Refugium for surface life on Snowball Earth in a nearly-enclosed sea? A first simple model for sea-glacier invasion. *Geophys. Res. Lett.* **38**, L19502 (2011).
291. E. Tziperman, D. S. Abbot, Y. Ashkenazy, H. Gildor, D. Pollard, C. G. Schoof, D. P. Schrag, Continental constriction and oceanic ice-cover thickness in a Snowball-Earth scenario. *J. Geophys. Res.* **117**, C05016 (2012).
292. A. J. Campbell, E. D. Waddington, S. G. Warren, Refugium for surface life on Snowball Earth in a nearly enclosed sea? A numerical solution for sea-glacier invasion through a narrow strait. *J. Geophys. Res. Oceans* **119**, 2679–2690 (2014).
293. W. F. Vincent, J. A. E. Gibson, R. Pienitz, V. Villeneuve, P. A. Broady, P. B. Hamilton, C. Howard-Williams, Ice shelf microbial ecosystems in the High Arctic and implications for life on snowball earth. *Naturwissenschaften* **87**, 137–141 (2000).
294. W. F. Vincent, D. R. Mueller, S. Bonilla, Ecosystems on ice: The microbial ecology of Markham Ice Shelf in the high Arctic. *Cryobiology* **48**, 103–112 (2004).
295. W. F. Vincent, D. Mueller, P. van Hove, C. Howard-Williams, in *Origins: Genesis, Evolution and Diversity of Life*, J. Seckbach, Ed. (Springer, 2004), pp. 483–501.
296. P. F. Hoffman, Cryoconite pans on Snowball Earth: Supraglacial oases for Cryogenian eukaryotes? *Geobiology* **14**, 531–542 (2016).
297. A. Tomitani, A. H. Knoll, C. M. Cavanaugh, T. Ohno, The evolutionary diversification of cyanobacteria: Molecular–phylogenetic and paleontological perspectives. *Proc. Natl. Acad. Sci. U.S.A.* **103**, 5442–5447 (2006).
298. N. J. Butterfield, Proterozoic photosynthesis—A critical review. *Palaeontology* **58**, 953–972 (2015).
299. P. M. Shih, J. Hemp, L. M. Ward, N. J. Matzke, W. W. Fischer, Crown group Oxyphotobacteria postdate the rise of oxygen. *Geobiology* **15**, 19–29 (2017).
300. R. M. Soo, J. Hemp, D. H. Parks, W. W. Fischer, P. Hugenholtz, On the origins of oxygenic photosynthesis and aerobic respiration in Cyanobacteria. *Science* **355**, 1436–1440 (2017).
301. A. H. Knoll, R. E. Summons, J. R. Waldbauer, J. E. Zumberge, The geological succession of primary producers in the oceans, in *Evolution of Primary Producers in the Sea*, P. G. Falkowski, A. H. Knoll, Eds. (Elsevier Academic, 2007), pp. 133–163.
302. N. J. Butterfield, A. H. Knoll, K. Swett, Paleobiology of the Neoproterozoic Svanbergjellet Formation, Spitsbergen. *Lethaia* **27**, 76 (1994).
303. N. J. Butterfield, *Bangiomorpha pubescans* n. gen., n. sp.: Implications for the evolution of sex, multicellularity, and the Mesoproterozoic/Neoproterozoic radiation of eukaryotes. *Paleobiology* **26**, 386–404 (2000).
304. N. J. Butterfield, Modes of pre-Ediacaran multicellularity. *Precambrian Res.* **173**, 201–211 (2009).
305. L. E. Graham, M. E. Cook, L. W. Wilcox, J. Graham, W. Taylor, C. H. Wellman, L. Lewis, Resistance of filamentous chlorophycean, ulvophycean, and xanthophycean algae to acetolysis: Testing Proterozoic and Paleozoic microfossil attributions. *Int. J. Plant Sci.* **174**, 947–957 (2013).
306. S. M. Porter, A. H. Knoll, Testate amoebae in the Neoproterozoic era: Evidence from vase-shaped microfossils in the Chuar Group, Grand Canyon. *Paleobiology* **26**, 360–385 (2000).
307. S. M. Porter, R. Meisterfeld, A. H. Knoll, Vase-shaped microfossils from the neoproterozoic Chuar Group, Grand Canyon: A classification guided by modern testate amoebae. *J. Paleontol.* **77**, 409–429 (2003).
308. S. M. Porter, The Proterozoic fossil record of heterotrophic eukaryotes, in *Neoproterozoic Geobiology and Paleobiology*, S.-H. Xiao, A. J. Kaufman, Eds. (Springer, 2006), pp. 1–21.
309. J. V. Strauss, A. D. Rooney, F. A. Macdonald, A. D. Brandon, A. H. Knoll, 740 Ma vase-shaped microfossils from Yukon, Canada: Implications for Neoproterozoic chronology and biostratigraphy. *Geology* **42**, 659–662 (2014).
310. T. Bosak, D. J. G. Lahr, S. B. Pruss, F. A. Macdonald, L. Dalton, E. Matys, Agglutinated tests in post-Sturtian cap carbonates of Namibia and Mongolia. *Earth Planet. Sci. Lett.* **308**, 29–40 (2011).
311. T. Bosak, F. Macdonald, D. Lahr, E. Matys, Putative Cryogenian ciliates from Mongolia. *Geology* **39**, 1123–1126 (2011).
312. T. Bosak, D. J. G. Lahr, S. B. Pruss, F. A. Macdonald, A. J. Gooday, L. Dalton, E. D. Matys, Possible early foraminiferans in post-Sturtian (716–635 Ma) cap carbonates. *Geology* **40**, 67–70 (2012).
313. L. A. Dalton, T. Bosak, F. A. Macdonald, D. J. G. Lahr, S. B. Pruss, Preservational and morphological variability of assemblages of agglutinated eukaryotes in Cryogenian cap carbonates of northern Namibia. *Palaios* **28**, 67–79 (2013).
314. J. J. Brocks, N. J. Butterfield, Biogeochemistry: Early animals out in the cold. *Nature* **457**, 672–673 (2009).
315. D. H. Erwin, Early metazoan life: Divergence, environment and ecology. *Philos. Trans. R. Soc. Lond. B Biol. Sci.* **370**, 20150036 (2015).
316. K. A. McFadden, S. Xiao, C. Zhou, M. Kowalewski, Quantitative evaluation of the biostratigraphic distribution of acanthomorphic acritarchs in the Ediacaran Doushantuo Formation in the Yangtze Gorges area, South China. *Precambrian Res.* **173**, 170–190 (2009).
317. P. Liu, C. Yin, S. Chen, F. Tang, L. Gao, The biostratigraphic succession of acanthomorphic acritarchs of the Ediacaran Doushantuo Formation in the Yangtze Gorges area, South China and its biostratigraphic correlation with Australia. *Precambrian Res.* **225**, 29–43 (2013).
318. X. Yuan, Z. Chen, S. Xiao, C. Zhou, H. Hua, An early Ediacaran assemblage of macroscopic and morphologically differentiated eukaryotes. *Nature* **470**, 390–393 (2011).
319. S. M. Porter, The fossil record of early eukaryotic diversification, vol. 10 of *Paleontological Society Papers* (Paleontological Society, 2004), pp. 35–50.
320. A. H. Knoll, The multiple origins of complex multicellularity. *Annu. Rev. Earth Planet. Sci.* **39**, 217–239 (2011).
321. A. H. Knoll, Paleobiological perspectives on early eukaryotic evolution. *Cold Spring Harb. Perspect. Biol.* **6**, a016121 (2014).
322. B. Runnegar, Loophole for snowball Earth. *Nature* **405**, 403–404 (2000).
323. W. R. Peltier, Y. Liu, J. W. Crowley, Snowball Earth prevention by dissolved organic carbon remineralization. *Nature* **450**, 813–818 (2007).
324. A. J. Ridgwell, M. J. Kennedy, K. Caldeira, Carbonate deposition, climate stability, and Neoproterozoic ice ages. *Science* **302**, 859–862 (2003).
325. S. Fabre, G. Berger, V. Chavagnac, P. Besson, Origin of cap carbonates: An experimental approach. *Palaeogeogr. Palaeoclimatol. Palaeoecol.* **392**, 524–533 (2013).
326. K.-J. Huang, F.-Z. Teng, B. Shen, S. Xiao, X. Lang, H.-R. Ma, Y. Fu, Y. Peng, Episode of intense chemical weathering during the termination of the 635 Ma Marinoan glaciation. *Proc. Natl. Acad. Sci. U.S.A.* **113**, 14904–14909 (2016).
327. W. T. Hyde, T. J. Crowley, S. K. Baum, W. R. Peltier, Neoproterozoic 'snowball Earth' simulations with a coupled climate/ice-sheet model. *Nature* **405**, 425–429 (2000).
328. J. P. Lewis, A. J. Weaver, S. T. Johnston, M. Eby, Neoproterozoic "snowball Earth": Dynamic sea ice over a quiescent ocean. *Paleoceanography* **18**, 1092 (2003).
329. J. P. Lewis, A. J. Weaver, M. Eby, Snowball versus slushball Earth: Dynamic versus nondynamic sea ice? *J. Geophys. Res.* **112**, C11014 (2007).
330. T. J. Crowley, W. T. Hyde, W. R. Peltier, CO_2 levels required for deglaciation of the "near-snowball" Earth. *Geophys. Res. Lett.* **28**, 283–286 (2001).
331. D. Ferreira, J. Marshall, P. A. O'Gorman, S. Seager, Climate at high-obliquity. *Icarus* **243**, 236–248 (2014).
332. J. Yang, W. R. Peltier, Y. Hu, The initiation of modern "soft snowball" and "hard snowball" climates in CCSM3. Part I: The influences of solar luminosity, CO_2 concentration, and the sea ice/snow albedo parameterization. *J. Clim.* **25**, 2711–2736 (2012).
333. J. C. Goodman, Through thick and thin: Marine and meteoric ice in a "Snowball Earth" climate. *Geophys. Res. Lett.* **33**, L16701 (2006).
334. P. F. Hoffman, G. P. Halverson, E. W. Domack, A. C. Maloof, N. L. Swanson-Hysell, G. M. Cox, Cryogenian glaciations on the southern tropical paleomargin of Laurentia (NE Svalbard and East Greenland), and a primary origin for the upper Russøya (Islay) carbon isotope excursion. *Precambrian Res.* **206–207**, 137–158 (2012).
335. R. E. Brandt, S. G. Warren, A. P. Worby, T. C. Grenfell, Surface albedo of the Antarctic sea ice zone. *J. Clim.* **18**, 3606–3622 (2005).
336. K. M. Cuffey, W. S. B. Peterson, *The Physics of Glaciers*, (Elsevier, ed. 4, 2010).
337. D. N. Thomas, G. S. Dieckmann, Antarctic sea ice—A habitat for extremophiles. *Science* **295**, 641–644 (2002).
338. B. G. Mason, D. M. Pyle, C. Oppenheimer, The size and frequency of the largest explosive eruptions on Earth. *Bull. Volcanol.* **66**, 735–748 (2004).
339. P. Huybers, C. Langmuir, Feedback between deglaciation, volcanism, and atmospheric CO_2. *Earth Planet. Sci. Lett.* **286**, 479–491 (2009).
340. S. P. Harrison, K. E. Kohfeld, C. Roelandt, T. Claquin, The role of dust in climate changes today, at the last glacial maximum, and in the future. *Earth Sci. Rev.* **54**, 43–80 (2001).
341. M. Deynoux, Periglacial polygonal structures and sand wedges in the Late Precambrian glacial formations of the Taoudeni Basin in Adrar of Mauretania (West Africa). *Palaeogeogr. Palaeoclimatol. Palaeoecol.* **39**, 55–70 (1982).
342. M. Deynoux, G. Kocurek, J. N. Proust, Late Proterozoic periglacial aeolian deposits on the West African Platform, Taoudeni Basin, western Mali. *Sedimentology* **36**, 531–549 (1989).

343. V. N. Konishchev, Characteristics of cryogenic weathering in the permafrost zone of the European USSR. *Arct. Alp. Res.* **14**, 261–265 (1982).
344. I. J. Smalley, The properties of glacial loess and the formation of loess deposits. *J. Sediment. Res.* **36**, 669–676 (1966).
345. B. Peucker-Ehrenbrink, C. A. Waters, M. D. Kurz, P. F. Hoffman, No evidence of extraterrestrial noble metal and helium anomalies at Marinoan glacial termination. *Earth Planet. Sci. Lett.* **437**, 76–88 (2016).
346. S. L. Harder, S. G. Warren, R. J. Charlson, D. S. Covert, Filtering of air through snow as a mechanism for aerosol deposition to the Antarctic ice sheet. *J. Geophys. Res.* **101**, 18729–18743 (1996).
347. D. R. Mueller, W. F. Vincent, Microbial habitat dynamics and ablation control on the Ward Hunt Ice Shelf. *Hydrol. Process.* **20**, 857–876 (2006).
348. W. F. Vincent, Cyanobacterial dominance in the polar regions, in *The Ecology of Cyanobacteria*, B. A. Whitton, M. Potts, Eds. (Kluwer Academic, 2000), pp. 321–340.
349. D. R. Mueller, W. F. Vincent, S. Bonilla, I. Laurion, Extremotrophs, extremophiles and broadband pigmentation strategies in a high arctic ice shelf ecosystem. *FEMS Microbiol. Ecol.* **53**, 73–87 (2005).
350. C. Klein, N. J. Beukes, Sedimentology and geochemistry of the glacigenic Late Proterozoic Rapitan iron-formation in Canada. *Econ. Geol.* **88**, 542–565 (1993).
351. D. T. Johnston, S. W. Poulton, C. Dehler, S. Porter, J. Husson, D. E. Canfield, A. H. Knoll, An emerging picture of Neoproterozoic ocean chemistry: Insights from the Chuar Group, Grand Canyon, USA. *Earth Planet. Sci. Lett.* **290**, 64–73 (2010).
352. T. W. Dahl, D. E. Canfield, M. T. Rosing, R. E. Frei, G. W. Gordon, A. H. Knoll, A. D. Anbar, Molybdenum evidence for expansive sulfidic water masses in ~750 Ma oceans. *Earth Planet. Sci. Lett.* **311**, 264–274 (2011).
353. E. A. Sperling, G. P. Halverson, A. H. Knoll, F. A. Macdonald, D. T. Johnston, A basin redox transect at the dawn of animal life. *Earth Planet. Sci. Lett.* **371–372**, 143–155 (2013).
354. A. v. S. Hood, M. W. Wallace, C. P. Reed, K.-H. Hoffmann, E. E. Freyer, Enigmatic carbonates of the Ombombo Subgroup, Otavi Fold Belt, Namibia: A prelude to extreme Cryogenian anoxia? *Sediment. Geol.* **324**, 12–31 (2015).
355. J. Farquhar, N.-P. Wu, D. E. Canfield, H. Oduro, Connections between sulfur cycle evolution, sulfur isotopes, sediments, and base metal sulfide deposits. *Econ. Geol.* **105**, 509–533 (2010).
356. T. A. Laakso, D. P. Schrag, A theory of atmospheric oxygen. *Geobiology* **15**, 366–384 (2017)
357. S. K. Sahoo, N. J. Planavsky, B. Kendall, X. Wang, X. Shi, C. Scott, A. D. Anbar, T. W. Lyons, G. Jiang, Ocean oxygenation in the wake of the Marinoan glaciation. *Nature* **489**, 546–549 (2012).
358. P. A. E. Pogge von Strandmann, E. E. Stüeken, T. Elliott, S. W. Poulton, C. M. Dehler, D. E. Canfield, D. C. Catling, Selenium isotope evidence for progressive oxidation of the Neoproterozoic biosphere. *Nat. Commun.* **6**, 10157 (2015).
359. K. V. Lau, F. A. Macdonald, K. Maher, J. L. Payne, Uranium isotope evidence for temporary ocean oxygenation in the aftermath of the Sturtian Snowball Earth. *Earth Planet. Sci. Lett.* **458**, 282–292 (2016).
360. M. Kunzmann, T. H. Bui, P. W. Crockford, G. P. Halverson, C. Scott, T. W. Lyons, B. A. Wing, Bacterial sulfur disproportionation constrains timing of Neoproterozoic oxygenation. *Geology* **45**, 207–210 (2017).
361. N. J. F. Blamey, U. Brand, J. Parnell, N. Spear, C. Lécuyer, K. Benison, F. Meng, P. Ni, Paradigm shift in determining Neoproterozoic atmospheric oxygen. *Geology* **44**, 651–654 (2016).
362. M. Brasier, G. McCarron, R. Tucker, J. Leather, P. Allen, G. Shields, New U-Pb zircon dates for the Neoproterozoic Ghubrah glaciation and for the top of the Huqf Supergroup, Oman. *Geology* **28**, 175–178 (2000).
363. K. Lund, J. N. Aleinikoff, K. V. Evans, C. M. Fanning, SHRIMP U-Pb geochronology of Neoproterozoic Windermere Supergroup, central Idaho: Implications for rifting of western Laurentia and synchroneity of Sturtian glacial deposits. *Geol. Soc. Am. Bull.* **115**, 349–372 (2003).
364. C. M. Fanning, P. K. Link, U-Pb SHRIMP ages of Neoproterozoic (Sturtian) glaciogenic Pocatello Formation, southeastern Idaho. *Geology* **32**, 881–884 (2004).
365. S. A. Bowring, J. P. Grotzinger, D. J. Condon, J. Ramezani, M. J. Newall, P. A. Allen, Geochronologic constraints on the chronostratigraphic framework of the Neoproterozoic Huqf Supergroup, Sultanate of Oman. *Am. J. Sci.* **307**, 1097–1145 (2007).
366. C. M. Fanning, P. K. Link, Age constraints for the Sturtian glaciation: Data from the Adelaide Geosyncline, South Australia and Pocatello Formation, Idaho, USA, in *Selwyn Symposium 2008* (Geological Society of Australia, Abstract No. 91, 2008).
367. Q. R. Zhang, J. D. A. Piper, Palaeomagnetic study of Neoproterozoic glacial rocks of the Yangzi Block: Palaeolatitude and configuration of South China in the late Proterozoic supercontinent. *Precambrian Res.* **85**, 173–199 (1997).
368. S. Zhang, D. A. D. Evans, H. Li, H. Wu, G. Jiang, J. Dong, Q. Zhao, T. D. Raub, T. Yang, Paleomagnetism of the late Cryogenian Nantuo Formation and paleogeographic implications for the South China Block. *J. Asian Earth Sci.* **72**, 164–177 (2013).
369. P.-A. Knight, P. E. Fell, Low salinity induces reversible tissue regression in the estuarine sponge *Microciona prolifera* (Ellis & Solander). *J. Exp. Mar. Biol. Ecol.* **107**, 253–261 (1987).
370. J. Leamon, P. E. Fell, Upper salinity tolerance of and salinity-induced tissue regression in the estuarine sponge *Microciona prolifera*. *Trans. Am. Microsc. Soc.* **109**, 265–272 (1990).
371. C. Borchiellini, C. Chombard, M. Manuel, E. Alivon, J. Vacelet, N. Boury-Esnault, Molecular phylogeny of Demospongiae: Implications for classification and scenarios of character evolution. *Mol. Phylogenet. Evol.* **32**, 823–837 (2004).
372. D. V. Lavrov, X. Wang, M. Kelly, Reconstructing ordinal relationships in the Demospongiae using mitochondrial genomic data. *Mol. Phylogenet. Evol.* **49**, 111–124 (2008).
373. H. Philippe, H. Brinkmann, D. V. Lavrov, D. T. J. Littlewood, M. Manuel, G. Wörheide, D. Baurain, Resolving difficult phylogenetic questions: Why more sequences are not enough. *PLOS Biol.* **9**, e1000602, (2011).
374. P. K. Dayton, G. A. Robilliard, A. L. Devries, Anchor ice formation in McMurdo Sound, Antarctica, and its biological effects. *Science* **163**, 273–274 (1969).
375. J. A. Dowdeswell, K. A. Hogan, N. S. Arnold, R. I. Mugford, M. Wells, J. P. P. Hirst, C. Decalf, Sediment-rich meltwater plumes and ice-proximal fans at the margins of modern and ancient tidewater glaciers: Observations and modeling. *Sedimentology* **62**, 1665–1692 (2015).
376. P. E. Fell, P.-A. Knight, W. Rieders, Low-salinity tolerance of and salinity-induced dormancy in the estuarine sponge *Microciona prolifera* (Ellis *et* Solander) under long-term laboratory culture. *J. Exp. Mar. Biol. Ecol.* **133**, 195–211 (1989).
377. D. A. D. Evans, Proterozoic low orbital obliquity and axial-dipolar geomagnetic field from evaporite palaeolatitudes. *Nature* **444**, 51–55 (2006).
378. N. Spear, H. D. Holland, J. Garcia-Veígas, T. K. Lowenstein, R. Giegengack, H. Peters, Analyses of fluid inclusions in Neoproterozoic marine halite provide oldest measurement of seawater chemistry. *Geology* **42**, 103–106 (2014).
379. D. Thomson, R. H. Rainbird, N. Planavsky, T. W. Lyons, A. Bekker, Chemostratigraphy of the Shaler Supergroup, Victoria Island, NW Canada: A record of ocean composition prior to the Cryogenian glaciations. *Precambrian Res.* **263**, 232–245 (2015).
380. J. B. Antcliffe, R. H. T. Callow, M. D. Brasier, Giving the early fossil record of sponges a squeeze. *Biol. Rev.* **89**, 972–1004 (2014).
381. T. Cavalier-Smith, Origin of animal multicellularity: Precursors, causes, consequences—The choanoflagellate/sponge transition, neurogenesis and the Cambrian explosion. *Philos. Trans. R. Soc. Lond. B Biol. Sci.* **372**, 20150476 (2017).
382. P. Sánchez-Baracaldo, A. Ridgwell, J. A. Raven, A Neoproterozoic transition in the marine nitrogen cycle. *Curr. Biol.* **24**, 652–657 (2014).
383. P. Sánchez-Baracaldo, Origin of marine planktonic cyanobacteria. *Sci. Rep.* **5**, 17418 (2015).
384. L. M. Powell, J. P. Bowman, J. H. Skerratt, P. D. Franzmann, H. R. Burton, Ecology of a novel *Synechococcus* clade occurring in dense populations in saline Antarctic lakes. *Mar. Ecol. Prog. Ser.* **291**, 65–80 (2005).
385. J. Laybourn-Parry, E. M. Bell, Ace Lake: Three decades of research on a meromictic, Antarctic lake. *Polar Biol.* **37**, 1685–1699 (2014).
386. W. K. W. Li, From cytometry to macroecology: A quarter century quest in microbial oceanography. *Aquat. Microb. Ecol.* **57**, 239–251 (2009).
387. J. Yang, M. F. Jansen, F. A. Macdonald, D. S. Abbot, Persistence of a surface freshwater ocean after a Snowball Earth. *Geology* **45**, 615–618 (2017).
388. P. F. Hoffman, P. Sanchez-Baracaldo, W. F. Vincent, Expanded freshwater oligotrophy on Snowball Earth and the origin of modern marine planktonic cyanobacteria (Geological Association of Canada, 2017); http://gac.esd.mun.ca/GAC_2017/ search_abs/sub_program.asp?sess=10&abs_no=187.
389. Y. Isozaki, Memories of pre-Jurassic lost oceans: How to retrieve them from extant lands. *Geosci. Can.* **41**, 283–311 (2014).
390. Y. Ashkenazy, H. Gildor, M. Losch, F. A. Macdonald, D. P. Schrag, E. Tziperman, Dynamics of a Snowball Earth ocean. *Nature* **495**, 90–93 (2013).
391. Y. Ashkenazy, H. Gildor, M. Losch, E. Tziperman, Ocean circulation under globally glaciated Snowball Earth conditions: Steady-state solutions. *J. Phys. Oceanogr.* **44**, 24–43 (2014).
392. Y. Ashkenazy, E. Tziperman, Variability, instabilities, and eddies in a Snowball Ocean. *J. Clim.* **29**, 869–888 (2016).
393. M. F. Jansen, The turbulent circulation of a Snowball Earth ocean. *J. Phys. Oceanogr.* **46**, 1917–1933 (2016).
394. C. Wunsch, *Modern Observational Physical Oceanography: Understanding the Global Ocean* (Princeton Univ. Press, 2015).
395. C. Wunsch, R. Ferrari, Vertical mixing, energy, and the general circulation of the oceans. *Annu. Rev. Fluid Mech.* **36**, 281–314 (2004).
396. R. Ferrari, C. Wunsch, Ocean circulation kinetic energy: Reservoirs, sources and sinks. *Annu. Rev. Fluid Mech.* **41**, 253–282 (2009).
397. Y.-G. Liu, W. R. Peltier, Sea level variations during snowball Earth formation: 1. A preliminary analysis. *J. Geophys. Res. Solid Earth* **118**, 4410–4424 (2013).
398. C. Wunsch, Tides of global ice-covered oceans. *Icarus* **274**, 122–130 (2016).

399. A. Bekker, J. F. Slack, N. Planavsky, B. Krapež, A. Hofmann, K. O. Konnhauser, O. Rouxel, Iron formation: The sedimentary product of a complex interplay among mantle, tectonic, oceanic, and biospheric processes. *Econ. Geol.* **105**, 467–508 (2010).
400. G. M. Cox, G. P. Halverson, W. G. Minarik, D. P. Le Heron, F. A. Macdonald, E. J. Bellefroid, J. V. Strauss, Neoproterozoic iron formation: An evaluation of its temporal, environmental and tectonic significance. *Chem. Geol.* **362**, 232–249 (2013).
401. W. W. Fischer, A. H. Knoll, An iron shuttle for deepwater silica in Late Archean and early Paleoproterozoic iron formation. *Geol. Soc. Am. Bull.* **121**, 222–235 (2009).
402. J. C. G. Walker, Was the Archaean biosphere upside down? *Nature* **329**, 710–712 (1987).
403. C. M. Johnson, J. M. Ludois, B. L. Beard, N. J. Beukes, A. Heimann, Iron formation carbonates: Paleoceanographic proxy or recorder of microbial diagenesis? *Geology* **41**, 1147–1150 (2013).
404. H. Urban, B. Stribny, H. J. Lippolt, Iron and manganese deposits of the Urucum District, Mato Grosso do Sul, Brazil. *Econ. Geol.* **87**, 1375–1892 (1992).
405. D. E. Canfield, R. Raiswell, The evolution of the sulfur cycle. *Am. J. Sci.* **299**, 697–723 (1999).
406. J. A. Mikucki, A. Pearson, D. T. Johnston, A. V. Turchyn, J. Farquhar, D. P. Schrag, A. D. Anbar, J. C. Priscu, P. A. Lee, A contemporary microbially maintained subglacial ferrous "ocean." *Science* **324**, 397–400 (2009).
407. L. R. Kump, W. E. Seyfried Jr., Hydrothermal Fe fluxes during the Precambrian: Effect of low oceanic sulfate concentrations and low hydrostatic pressure on the composition of black smokers. *Earth Planet. Sci. Lett.* **235**, 654–662 (2005).
408. N. J. Planavsky, O. J. Rouxel, A. Bekker, S. V. Lalonde, K. O. Konnhauser, C. T. Reinhard, T. W. Lyons, The evolution of the marine phosphate reservoir. *Nature* **467**, 1088–1090 (2010).
409. P. F. Hoffman, G. P. Halverson, Neoproterozoic glacial record in the Mackenzie Mountains, northern Canadian Cordillera, in *The Geological Record of Neoproterozoic Glaciations*, E. Arnaud, G. P. Halverson, G. Shields-Zhou, Eds. (Geological Society of London, 2011), pp. 397–411.
410. W. V. Preiss, V. A. Gostin, D. M. McKirdy, P. M. Ashley, G. E. Williams, P. W. Schmidt, The glacial succession of Sturtian age in South Australia: The Yudnamutana Subgroup, in *The Geological Record of Neoproterozoic Glaciations*, E. Arnaud, G. P. Halverson, G. Shields-Zhou, Eds. (Geological Society of London, 2011), pp. 701–712.
411. B. G. Lottermoser, P. M. Ashley, Geochemistry, petrology and origin of Neoproterozoic ironstones in the eastern part of the Adelaide Greosyncline, South Australia. *Precambrian Res.* **101**, 49–67 (2000).
412. G. P. Halverson, F. Poitrasson, P. F. Hoffman, A. Nédélec. J.-M. Montel, J. Kirby, Fr isotope and trace element geochemistry of the Neoproterozoic syn-glacial Rapitan iron formation. *Earth Planet. Sci. Lett.* **309**, 100–112 (2011).
413. G. J. Baldwin, E. C. Turner, B. S. Kamber, A new depositional model for glacigenic Neoproterozoic iron formation: Insights from the chemostratigraphy and basin configuration of the Rapitan iron formation. *Can. J. Earth Sci.* **49**, 455–476 (2012).
414. T. Angerer, S. G. Hagemann, D. H. G. Walde, G. P. Halverson, A. J. Boyce, Multiple metal sources in the glaciomarine facies of the Neoproterozoic Jacadigo iron formation in the "Santa Cruz deposit", Corumbá, Brazil. *Precambrian Res.* **275**, 369–393 (2016).
415. M. Lechte, M. Wallace, Sub-ice shelf ironstone deposition during the Neoproterozoic Sturtian glaciation. *Geology* **44**, 891–894 (2016).
416. N. P. James, G. M. Narbonne, T. K. Kyser, Late Neoproterozoic cap carbonates: Mackenzie Mountains, northwestern Canada: Precipitation and global glacial meltdown. *Can. J. Earth Sci.* **38**, 1229–1262 (2001).
417. G. Jiang, M. J. Kennedy, N. Christie-Blick, H. Wu, S. Zhang, Stratigraphy, sedimentary structures, and textures of the late Neoproterozoic Doushantuo cap carbonate in South China. *J. Sediment. Res.* **76**, 978–995 (2006).
418. E. G. Williams, L. A. Wright, B. W. Troxel, The Noonday Dolomite and equivalent stratigraphic units, southern Death Valley region, California, in *Guidebook: Death Valley Region, California and Nevada*, L. A. Wright, B. Troxel, Eds. (Death Valley Publishing, 1974), pp. 73–77.
419. J. R. Creveling, J. X. Mitrovica, The sea-level fingerprint of a Snowball Earth deglaciation. *Earth Planet. Sci. Lett.* **399**, 74–85 (2014).
420. T. M. Peryt, A. Hoppe, T. Bechstädt, J. Köster, C. Pierre, D. K. Richter, Late Proterozoic aragonitic cement crusts, Bambuí Group, Minas Gerais, Brazil. *Sedimentology* **37**, 279–286 (1990).
421. J. P. Grotzinger, A. H. Knoll, Anomalous carbonate precipitates: Is the Precambrian the key to the Permian? *Palaios* **10**, 578–596 (1995).
422. L. C. Vieira, A. Nédélec, S. Fabre, R. I. F. Trindade, R. Paes de Almeida, Aragonite crystal fans in Neoproterozoic cap carbonates: A case study from Brazil and implications for the post–Snowball environment. *J. Sediment. Res.* **85**, 285–300 (2015).
423. J. A. Higgins, W. W. Fischer, D. P. Schrag, Oxygenation of the ocean and sediments: Consequences for the seafloor carbonate factory. *Earth Planet. Sci. Lett.* **284**, 25–33 (2009).
424. E. Norin, Geology of western Quruq Tagh, eastern Tien-Shan, in *Reports from the Scientific Expedition to the North-Western Provinces of China Under the Leadership of Dr. Sven Hedin, the Sino-Swedish Expedition*, S. Hedin, Ed. (Bokförlags Aktiebolaget Thule, 1937), 171 pp.
425. P. F. Hoffman, F. A. Macdonald, Sheet-crack cements and early regression in Marinoan (635 Ma) cap dolostones: Regional benchmarks of vanishing ice-sheets? *Earth Planet. Sci. Lett.* **300**, 374–384 (2010).
426. G. J. Retallack, Neoproterozoic loess and limits to snowball Earth. *J. Geol. Soc. London* **168**, 289–307 (2011).
427. C. V. Rose, A. C. Maloof, Testing models for post-glacial 'cap dolostone' deposition: Nuccaleena Formation, South Australia. *Earth Planet. Sci. Lett.* **296**, 165–180 (2010).
428. R. I. F. Trindade, E. Font, M. S. D'Agrella-Filho, A. C. R. Nogueira, C. Riccomini, Low-latitude and multiple geomagnetic reversals in the Neoproterozoic Puga cap carbonate, Amazon craton. *Terra Nova* **15**, 441–446 (2003).
429. B. Kilner, C. Mac Niocaill, M. Brasier, Low-latitude glaciation in the Neoproterozoic of Oman. *Geology* **33**, 413–416 (2005).
430. T. D. Raub, "Prolonged Deglaciation of "Snowball Earth"," thesis, Yale University (2008).
431. E. Font, A. Nédélec, R. I. F. Trindade, C. Moreau, Fast or slow melting of the Marinoan snowball Earth? The cap dolostone record. *Palaeogeogr. Palaeoclimatol. Palaeoecol.* **295**, 215–225 (2010).
432. B. M. Clement, Dependence of the duration of geomagnetic polarity reversals on site latitude. *Nature* **428**, 637–640 (2004).
433. S. Labrosse, Thermal evolution of the core with a high thermal conductivity. *Phys. Earth Planet. Inter.* **247**, 36–55 (2015).
434. D. Gubbins, D. Alfè, C. Davies, M. Pozzo, On core convection and the geodynamo: Effects of high electrical and thermal conductivity. *Phys. Earth Planet. Inter.* **247**, 56–64 (2015).
435. C. J. Davies, Cooling history of Earth's core with high thermal conductivity. *Phys. Earth Planet. Inter.* **247**, 65–79 (2015).
436. P. F. Hoffman, A. J. Kaufman, G. P. Halverson, Comings and goings of global glaciations on a Neoproterozoic tropical platform in Namibia. *GSA Today* **8**, 1–9 (1998).
437. A. C. R. Nogueira, C. Riccomini, A. N. Sial, C. A. V. Moura, R. I. F. Trindade, T. R. Fairchild, Carbon and strontium isotope fluctuations and paleoceanographic changes in the late Neoproterozoic Araras carbonate platform, southern Amazon craton, Brazil. *Chem. Geol.* **237**, 168–190 (2007).
438. R. L. Folk, Practical petrographic classification of limestones. *AAPG Bull.* **43**, 1–38 (1959).
439. L. Wright, E. G. Williams, P. Cloud, Algal and cryptalgal structures and platform environments of the late pre-Phanerozoic Noonday Dolomite, eastern California. *Geol. Soc. Am. Bull.* **89**, 321–333 (1978).
440. P. Cloud, L. A. Wright, E. G. Williams, P. Diehl, M. R. Walter, Giant stromatolites and associated vertical tubes from the Upper Proterozoic Noonday Dolomite, Death Valley region, eastern California. *Geol. Soc. Am. Bull.* **85**, 1869–1882 (1974).
441. F. A. Corsetti, J. P. Grotzinger, Origin and significance of tube structures in Neoproterozoic post-glacial cap carbonates: Example from Noonday Dolomite, Death Valley, United States. *Palaios* **20**, 348–362 (2005).
442. T. Bosak, G. Mariotti, F. A. Macdonald, J. T. Perron, S. B. Pruss, Microbial sedimentology in Neoproterozoic cap carbonates, vol. 19 of *Paleontological Society Papers* (Paleontological Society, 2013), pp. 1–25.
443. P. A. Allen, P. F. Hoffman, Extreme winds and waves in the aftermath of a Neoproterozoic glaciation. *Nature* **433**, 123–127 (2005).
444. B. Shen, S. Xiao, A. J. Kaufman, H. Bao, C. Zhou, H. Wang, Stratification and mixing of a post-glacial Neoproterozoic ocean: Evidence from carbon and sulfur isotopes in a cap dolostone from northwest China. *Earth Planet. Sci. Lett.* **265**, 209–228 (2008).
445. C. Liu, Z. Wang, T. D. Raub, F. A. Macdonald, D. A. D. Evans, Neoproterozoic cap-dolostone deposition in stratified glacial meltwater plume. *Earth Planet. Sci. Lett.* **404**, 22–32 (2014).
446. M. J. Kennedy, N. Christie-Blick, A. R. Prave, Carbon isotopic composition of Neoproterozoic glacial carbonates as a test of paleoceanographic models for snowball Earth phenomena. *Geology* **29**, 1135–1138 (2001).
447. S. Fabre, G. Berger, How tillite weathering during the snowball Earth aftermath induced cap carbonate deposition. *Geology* **40**, 1027–1030 (2012).
448. G. Le Hir, Y. Donnadieu, Y. Goddéris, R. T. Pierrehumbert, G. P. Halverson, M. Macouin, A. Nédélec, G. Ramstein, The snowball Earth aftermath: Exploring the limits of continental weathering processes. *Earth Planet. Sci. Lett.* **277**, 453–463 (2009).
449. S. Fabre, G. Berger, A. Nédélec, Modeling of continental weathering under high-CO_2 atmospheres during Precambrian times. *Geochem. Geophys. Geosyst.* **12**, Q10001 (2011).
450. E. Font, A. Nédélec, R. I. F. Trindade, M. Macouin, A. Charrière, Chemostratigraphy of the Neoproterozoic Mirassol d'Oeste cap dolostones (Mato Grosso, Brazil): An alternative model for Marinoan cap dolostone formation. *Earth Planet. Sci. Lett.* **250**, 89–103 (2006).
451. P. R. Gammon, An organosedimentary model for Marinoan-age cap carbonates. *Sediment. Geol.* **243–244**, 17–32 (2012).

452. P. A. Kenward, R. H. Goldstein, L. A. González, J. A. Roberts, Precipitation of low-temperature dolomite from an aerobic microbial consortium: The role of methanogenic Archaea. *Geobiology* **7**, 1–10 (2009).
453. F. A. Macdonald, D. S. Jones, The Khubsugul Group, Northern Mongolia, in *The Geological Record of Neoproterozoic Glaciations*, E. Arnaud, G. P. Halverson, G. Shields-Zhou, Eds. (Geological Society of London, 2011), pp. 339–345.
454. C. Vincent, A. Fischer, C. Mayer, A. Bauder, S. P. Galos, M. Funk, E. Thibert, D. Six, L. Braun, M. Huss, Common climatic signal from glaciers in the European Alps over the last 50 years. *Geophys. Res. Lett.* **44**, 1376–1383 (2017).
455. J. X. Mitrovica, J. Wahr, Ice age Earth rotation. *Annu. Rev. Earth Planet. Sci.* **39**, 577–616 (2011).
456. A. Wegener, *The Origin of Continents and Oceans*, J. Biram, Transl. (Dover, ed. 4, 1928).
457. J. E. Mound, J. X. Mitrovica, True polar wander as a mechanism for second-order sea-level variations. *Science* **279**, 534–537 (1998).
458. M. Pozzo, C. Davies, D. Gubbins, D. Alfè, Thermal and electrical conductivity of iron at Earth's core conditions. *Nature* **485**, 355–358 (2012).
459. H. Gomi, K. Hirose, Electrical resistivity and thermal conductivity of hcp Fe–Ni alloys under high pressure: Implications for thermal convection in the Earth's core. *Phys. Earth Planet. Inter.* **247**, 2–10 (2015).
460. K. Ohta, Y. Kuwayama, K. Hirose, K. Shimizu, Y. Ohishi, Experimental determination of the electrical resistivity of iron at Earth's core conditions. *Nature* **534**, 95–98 (2016).
461. Z. Konôpková, R. S. McWilliams, N. Gómez-Pérez, A. F. Goncharov, Direct measurement of thermal conductivity in solid iron at planetary core conditions. *Nature* **534**, 99–101 (2016).
462. D. Dobson, Geophysics: Earth's core problem. *Nature* **534**, 45 (2016).
463. D. Gubbins, The distinction between geomagnetic excursions and reversals. *Geophys. J. Int.* **137**, F1–F3 (1999).
464. A. Abrajevitch, R. Van der Voo, Incompatible Ediacaran paleomagnetic directions suggest an equatorial geomagnetic dipole hypothesis. *Earth Planet. Sci. Lett.* **293**, 164–170 (2010).
465. H. C. Halls, A. Lovette, M. Hamilton, U. Söderlund, A paleomagnetic and U–Pb geochronology study of the western end of the Grenville dyke swarm: Rapid changes in paleomagnetic field direction at ca. 585 Ma related to polarity reversals? *Precambrian Res.* **257**, 137–166 (2015).
466. M. L. Bazhenov, N. M. Levashova, J. G. Meert, I. V. Golovanova, K. N. Danukalov, N. M. Federova, Late Ediacaran magnetostratigraphy of Baltica: Evidence for magnetic field hyperactivity. *Earth Planet. Sci. Lett.* **435**, 124–135 (2016).
467. J. G. O'Rourke, D. J. Stevenson, Powering Earth's dynamo with magnesium precipitation from the core. *Nature* **529**, 387–389 (2016).
468. G. P. Halverson, A Neoproterozoic chronology, in *Neoproterozoic Geobiology and Paleobiology*, S.-H. Xiao, A. J. Kaufman, Eds. (Springer, 2006), pp. 231–271.
469. R. Petterson, A. R. Prave, B. P. Wernicke, A. E. Fallick, The Neoproterozoic Noonday Formation, Death Valley region, California. *Geol. Soc. Am. Bull.* **123**, 1317–1336 (2011).
470. J. R. Creveling, K. D. Bergmann, J. P. Grotzinger, Cap carbonate platform facies model, Noonday Formation, SE California. *Geol. Soc. Am. Bull.* **128**, 1249–1269 (2016).
471. M. Kunzmann, G. P. Halverson, P. A. Sossi, T. D. Raub, J. L. Payne, J. Kirby, Zn isotope evidence for immediate resumption of primary productivity after snowball Earth. *Geology* **41**, 27–30 (2013).
472. S. G. John, M. Kunzmann, E. J. Townsend, A. D. Rosenberg, Zinc and cadmium stable isotopes in the geological record: A case study from the post-snowball Nuccaleena cap dolostone. *Palaeogeogr. Palaeoclimatol. Palaeoecol.* **466**, 202–208 (2017).
473. J. P. Grotzinger, N. P. James, Precambrian carbonates: Evolution of understanding, in *Carbonate Sedimentation and Diagenesis in the Evolving Precambrian World*, J. P. Grotzinger, N. P. James, Eds. (Society for Sedimentary Geology, Special Publication 67, 2000), pp. 3–20.
474. B. Tojo, N. Katsuta, M. Takano, S. Kawakami, T. Ohno, Calcite–dolomite cycles in the Neoproterozoic Cap carbonates, Otavi Group, Namibia, in *The Rise and Fall of the Ediacaran Biota*, P. Vickers-Rich, P. Komarower, Eds. (Geological Society of London, Special Publication 286, 2007), pp. 103–113.
475. S. B. Pruss, T. Bosak, F. A. Macdonald, M. McLane, P. F. Hoffman, Microbial facies in a Sturtian cap carbonate, the Rasthof Formation, Otavi Group, northern Namibia. *Precambrian Res.* **181**, 187–198 (2010).
476. J. A. Giddings, M. W. Wallace, Sedimentology and C-isotope geochemistry of the 'Sturtian' cap carbonate, South Australia. *Sediment. Geol.* **216**, 1–14 (2009).
477. K. R. Moore, T. Bosak, F. A. Macdonald, D. J. G. Lahr, S. Newman, C. Settens, S. B. Pruss, Biologically-agglutinated eukaryotic microfossil from Cryogenian cap carbonates. *Geobiology* **15**, 499–515 (2017).
478. E. Le Ber, D. P. Le Heron, G. Winterleitner, D. W. J. Bosence, B. A. Vining, F. Kamona, Microbialite recovery in the aftermath of the Sturtian glaciation: Insights from the Rasthof Formation, Namibia. *Sediment. Geol.* **294**, 1–12 (2013).
479. M. W. Wallace, A. v. S. Hood, E. M. S. Woon, K.-H. Hoffmann, C. P. Reed, Enigmatic chambered structures in Cryogenian reefs: The oldest sponge-grade organisms? *Precambrian Res.* **255**, 109–123 (2014).
480. P. Gorjan, J. J. Veevers, M. R. Walter, Neoproterozoic sulfur-isotope variation in Australia and global implications. *Precambrian Res.* **100**, 151–179 (2000).
481. J. C. Silva-Tamayo, T. F. Nägler, I. M. Villa, K. Kyser, L. C. Vieira, A. N. Sial, G. M. Narbonne, N. P. James, Global Ca isotope variations in *c.* 0.7 Ga old post-glacial carbonate successions. *Terra Nova* **22**, 188–194 (2010).
482. J. C. Silva-Tamayo, T. F. Nägler, A. N. Sial, A. Nogueira, K. Kyser, C. Riccomini, N. P. James, G. M. Narbonne, I. M. Villa, Global perturbation of the marine Ca isotopic composition in the aftermath of the Marinoan global glaciation. *Precambrian Res.* **182**, 373–381 (2010).
483. G. P. Halverson, G. Shields-Zhou, Chemostratigraphy and the Neoproterozoic glaciations, in *The Geological Record of Neoproterozoic Glaciations*, E. Arnaud, G. P. Halverson, G. Shields-Zhou, Eds. (Geological Society of London, 2011), pp. 51–66.
484. J. Farquhar, B. A. Wing, Multiple sulfur isotopes and the evolution of the atmosphere. *Earth Planet. Sci. Lett.* **213**, 1–13 (2003).
485. A. R. Prave, A. E. Fallick, C. W. Thomas, C. M. Graham, A composite C-isotope profile for the Neoproterozoic Dalradian Supergroup of Scotland and Ireland. *J. Geol. Soc. London* **166**, 845–857 (2009).
486. G. P. Halverson, A. C. Maloof, P. F. Hoffman, The Marinoan glaciation (Neoproterozoic) in northeast Svalbard. *Basin Res.* **16**, 297–324 (2004).
487. M. Kunzmann, G. P. Halverson, C. Scott, W. G. Minarik, B. A. Wing, Geochemistry of Neoproterozoic black shales from Svalbard: Implications for oceanic redox conditions spanning Cryogenian glaciations. *Chem. Geol.* **417**, 383–393 (2015).
488. M. Tahata, Y. Sawaki, K. Yoshiya, M. Nishizawa, T. Komiya, T. Hirata, N. Yoshida, S. Maruyama, B. F. Windley, The marine environment encompassing the Neoproterozoic glaciations: Evidence from C, Sr, and Fe isotope ratios in the Hecla Hoek Supergroup in Svalbard. *Precambrian Res.* **263**, 19–42 (2015).
489. W. D. Collins, P. J. Rasch, B. A. Boville, J. J. Hack, J. R. McCaa, D. L. Williamson, J. T. Kiehl, B. Briegleb, C. Bitz, S.-J. Lin, M. Zhang, Y. Dai, *Description of the NCAR Community Atmosphere Model (CAM 3.0),* NCAR Technical Note NCAR/TN-464+STR (National Center for Atmospheric Research, 2004).
490. M. F. Khairoutdinov, D. A. Randall, A cloud resolving model as a cloud parameterization in the NCAR community climate system model: Preliminary results. *Geophys. Res. Lett.* **28**, 3617–3620 (2001).
491. M. C. Khairoutdinov, C. DeMott, D. Randall, Evaluation of the simulated interannual subseasonal variability in an AMIP-style simulation using the CSU multiscale modeling framework. *J. Clim.* **21**, 413–431 (2008).
492. R. Jacob, "Low frequency variability in a simulated atmosphere ocean system," thesis, University of Wisconsin-Madison, Madison, WI (1997).
493. B. Stevens, M. Giorgetta, M. Esch, T. Mauritsen, T. Crueger, S. Rast, M. Salzmann, H. Schmidt, J. Bader, K. Block, Renate Brokopf, I. Fast, S. Kinne, L. Kornblueh, U. Lohmann, R. Pincus, T. Reichler, E. Roeckner, Atmospheric component of the MPI-M Earth System Model: ECHAM6. *J. Adv. Model. Earth Syst.* **5**, 146–172 (2013).
494. S. L. Thompson, D. Pollard, Greenland and Antarctic mass balance for present and doubled atmospheric CO_2 from the GENESIS version-2 global climate model. *J. Clim.* **10**, 871–900 (1997).
495. J. R. Alder, S. W. Hostetler, D. Pollard, A. Schmittner, Evaluation of a present-day climate simulation with a new coupled atmosphere-ocean model GENMOM. *Geosci. Model Dev.* **4**, 69–83 (2011).
496. D. Pollard, J. F. Kasting, Snowball Earth: A thin-ice solution with flowing glaciers. *J. Geophys. Res.* **110**, C07010 (2005).
497. G. M. Young, V. A. Gostin, Late Proterozoic (Sturtian) succession of the North Flinders Basin, South Australia: An example of temperate glaciation in an active rift setting, in *Glacial Marine Sedimentation: Paleoclimatic Significance*, J. B. Anderson, G. M. Ashley, Eds. (Geological Society of America, 1991), pp. 207–222.
498. D. P. Le Heron, M. E. Busfield, A. S. Collins, Bolla Bollana boulder beds: A Neoproterozoic trough mouth fan in South Australia? *Sedimentology* **61**, 978–995 (2014).
499. J. D. Aitken, The Ice Brook Formation and post-Rapitan, Late Proterozoic glaciation, Mackenzie Mountains, Northwest Territories. *Geol. Surv. Can. Bull.* **404**, 1–43 (1991).
500. S. Xiao, H. Bao, H. Wang, A. J. Kaufman, C. Zhou, G. Li, X. Yuan, H. Ling, The Neoproterozoic Quruqtagh Group in eastern Chinese Tianshan: Evidence for a post-Marinoan glaciation. *Precambrian Res.* **130**, 1–26 (2004).
501. F. A. Macdonald, D. S. Jones, D. P. Schrag, Stratigraphic and tectonic implications of a newly discovered glacial diamictite–cap carbonate couplet in southwestern Mongolia. *Geology* **37**, 123–126 (2009).
502. L. Yin, M. Zhu, A. H. Knoll, X. Yuan, J. Zhang, J. Hu, Doushantuo embryos preserved inside diapause egg cysts. *Nature* **446**, 661–663 (2007).
503. L. Chen, S. Xiao, K. Pang, C. Zhou, X. Yuan, Cell differentiation and germ–soma separation in Ediacaran animal embryo-like fossils. *Nature* **516**, 238–241 (2014).
504. P. F. Hoffman, C. R. Calver, G. P. Halverson, Cottons Breccia of King Island, Tasmania: Glacial or non-glacial, Cryogenian or Ediacaran? *Precambrian Res.* **172**, 311–322 (2009).

505. J. P. Grotzinger, Trends in Precambrian carbonate sediments and their implication for understanding evolution, in *Early Life on Earth*, S. Bengtson, Ed. (Columbia Univ. Press, 1994), pp. 245–258.
506. M. P. Lamb, W. W. Fischer, T. D. Raub, J. T. Perron, P. M. Myrow, Origin of giant wave ripples in snowball Earth cap carbonate. *Geology* **40**, 827–830 (2012).

Acknowledgments: We thank K. Hodges for inviting and B. Schoene for editing this contribution in honor of geologist S. Bowring. We are grateful to R. Pierrehumbert and two anonymous reviewers for comments that materially improved the paper. **Funding:** G.R. was supported by CNRS funding through the ECLIPSE program. B.E.J.R. was supported by NSF grant AGS-1455071. A.V. was supported by the German Federal Ministry of Education and Research (BMBF) and Research for Sustainable Development (FONA) (www.fona.de) under grant 01LK1509A. S.G.W. was supported by NSF grant ANT-1142963. **Author contributions:** P.F.H. conceived and wrote successive drafts of the manuscript, to which each co-author responded with corrections, discussions, and/or revised text. All authors approved the final text and figures. **Competing interests:** The authors declare that they have no competing interests. **Data and materials availability:** All data needed to evaluate the conclusions in the paper are present in the paper and/or references cited. Additional data related to this paper may be requested from the authors.

Submitted 4 May 2016
Accepted 21 September 2017
Published 8 November 2017
10.1126/sciadv.1600983

Citation: P. F. Hoffman, D. S. Abbot, Y. Ashkenazy, D. I. Benn, J. J. Brocks, P. A. Cohen, G. M. Cox, J. R. Creveling, Y. Donnadieu, D. H. Erwin, I. J. Fairchild, D. Ferreira, J. C. Goodman, G. P. Halverson, M. F. Jansen, G. Le Hir, G. D. Love, F. A. Macdonald, A. C. Maloof, C. A. Partin, G. Ramstein, B. E. J. Rose, C. V. Rose, P. M. Sadler, E. Tziperman, A. Voigt, S. G. Warren, Snowball Earth climate dynamics and Cryogenian geology-geobiology. *Sci. Adv.* **3**, e1600983 (2017).

ScienceAdvances

Snowball Earth climate dynamics and Cryogenian geology-geobiology

Paul F. Hoffman, Dorian S. Abbot, Yosef Ashkenazy, Douglas I. Benn, Jochen J. Brocks, Phoebe A. Cohen, Grant M. Cox, Jessica R. Creveling, Yannick Donnadieu, Douglas H. Erwin, Ian J. Fairchild, David Ferreira, Jason C. Goodman, Galen P. Halverson, Malte F. Jansen, Guillaume Le Hir, Gordon D. Love, Francis A. Macdonald, Adam C. Maloof, Camille A. Partin, Gilles Ramstein, Brian E. J. Rose, Catherine V. Rose, Peter M. Sadler, Eli Tziperman, Aiko Voigt and Stephen G. Warren

Sci Adv **3** (11), e1600983.
DOI: 10.1126/sciadv.1600983